DISCLAIMER

Sandia National Laboratories

Operated for the U.S. Department of Energy by
National Technology and Engineering Solutions of Sandia, LLC
Albuquerque, New Mexico 87185-0405
Livermore, California 94551-0969

Date: 22 May 2025

To: Michelle Gallegos, Organization 02932
Michael Hansen, Organization 02932
Kevin Schafer, Organization 02932
Philip Wang, Organization 02932

From: Neal B. Hubbard, Organization 01554

Subject: Empirical Model for Energy Required to Puncture Specimens of 6061-T651 Aluminum Plate

Executive Summary

Specimens of 6061-T651 aluminum with different thicknesses were punctured by AISI 4340 steel probes of three diameters in a series of drop-table experiments. The probes are all right circular cylinders. The times when a probe contacts a specimen and when it breaks through are indicated by the acceleration of the drop-table carriage. The change in the total energy of the carriage between these times is the energy mitigated by each specimen. Only a few replications were performed with each specimen thickness and probe diameter, so the data sets are not amenable to classical statistical inference. Rather than calculate statistics for each combination of geometric parameters, an empirical model is derived that fits all of the experimental data. The model predicts future observations within the range of specimen thicknesses and probe diameters that were tested. Confidence intervals based on the variance in the data account for uncertainty. The lower bounds on the mitigated energy for a few select scenarios are tabulated below.

Table 1: Results of Empirical Model for Mitigated Energy in Select Scenarios

Specimen Thickness	0.063 in		0.125 in		0.188 in		0.250 in	
Probe Diameter	0.250 in	1.000 in	0.250 in	1.000 in	0.250 in	1.000 in	0.250 in	1.000 in
Median, 50%	6.4 ft-lb	30 ft-lb	23 ft-lb	110 ft-lb	50 ft-lb	237 ft-lb	86 ft-lb	405 ft-lb
Lower Bound, 1%	3.5 ft-lb	16.6 ft-lb	12.8 ft-lb	60 ft-lb	28 ft-lb	130 ft-lb	47 ft-lb	222 ft-lb
Lower Bound, 1E-3	2.9 ft-lb	13.4 ft-lb	10.4 ft-lb	49 ft-lb	22 ft-lb	105 ft-lb	38 ft-lb	180 ft-lb
Lower Bound, 1E-6	1.7 ft-lb	7.9 ft-lb	6.2 ft-lb	29 ft-lb	13.3 ft-lb	62 ft-lb	23 ft-lb	107 ft-lb
Lower Bound, 1E-9	1.1 ft-lb	5.0 ft-lb	3.8 ft-lb	18.1 ft-lb	8.3 ft-lb	39 ft-lb	14.2 ft-lb	67 ft-lb

Introduction

Robert Waymel performed a series of experiments on a drop table to measure the energy mitigated by 6061-T651 aluminum as projectiles passed through it (Ref. 1). Specimens were machined from plate stock that was sliced with the wire in an electrical discharge machine (EDM). Milling operations produced surface texture representative of actual components. Cracks nucleate at flaws in the material, and a normal quantity of flaws produces characteristic performance. Polished specimens would likely have mitigated more energy but would have been unrealistic for comparison to machined containers, covers, and lids.

The disc specimens shown in Figures 1 through 4 have pockets where the thickness is reduced so that projectiles can easily penetrate them. The thick rim constrains the thin portion, giving it a fixed boundary condition around the circular perimeter. The reaction forces at the boundary pull downward and radially inward on the rim and tend to curl it such that the outer edges lift off of the fixture. The rim is designed to minimize this deformation.

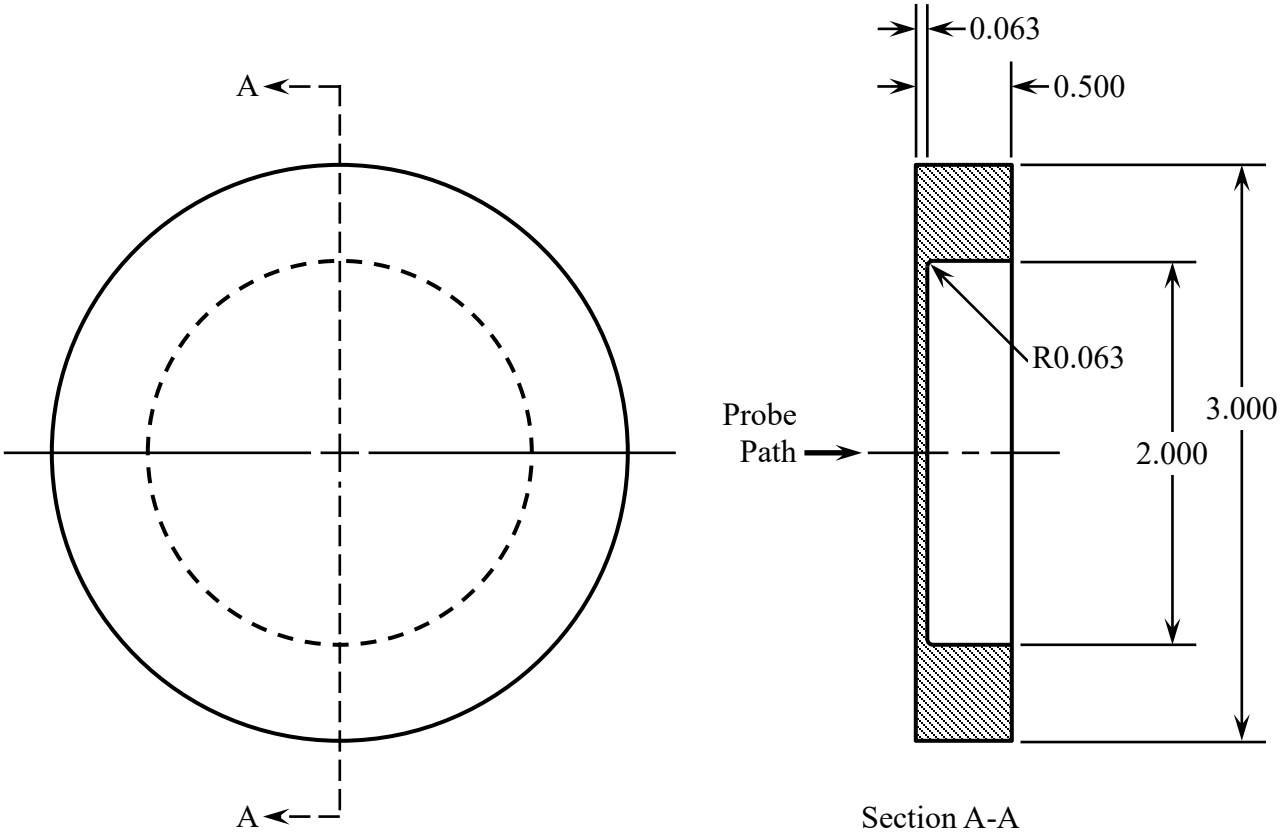

Figure 1: 6061-T651 Aluminum Disc Specimen with Thickness of 0.063 Inch

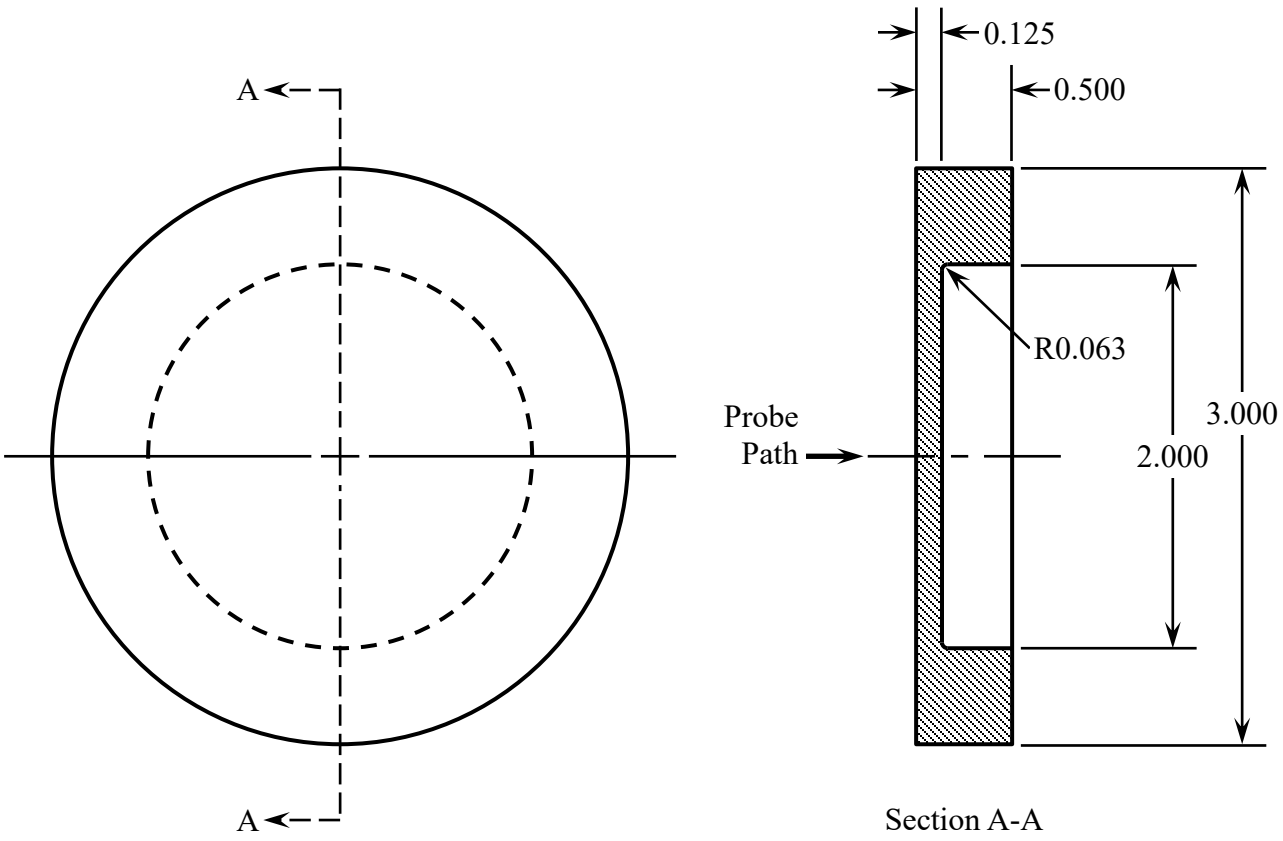

Figure 2: 6061-T651 Aluminum Disc Specimen with Thickness of 0.125 Inch

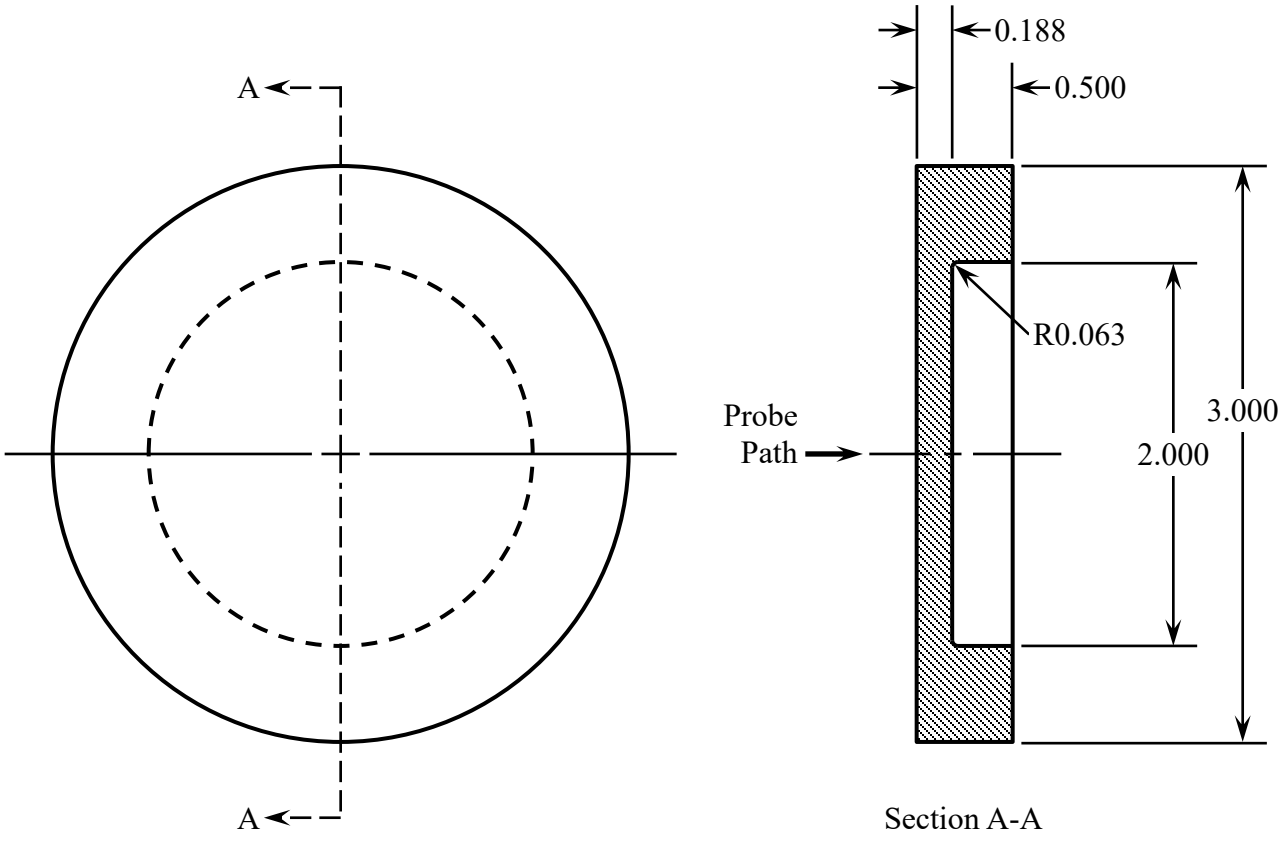

Figure 3: 6061-T651 Aluminum Disc Specimen with Thickness of 0.188 Inch

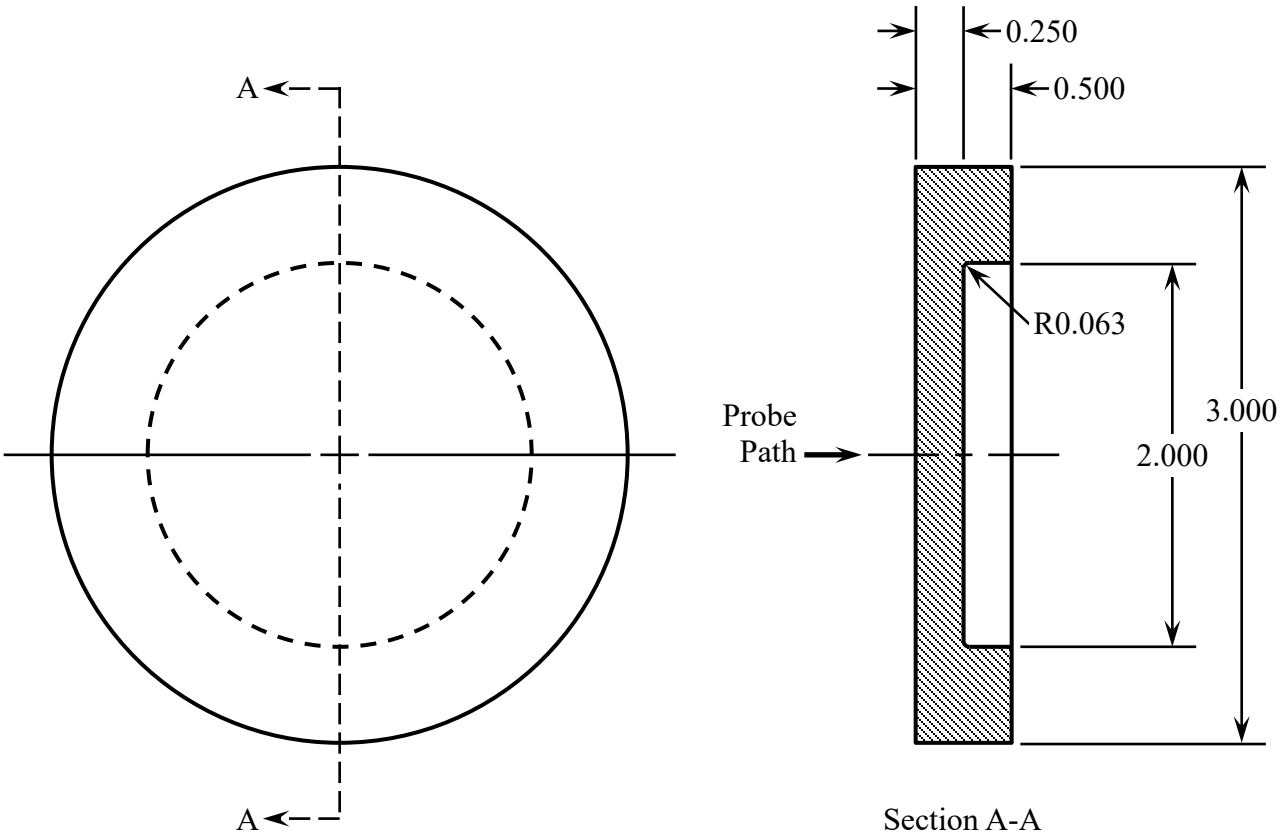

Figure 4: 6061-T651 Aluminum Disc Specimen with Thickness of 0.250 Inch

The probes are straight cylinders turned from AISI 4340 steel bars and hardened to 42–48 Rockwell C hardness (HRC). Figures 5 through 7 give the dimensions in inches. The interface between the probe and the drop table is standardized for quick probe exchanges.

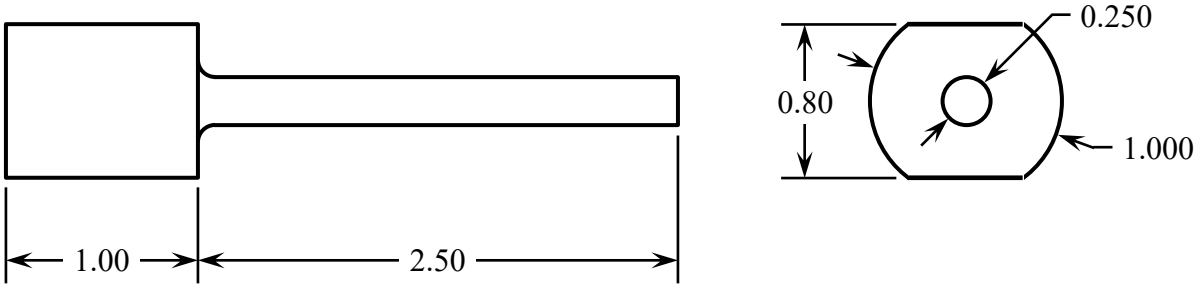

Figure 5: Cylindrical Probe with Diameter of 0.250 Inch and Flat End

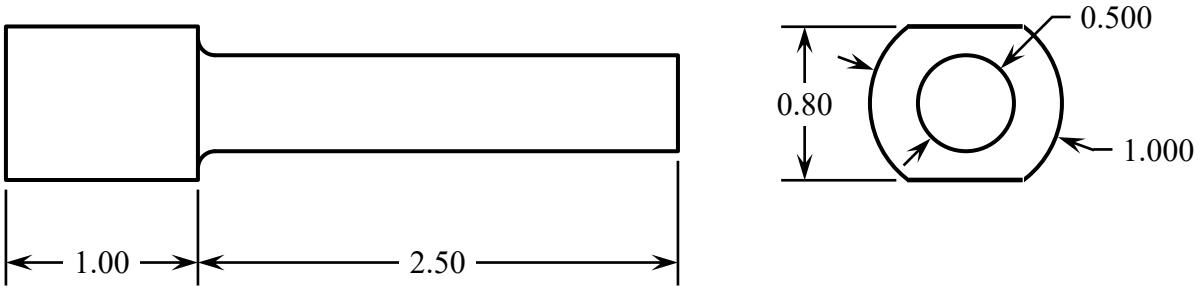

Figure 6: Cylindrical Probe with Diameter of 0.500 Inch and Flat End

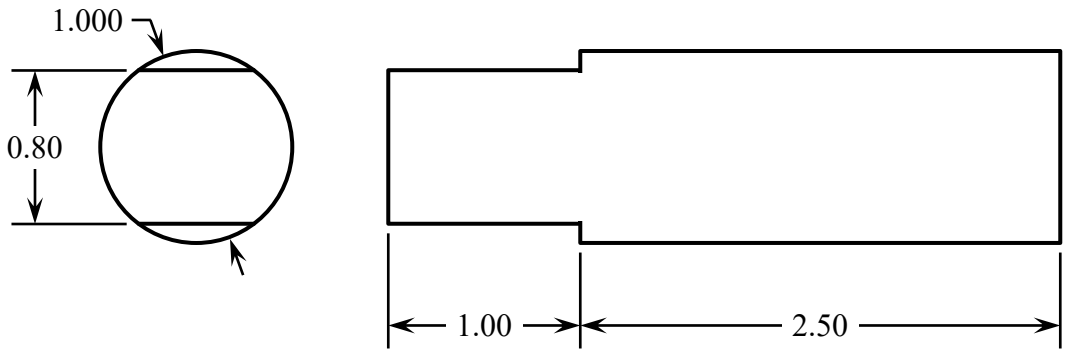

Figure 7: Cylindrical Probe with Diameter of 1.000 Inch and Flat End

The drop table has a 1370 N (308 lb) carriage that guides the probes along a straight path intersecting the specimens. The specimens are held in fixtures that constrain them against being pushed by the probes and resist lateral motion after a little clearance is removed. The specimens are free to lift off of the fixture and deform. Two laser interferometers measure the position of the carriage, and an accelerometer on the carriage measures the resistance to the falling mass. When the carriage is released from a planned height, the acceleration drops from 1 G to between 0.30 G and 0.62 G; friction in the guide rods prevents free-fall, and they are lubricated regularly to minimize it. Data collection begins as the probe approaches the specimen. Upon contact, an elastic wave travels through the probe to the carriage and registers an increase in the acceleration (resistance to gravity). The acceleration rises to between 3 G and 66 G as the aluminum work hardens; after it reaches the ultimate stress and the specimen fractures, the acceleration settles down to the previous level. The peak acceleration indicates the maximum force required to puncture the specimen, which depends on the thickness of the specimen and the geometry of the probe. If friction between the specimen and the probe does not arrest the descent, the probe passes through a hole in the fixture, and the carriage settles onto felt programming rings. The data of interest are collected before the carriage either stops or contacts the rings. The drop table is shown in Figure 8 (Ref. 1, p. 3, Fig. 3) and the various probes in Figure 9 (Ref. 1, p. 2, Fig. 2(c)).

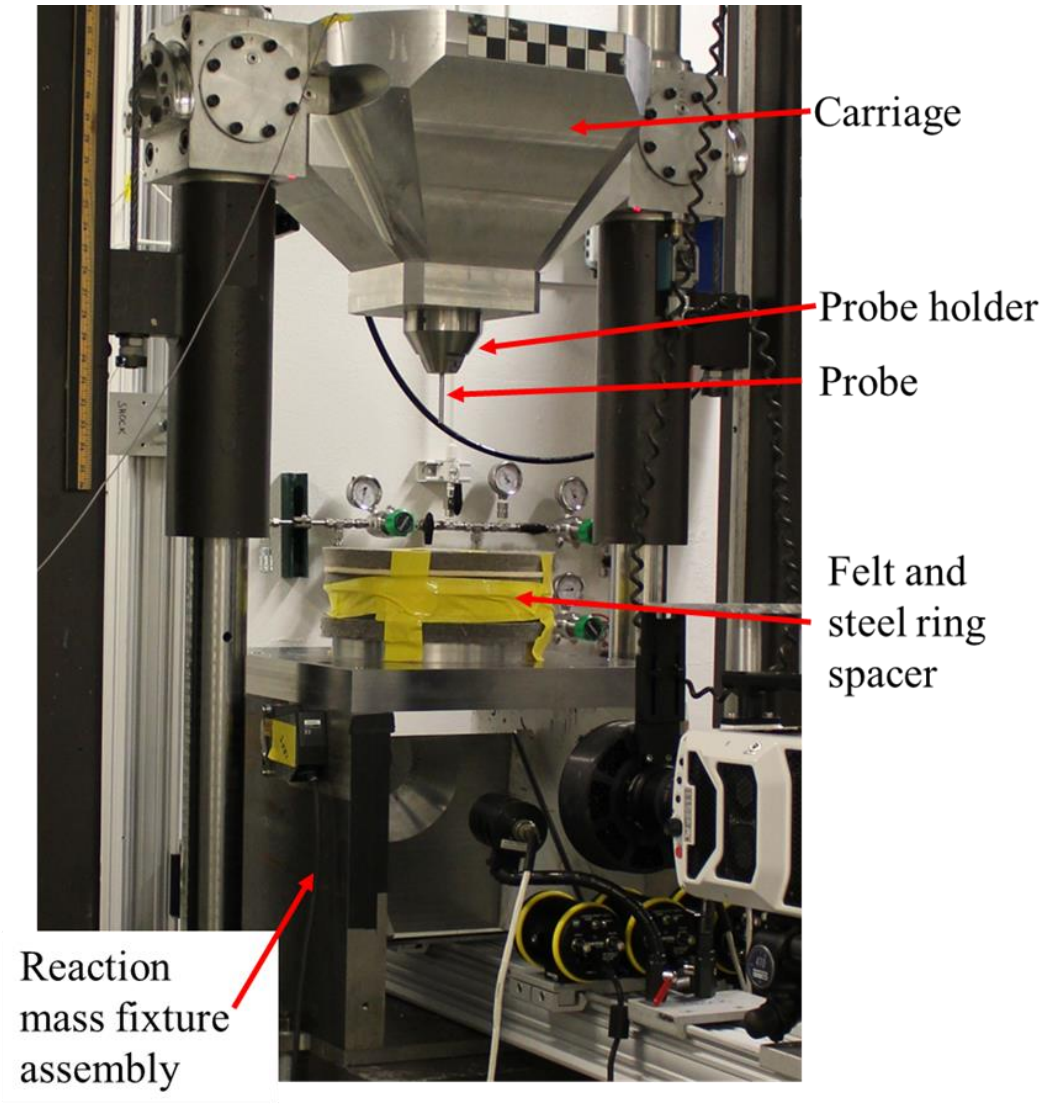

Figure 8: Drop Table Carriage Holding One-Quarter-Inch Flat-End Probe

Figure 9: Cylindrical Probes with Diameters of 1.000, 0.500, and 0.250 Inches and Flat Ends

As each probe punctured a specimen, it ejected a plug. Following each test, the specimen typically adhered to the probe and was lifted when the carriage raised to the reset position. Significant force and energy were required to separate some of the larger probes and thicker specimens. Each combination of specimen thickness and probe diameter is represented in the subsequent figures with a view toward the surface that the probe emerged from. The plug is contained in a plastic bag behind each specimen.

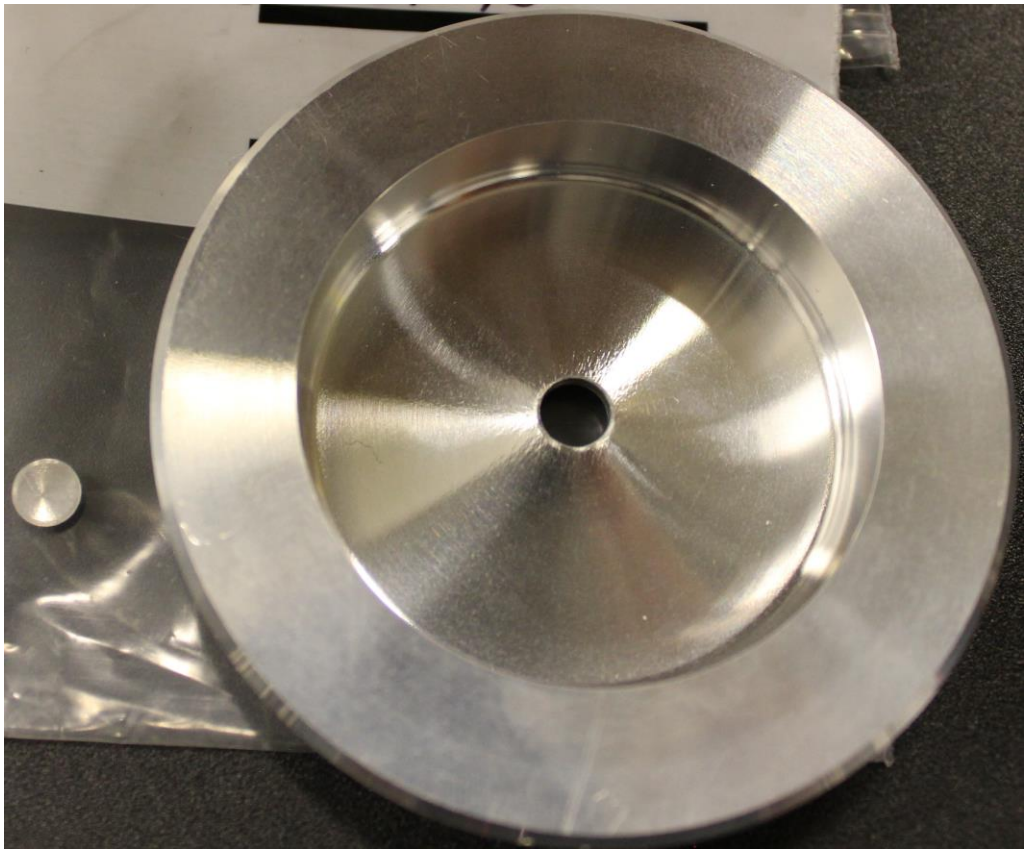

Figure 10: Specimen T063-06 and Ejected Plug After Test 38 with One-Quarter-Inch Probe

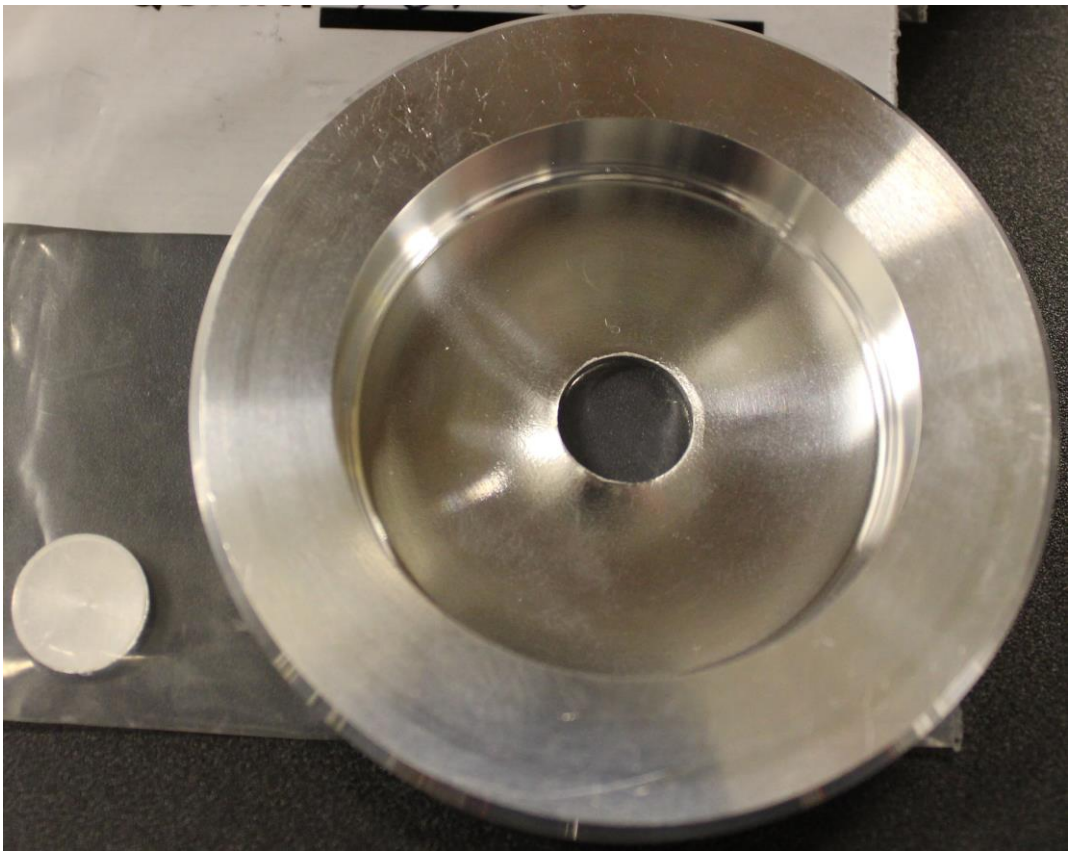

Figure 11: Specimen T063-07 and Ejected Plug After Test 39 with One-Half-Inch Probe

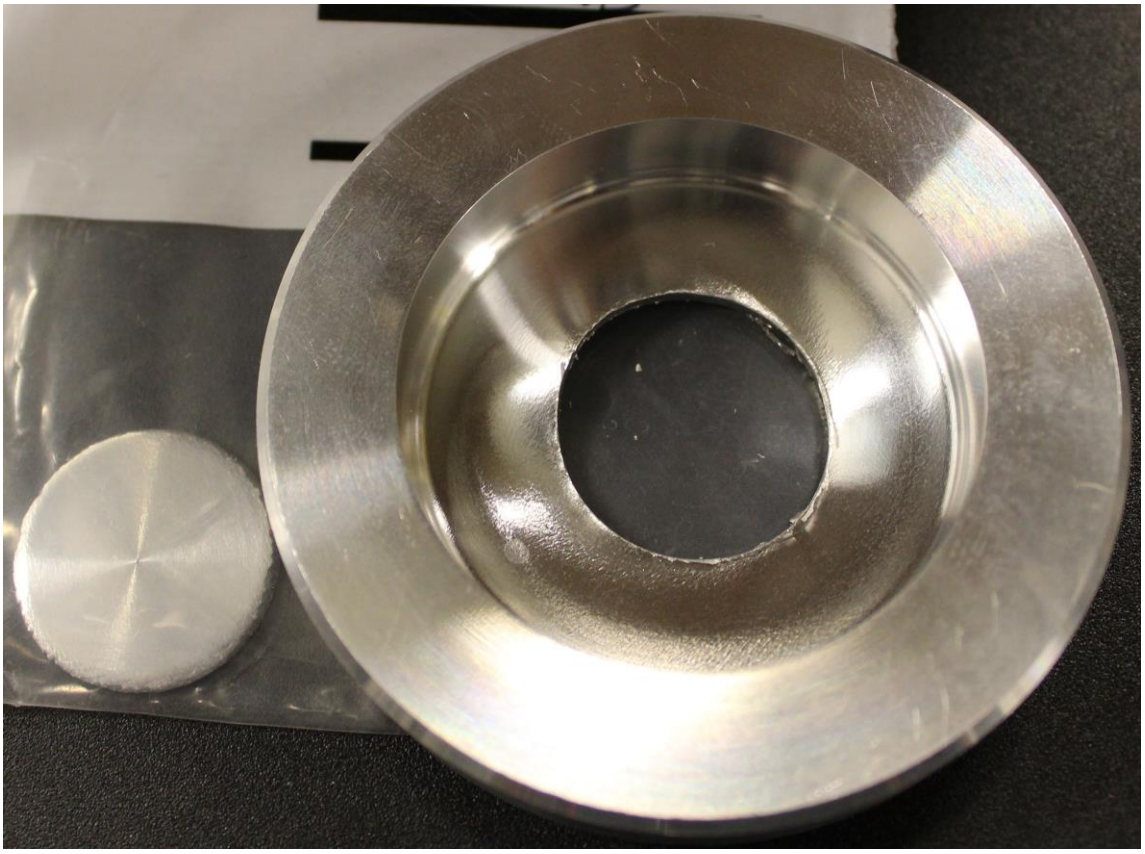

Figure 12: Specimen T063-11 and Ejected Plug After Test 43 with One-Inch Probe

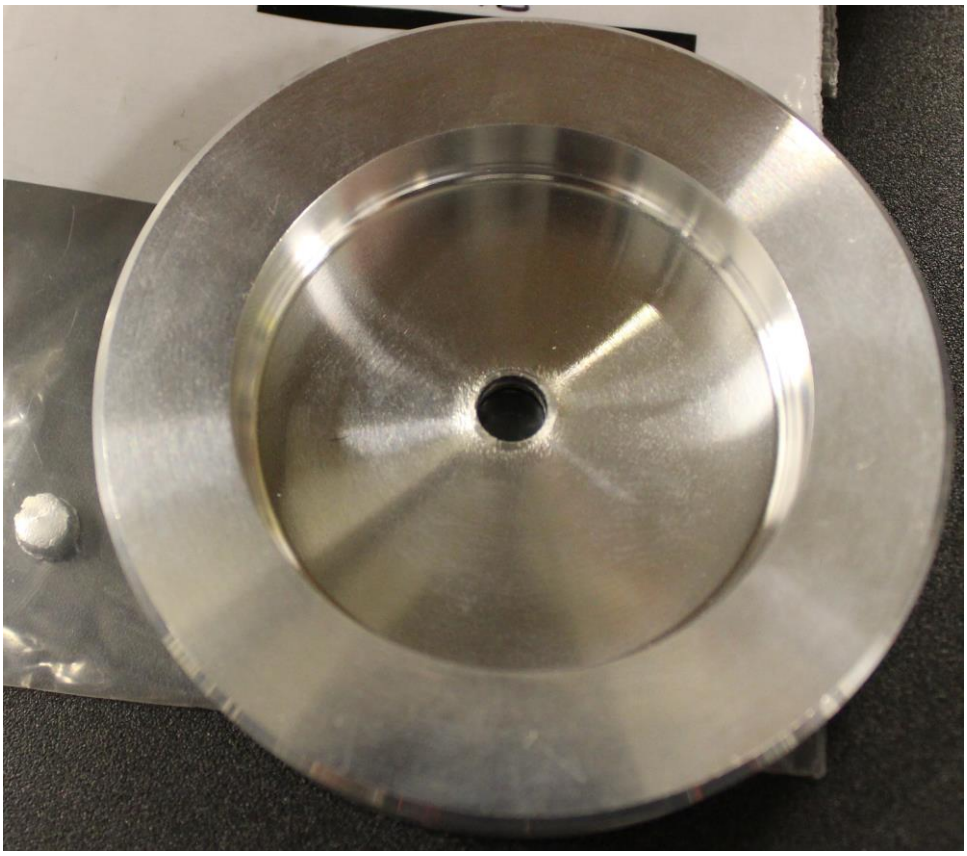

Figure 13: Specimen T125-05 and Ejected Plug After Test 52 with One-Quarter-Inch Probe

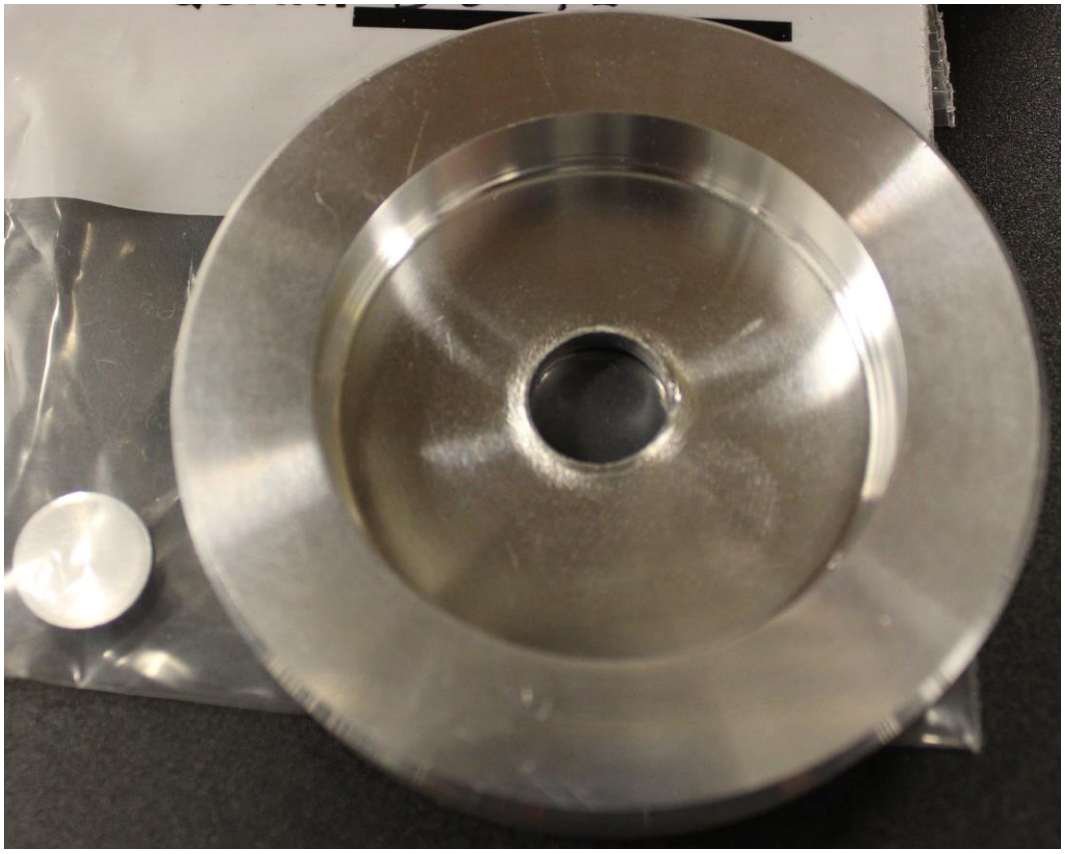

Figure 14: Specimen T125-08 and Ejected Plug After Test 60 with One-Half-Inch Probe

Figure 15: Specimen T125-12 and Ejected Plug After Test 65 with One-Inch Probe

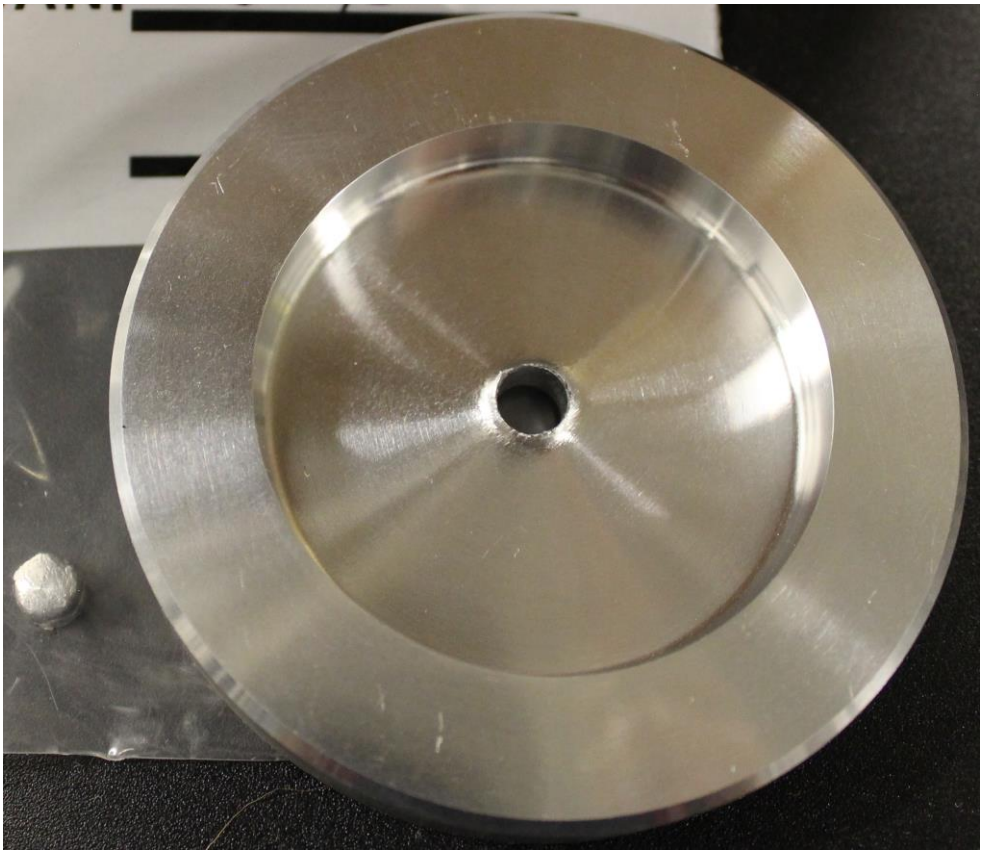

Figure 16: Specimen T188-05 and Ejected Plug After Test 77 with One-Quarter-Inch Probe

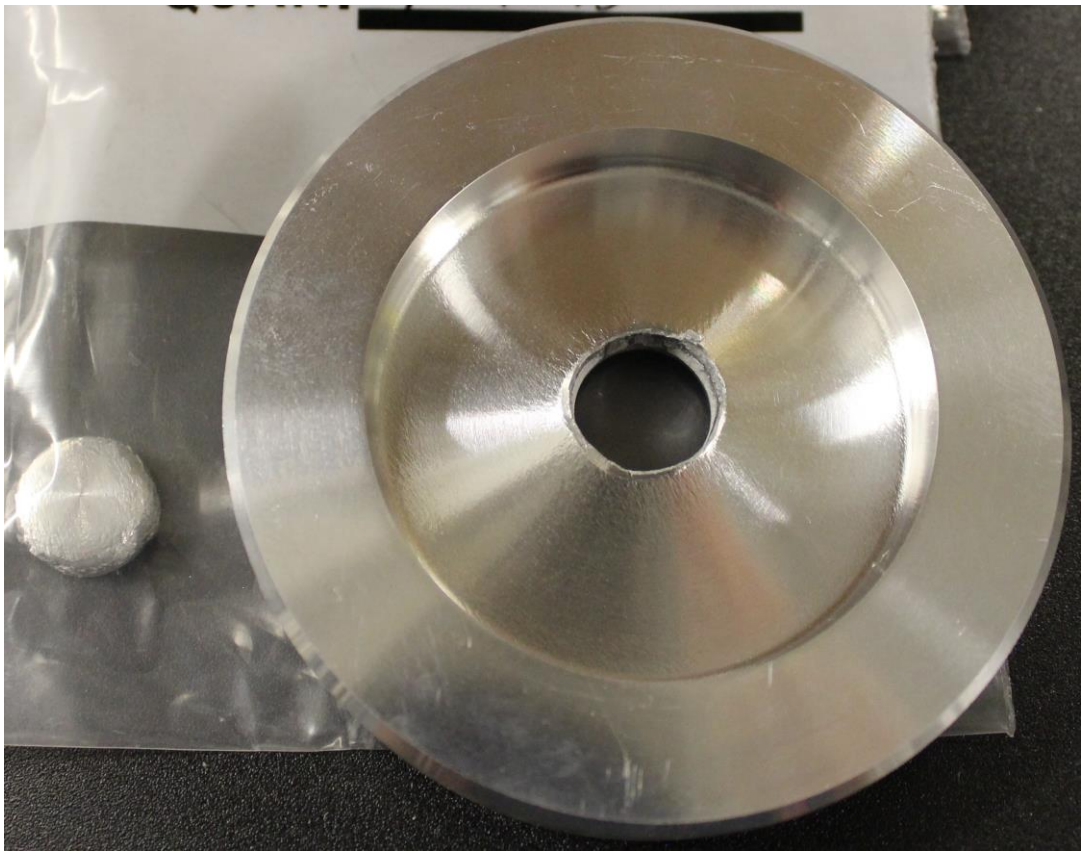

Figure 17: Specimen T188-09 and Ejected Plug After Test 81 with One-Half-Inch Probe

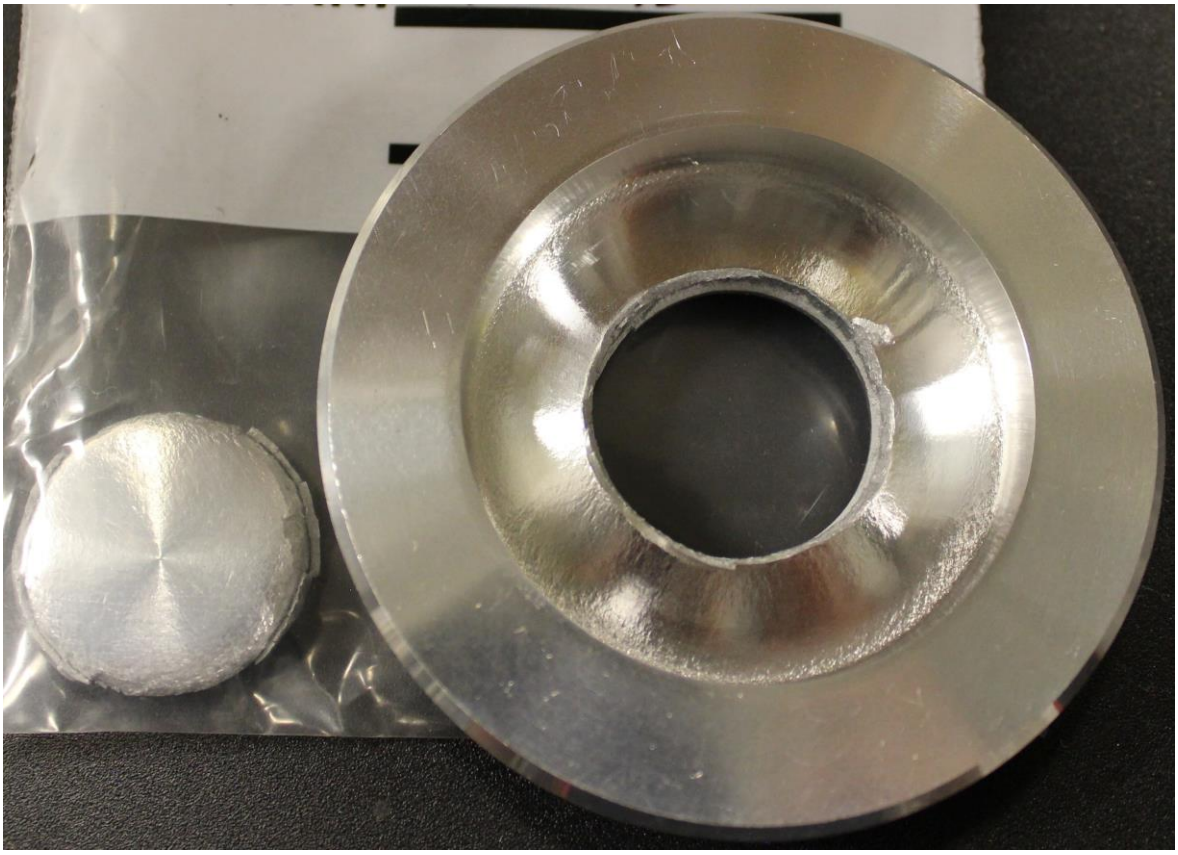

Figure 18: Specimen T188-14 and Ejected Plug After Test 86 with One-Inch Probe

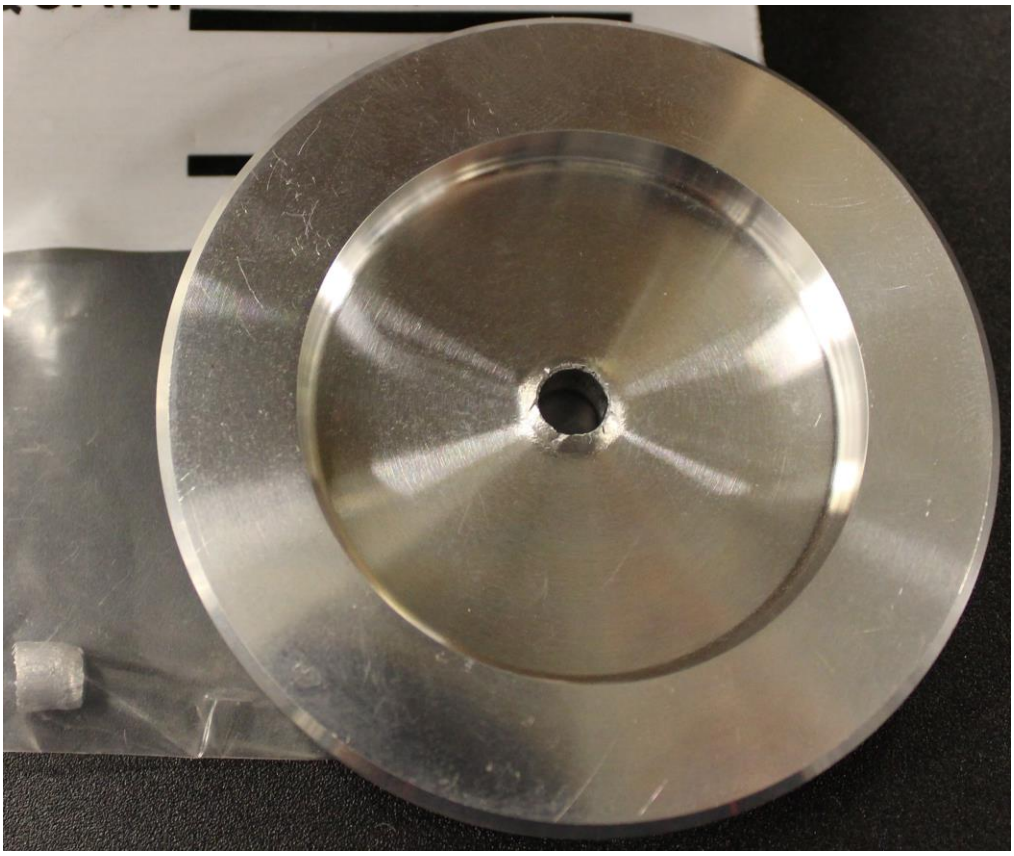

Figure 19: Specimen T250-03 and Ejected Plug After Test 90 with One-Quarter-Inch Probe

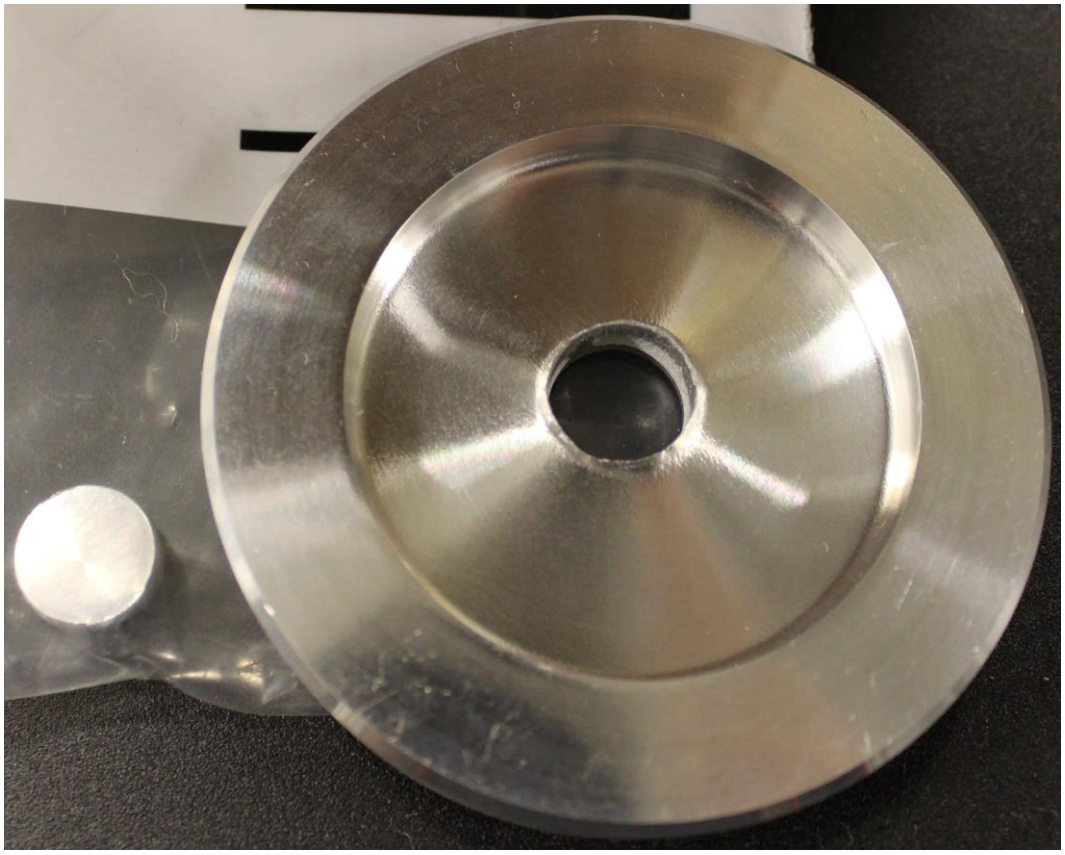

Figure 20: Specimen T250-10 and Ejected Plug After Test 97 with One-Half-Inch Probe

Figure 21: Specimen T250-15 and Ejected Plug After Test 102 with One-Inch Probe

Data Processing Method

Most of the processing parameters are optimized for each test because of significant differences in the measured data. These values are listed in Table 2. Although consistency in the processing parameters has been preferred, they cannot be the same for every test. Rather, a consistent approach has been taken to determine the values based on the observed data.

Table 2: Data Processing Parameters

Test	Specimen	Acceleration		Threshold		Time Offset		Time Period	Reference Position, p_r	
		Free-Fall, a_f (G)	Peak, a_p (G)	Impact, $a_{t,i}$ (G)	Puncture, $a_{t,p}$ (G)	Impact, $\Delta t_{o,i}$ (ms)	Puncture, $\Delta t_{o,p}$ (ms)	Puncture, $\Delta t_{E,p}$ (ms)	(mm)	(in)
35	T063-02	0.369	2.98	0.2	1.0	0.5	0.6	1.6	-4.32	-0.170
36	T063-04	0.302	3.05	0.3	1.0	0.7	0.2	2.4	-4.34	-0.171
37	T063-05	0.295	3.01	0.3	1.2	0.5	0.5	1.4	-4.54	-0.179
38	T063-06	0.316	3.00	0.3	1.2	0.5	0.5	2.4	-4.44	-0.175
39	T063-07	0.320	5.50	0.4	2.0	0.5	0.2	1.8	-4.77	-0.188
40	T063-08	0.325	5.49	0.4	1.8	0.5	-0.5	1.5	-4.63	-0.182
41	T063-09	0.328	5.37	0.4	1.8	0.4	-0.5	1.4	-4.61	-0.181
42	T063-10	0.339	5.50	0.4	1.6	0.4	-0.2	1.4	-4.65	-0.183
43	T063-11	0.419	9.91	0.5	2.0	1.4	-0.4	1.4	-4.71	-0.185
44	T063-12	0.367	9.92	0.5	2.0	0.5	0.3	1.8	-5.47	-0.215
45	T063-13	0.331	10.31	0.5	2.0	0.4	0.6	2.1	-5.35	-0.211
46	T063-14	0.312	9.90	0.5	2.0	0.5	0.2	1.8	-5.15	-0.203
47	T063-15	0.306	10.15	0.5	2.0	0.5	0.3	2.0	-5.05	-0.199
49	T125-02	0.315	7.25	0.4	2.0	0.5	0.5	5.0	-5.09	-0.200
50	T125-03	0.319	7.63	0.4	1.6	0.5	0.5	5.0	-7.23	-0.285
51	T125-04	0.398	7.56	0.4	3.2	0.2	-0.3	1.5	-5.10	-0.201
52	T125-05	0.391	7.39	0.4	3.0	0.5	-0.4	1.5	-4.69	-0.185
59	T125-07	0.435	12.93	0.5	5.0	0.5	0.3	1.5	-6.92	-0.272
60	T125-08	0.391	12.16	0.5	5.0	0.5	-0.3	1.4	-6.10	-0.240
61	T125-09	0.424	12.66	0.5	5.0	0.5	-0.8	1.2	-5.80	-0.228
62	T125-10	0.423	12.22	0.5	5.0	0.5	-0.3	1.5	-5.67	-0.223
64	T125-11	0.439	24.8	1.0	10.0	0.5	0.5	1.8	-6.10	-0.240
65	T125-12	0.413	23.2	1.0	10.0	0.5	0.5	2.0	-5.38	-0.212
66	T125-13	0.386	23.9	1.0	10.0	0.5	0.2	1.4	-5.26	-0.207
67	T125-14	0.398	24.3	1.0	10.0	0.5	-0.3	1.4	-5.14	-0.202
68	T125-15	0.461	49.3	2.0	10.0	0.5	0.3	1.5	-5.24	-0.206
73	T188-01	0.498	13.28	1.0	8.0	0.5	0.7	1.5	-4.42	-0.174
74	T188-02	0.404	13.38	1.0	8.0	0.5	0.8	1.4	-4.56	-0.179
75	T188-03	0.401	13.34	1.0	8.0	0.5	0.7	1.5	-4.56	-0.180
76	T188-04	0.401	13.06	1.0	8.0	0.5	0.5	1.5	-4.50	-0.177
77	T188-05	0.443	12.82	1.0	8.0	0.5	0.9	1.5	-4.58	-0.180
78	T188-06	0.462	20.6	1.0	8.0	0.5	0.4	1.5	-5.64	-0.222
79	T188-07	0.480	20.5	1.0	8.0	0.5	0.6	2.4	-5.00	-0.197
80	T188-08	0.440	22.0	1.0	12.0	0.6	0.2	1.3	-5.48	-0.216
81	T188-09	0.429	20.8	1.0	5.0	0.5	0.5	1.7	-5.42	-0.213
82	T188-10	0.447	21.7	1.0	5.0	0.5	0.4	2.1	-5.08	-0.200
83	T188-11	0.616	40.2	2.0	20.0	0.5	-0.3	1.2	-4.36	-0.172
84	T188-12	0.501	45.8	2.0	20.0	0.6	-0.8	1.2	-4.34	-0.171
85	T188-13	0.487	41.2	2.0	15.0	0.6	-0.4	1.2	-4.66	-0.183
86	T188-14	0.406	40.5	2.0	15.0	0.6	-0.3	1.5	-4.64	-0.183
87	T188-15	0.566	39.9	2.0	15.0	0.4	-0.5	1.5	-4.22	-0.166
88	T250-01	0.447	18.69	2.0	5.0	0.5	0.5	2.0	-3.87	-0.152

Table 2: Data Processing Parameters, Continued

Test	Specimen	Acceleration		Threshold		Time Offset		Time Period	Reference Position, p_r	
		Free-Fall, a_f (G)	Peak, a_p (G)	Impact, $a_{t,i}$ (G)	Puncture, $a_{t,p}$ (G)	Impact, $\Delta t_{o,i}$ (ms)	Puncture, $\Delta t_{o,p}$ (ms)	Puncture, $\Delta t_{E,p}$ (ms)	(mm)	(in)
89	T250-02	0.453	18.94	2.0	8.0	0.5	0.6	2.0	-3.97	-0.156
90	T250-03	0.446	19.69	2.0	10.0	0.5	0.5	1.9	-3.91	-0.154
91	T250-04	0.457	19.41	2.0	10.0	0.5	0.5	2.0	-3.89	-0.153
92	T250-05	0.455	18.77	2.0	10.0	0.5	0.4	1.3	-4.80	-0.189
94	T250-07	0.429	32.5	2.0	10.0	0.5	0.4	2.2	-4.91	-0.193
95	T250-08	0.425	33.2	2.0	10.0	0.5	0.5	2.2	-4.89	-0.192
96	T250-09	0.411	33.2	2.0	10.0	0.5	0.5	2.2	-5.07	-0.200
97	T250-10	0.409	32.9	2.0	10.0	0.5	0.4	2.2	-4.80	-0.189
98	T250-11	0.460	48.1	3.0	15.0	0.5	-0.7	1.4	-4.19	-0.165
99	T250-12	0.487	53.2	3.0	15.0	0.5	-0.3	1.8	-4.71	-0.185
100	T250-13	0.510	64.1	3.0	15.0	0.5	-0.3	1.2	-4.63	-0.182
101	T250-14	0.462	65.9	3.0	15.0	0.5	-0.2	1.6	-4.92	-0.194
102	T250-15	0.454	62.1	3.0	15.0	0.5	-0.4	1.4	-4.48	-0.177

The times when the probe contacts the specimen and penetrates it are determined from the acceleration data. Threshold accelerations are selected for identifying the impact and puncture events. Impact is considered to occur at the last time (t_i) when the acceleration is less than the impact threshold ($a_{t,i}$) prior to the peak acceleration (a_p), and the puncture is considered complete at the last time (t_p) when the acceleration is greater than the puncture threshold ($a_{t,p}$) after the peak. Figure 22 illustrates these accelerations and times. The thresholds for tests with a particular combination of input parameters are similar; however, differences in the data necessitate some variation. The figures in Appendix A show the acceleration data for each test with the thresholds for impact and complete puncture.

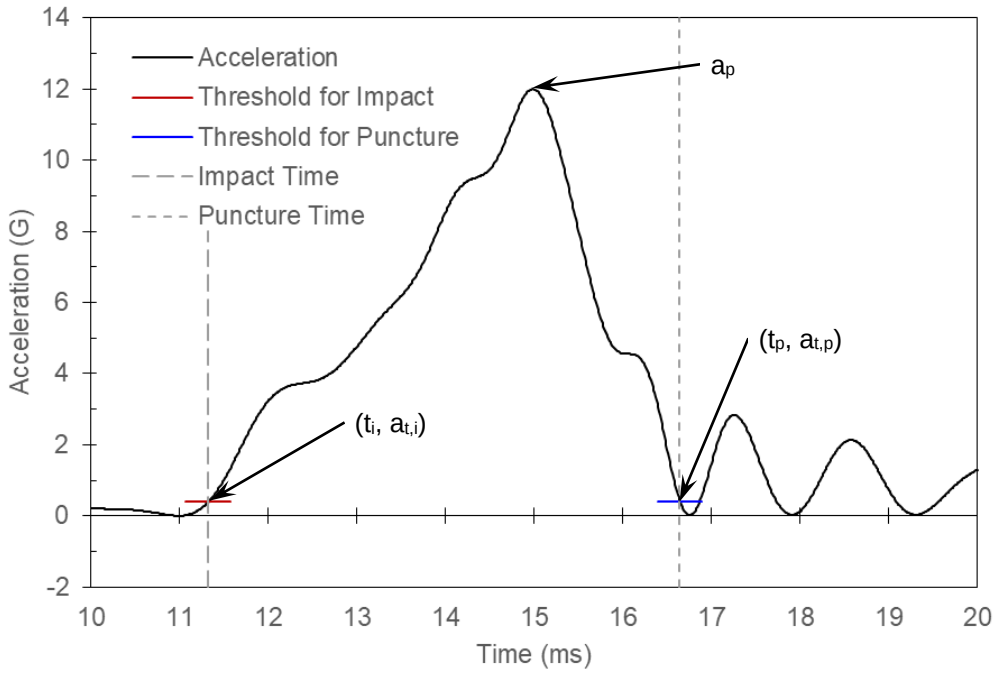

Figure 22: Representative Acceleration Curve with Impact and Puncture Times Identified

The position data from the two laser interferometers (p_L on the left and p_R on the right) are averaged and shifted with Equation 1. The reference position (p_r) is selected such that the position is zero when the puncture process is complete (t_p). The reference position also makes the potential energy (E_P, Eq. 2) positive when the probe contacts the specimen and zero when it breaks through. The mass (m) of the carriage with the attached mounting fixtures, accelerometer, and probe is 139.7 kg (9.57 slug). The free-fall acceleration of the carriage (a_f) is calibrated to correspond to a free-fall condition prior to the time of impact, accounting for friction in the guide rods, and is explained subsequently.

$$p = \frac{p_L + p_R}{2} - p_r \tag{1}$$

$$E_P = m\, a_f\, p \tag{2}$$

The average carriage position is differentiated to obtain the carriage velocity (v, Eq. 3). For each time in the data set, the velocity value (v_j) is given by Equation 4, where j is the index of the data points. The majority of the velocity values are computed with the second-order central finite difference formula; the first and last velocity values are evaluated with first-order finite difference formulas based on the available data points. The kinetic energy of the carriage and probe is defined by Equation 5 and the total energy by Equation 6.

$$v = \frac{dp}{dt} \tag{3}$$

$$v_j = \begin{cases} \dfrac{p_{j+1} - p_j}{t_{j+1} - t_j} & j = 1 \\ \dfrac{p_{j+1} - p_{j-1}}{t_{j+1} - t_{j-1}} & j = 2 \ldots n - 1 \\ \dfrac{p_j - p_{j-1}}{t_j - t_{j-1}} & j = n \end{cases} \tag{4}$$

$$E_K = \frac{m\, v^2}{2} \tag{5}$$

$$E_T = E_P + E_K \tag{6}$$

The free-fall acceleration of the carriage is optimized such that a linear fit to the total energy during a certain period of time prior to the probe contacting the specimen has zero slope. This calibrates the data to a true free-fall condition prior to the time of impact. It correctly accounts for friction in the carriage guide rods and the increase in potential energy as the carriage falls through the specimen. The total energy is always averaged over a time period of 15 ms ($\Delta t_{E,i}$), but the end of the period is offset relative to the impact time (t_i), and the offset ($\Delta t_{o,i}$) differs between tests. During this period, several complete cycles of oscillation are observed in the total energy. The average of the total energy in this period is taken as the total energy before impact ($E_{T,i}$). The total energy after complete puncture ($E_{T,p}$) is the average value in a period of time beginning within 1 ms ($\Delta t_{o,p}$) of the puncture time (t_p) and lasting about 2 ms ($\Delta t_{E,p}$). Table 2 has the actual values of the puncture time offset and period for each test. The total energy mitigated by the specimen is

$$E_M = E_{T,i} - E_{T,p} \tag{7}$$

Figure 23 illustrates the time periods over which the total energy is averaged and the difference between the averages. The figures in Appendix B plot the total energy as a

function of time and bracket the time periods that are averaged before impact and after complete puncture.

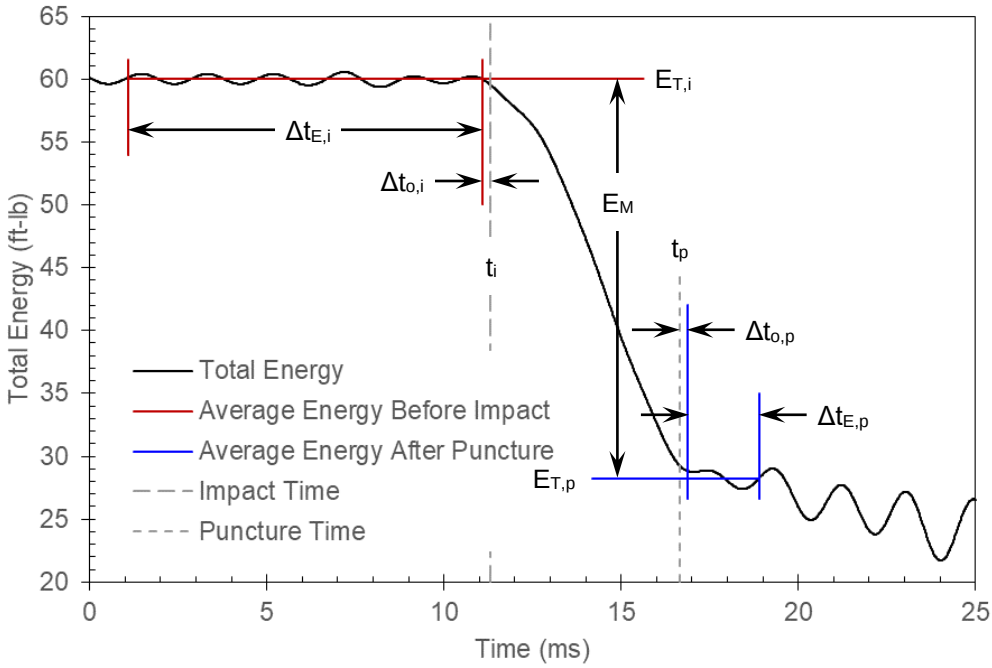

Figure 23: Representative Total Energy Curve and Time Periods for Averaging

The carriage velocity before impact (v_i) is found by averaging the velocity values over a time period of 500 µs ($\Delta t_{v,i}$) that ends at the offset impact time ($t_i - \Delta t_{o,i}$). The velocity after complete puncture (v_p) is the average value over a time period of 500 µs ($\Delta t_{v,p}$) that starts at the offset puncture time ($t_p + \Delta t_{o,p}$). The time periods are constant, but the offsets are unique to each test (Table 2). Figure 24 illustrates the time periods and offsets. Appendix C has plots of the velocity data for each test and the time periods in which it is averaged.

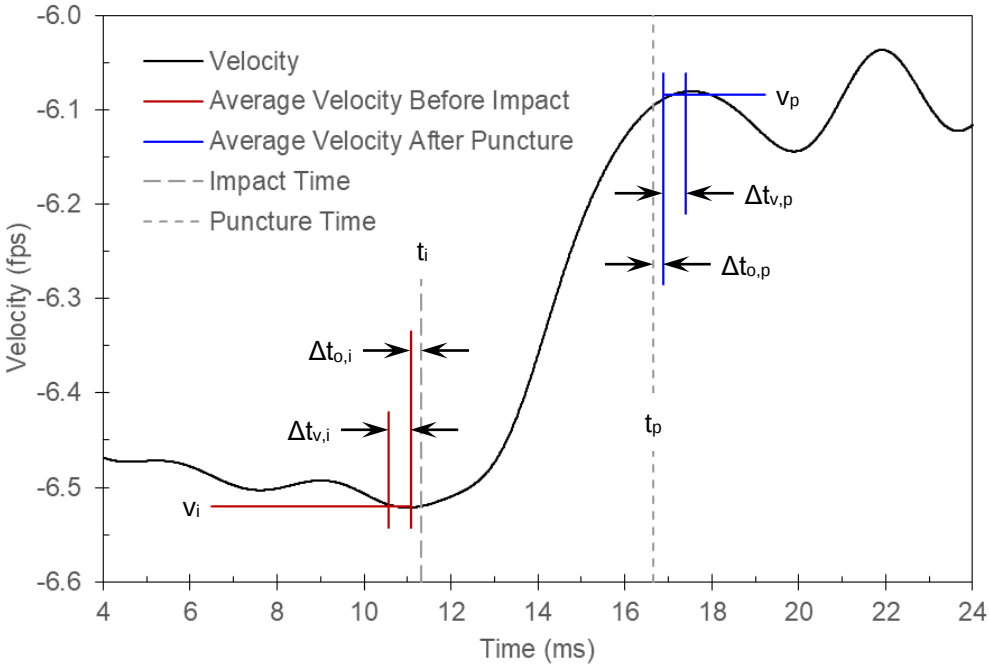

Figure 24: Representative Velocity Curve and Time Periods for Averaging

Table 3 correlates the test and specimen numbers with the measured thickness of each specimen at the gauge section and the nominal diameter of the probe. The maximum deviation between the measured thickness (the average of several measurements) and the nominal thickness is 0.7%. The distance traveled by the probe during the puncture process is the difference in the positions at the impact and puncture times (t_i, t_p). The results of the distance, velocity, and energy calculations are provided in Tables 4 and 5.

Table 3: Measurements of Disc Specimens Made from 6061-T651 Plate and Nominal Probe Diameters

Test	Specimen	Probe Design	Thickness (mm)	Thickness (in)	Probe Diameter (mm)	Probe Diameter (in)
35	T063-02	F0250	1.599	0.0630	6.35	0.250
36	T063-04	F0250	1.601	0.0631	6.35	0.250
37	T063-05	F0250	1.600	0.0630	6.35	0.250
38	T063-06	F0250	1.605	0.0632	6.35	0.250
39	T063-07	F0500	1.612	0.0635	12.70	0.500
40	T063-08	F0500	1.605	0.0632	12.70	0.500
41	T063-09	F0500	1.608	0.0633	12.70	0.500
42	T063-10	F0500	1.598	0.0629	12.70	0.500
43	T063-11	F1000	1.598	0.0629	25.40	1.000
44	T063-12	F1000	1.596	0.0629	25.40	1.000
45	T063-13	F1000	1.595	0.0628	25.40	1.000
46	T063-14	F1000	1.594	0.0628	25.40	1.000
47	T063-15	F1000	1.599	0.0630	25.40	1.000
49	T125-02	F0250	3.181	0.1253	6.35	0.250
50	T125-03	F0250	3.176	0.1251	6.35	0.250
51	T125-04	F0250	3.185	0.1254	6.35	0.250

Table 3: Measurements of Disc Specimens Made from 6061-T651 Plate and Nominal Probe Diameters, Continued

Test	Specimen	Probe Design	Thickness (mm)	Thickness (in)	Probe Diameter (mm)	Probe Diameter (in)
52	T125-05	F0250	3.179	0.1252	6.35	0.250
59	T125-07	F0500	3.176	0.1251	12.70	0.500
60	T125-08	F0500	3.179	0.1252	12.70	0.500
61	T125-09	F0500	3.174	0.1250	12.70	0.500
62	T125-10	F0500	3.176	0.1251	12.70	0.500
64	T125-11	F1000	3.176	0.1251	25.40	1.000
65	T125-12	F1000	3.174	0.1250	25.40	1.000
66	T125-13	F1000	3.179	0.1252	25.40	1.000
67	T125-14	F1000	3.176	0.1251	25.40	1.000
68	T125-15	F1000	3.174	0.1250	25.40	1.000
73	T188-01	F0250	4.779	0.1882	6.35	0.250
74	T188-02	F0250	4.780	0.1882	6.35	0.250
75	T188-03	F0250	4.785	0.1884	6.35	0.250
76	T188-04	F0250	4.778	0.1881	6.35	0.250
77	T188-05	F0250	4.776	0.1881	6.35	0.250
78	T188-06	F0500	4.771	0.1879	12.70	0.500
79	T188-07	F0500	4.776	0.1881	12.70	0.500
80	T188-08	F0500	4.771	0.1879	12.70	0.500
81	T188-09	F0500	4.774	0.1880	12.70	0.500
82	T188-10	F0500	4.770	0.1878	12.70	0.500
83	T188-11	F1000	4.770	0.1878	25.40	1.000
84	T188-12	F1000	4.774	0.1880	25.40	1.000
85	T188-13	F1000	4.773	0.1879	25.40	1.000
86	T188-14	F1000	4.771	0.1879	25.40	1.000
87	T188-15	F1000	4.771	0.1879	25.40	1.000
88	T250-01	F0250	6.351	0.2501	6.35	0.250
89	T250-02	F0250	6.359	0.2504	6.35	0.250
90	T250-03	F0250	6.354	0.2502	6.35	0.250
91	T250-04	F0250	6.354	0.2502	6.35	0.250
92	T250-05	F0250	6.351	0.2501	6.35	0.250
94	T250-07	F0500	6.361	0.2505	12.70	0.500
95	T250-08	F0500	6.359	0.2504	12.70	0.500
96	T250-09	F0500	6.351	0.2501	12.70	0.500
97	T250-10	F0500	6.351	0.2501	12.70	0.500
98	T250-11	F1000	6.350	0.2500	25.40	1.000
99	T250-12	F1000	6.349	0.2500	25.40	1.000
100	T250-13	F1000	6.349	0.2500	25.40	1.000
101	T250-14	F1000	6.349	0.2500	25.40	1.000
102	T250-15	F1000	6.346	0.2499	25.40	1.000

Table 4: Results of Puncture Experiments with Flat-End Probes on Disc Specimens Made from 6061-T651 Plate

Test	Specimen	Probe Design	Distance Traveled (mm)	Distance Traveled (in)	Impact Velocity, v_i (m/s)	Impact Velocity, v_i (fps)	Puncture Velocity, v_p (m/s)	Puncture Velocity, v_p (fps)
35	T063-02	F0250	5.41	0.213	0.42	1.37	0.18	0.59
36	T063-04	F0250	5.42	0.213	0.59	1.94	0.46	1.49
37	T063-05	F0250	5.51	0.217	0.57	1.87	0.42	1.37
38	T063-06	F0250	5.35	0.211	0.55	1.82	0.41	1.34
39	T063-07	F0500	6.05	0.238	0.84	2.76	0.65	2.12
40	T063-08	F0500	5.69	0.224	0.80	2.61	0.59	1.95
41	T063-09	F0500	5.54	0.218	0.76	2.48	0.55	1.82
42	T063-10	F0500	5.63	0.222	0.78	2.56	0.58	1.92
43	T063-11	F1000	7.19	0.283	1.14	3.75	0.89	2.92
44	T063-12	F1000	6.85	0.270	0.94	3.09	0.57	1.88
45	T063-13	F1000	6.46	0.254	0.89	2.91	0.49	1.59
46	T063-14	F1000	6.42	0.253	0.86	2.83	0.46	1.50
47	T063-15	F1000	6.22	0.245	0.85	2.80	0.43	1.42
49	T125-02	F0250	6.29	0.247	0.76	2.49	-0.01	-0.04
50	T125-03	F0250	8.58	0.338	0.86	2.82	-0.02	-0.06
51	T125-04	F0250	6.42	0.253	1.21	3.97	0.92	3.03
52	T125-05	F0250	6.23	0.245	1.11	3.64	0.81	2.66
59	T125-07	F0500	8.80	0.346	1.50	4.92	0.99	3.24
60	T125-08	F0500	8.15	0.321	1.63	5.36	1.22	3.99
61	T125-09	F0500	7.68	0.302	1.49	4.90	1.04	3.40
62	T125-10	F0500	7.62	0.300	1.52	4.99	1.11	3.63
64	T125-11	F1000	8.57	0.338	1.98	6.51	1.30	4.26
65	T125-12	F1000	7.74	0.305	1.82	5.99	1.21	3.96
66	T125-13	F1000	7.41	0.292	1.69	5.55	0.93	3.06
67	T125-14	F1000	7.25	0.285	1.66	5.43	0.85	2.78
68	T125-15	F1000	7.19	0.283	1.71	5.60	0.94	3.08
73	T188-01	F0250	6.21	0.244	1.32	4.33	0.81	2.66
74	T188-02	F0250	6.36	0.251	1.38	4.54	0.91	2.98
75	T188-03	F0250	6.38	0.251	1.39	4.56	0.92	3.01
76	T188-04	F0250	6.34	0.250	1.37	4.48	0.89	2.93
77	T188-05	F0250	6.38	0.251	1.38	4.53	0.93	3.04
78	T188-06	F0500	7.74	0.305	1.75	5.73	1.01	3.31
79	T188-07	F0500	7.15	0.282	1.75	5.74	1.18	3.86
80	T188-08	F0500	7.83	0.308	1.74	5.70	0.89	2.92
81	T188-09	F0500	7.69	0.303	1.81	5.94	1.23	4.05
82	T188-10	F0500	7.37	0.290	1.75	5.76	1.17	3.85
83	T188-11	F1000	7.39	0.291	2.42	7.94	1.51	4.95
84	T188-12	F1000	7.71	0.304	2.42	7.95	1.49	4.89
85	T188-13	F1000	8.05	0.317	2.59	8.48	1.74	5.69
86	T188-14	F1000	7.93	0.312	2.50	8.19	1.60	5.26
87	T188-15	F1000	6.92	0.272	2.44	8.02	1.57	5.15
88	T250-01	F0250	5.66	0.223	1.38	4.51	0.77	2.51

Table 4: Results of Puncture Experiments with Flat-End Probes on Disc Specimens Made from 6061-T651 Plate, Continued

Test	Specimen	Probe Design	Distance Traveled (mm)	Distance Traveled (in)	Impact Velocity, v_i (m/s)	Impact Velocity, v_i (fps)	Puncture Velocity, v_p (m/s)	Puncture Velocity, v_p (fps)
89	T250-02	F0250	5.75	0.226	1.39	4.55	0.74	2.42
90	T250-03	F0250	5.68	0.224	1.38	4.51	0.64	2.10
91	T250-04	F0250	5.63	0.222	1.37	4.50	0.70	2.28
92	T250-05	F0250	6.69	0.264	1.53	5.01	0.86	2.81
94	T250-07	F0500	7.42	0.292	1.96	6.42	1.06	3.47
95	T250-08	F0500	7.34	0.289	1.94	6.37	1.06	3.47
96	T250-09	F0500	7.54	0.297	1.96	6.41	0.94	3.08
97	T250-10	F0500	7.24	0.285	1.94	6.35	1.02	3.36
98	T250-11	F1000	7.59	0.299	2.71	8.90	1.55	5.08
99	T250-12	F1000	8.21	0.323	2.83	9.28	1.63	5.36
100	T250-13	F1000	8.20	0.323	2.95	9.68	1.85	6.06
101	T250-14	F1000	8.37	0.330	2.88	9.45	1.75	5.76
102	T250-15	F1000	7.93	0.312	2.84	9.31	1.74	5.72

Table 5: Total Energy in Puncture Experiments with Flat-End Probes on Disc Specimens Made from 6061-T651 Plate

Test	Specimen	Probe Design	Total Energy Before Impact, $E_{T,i}$ (J)	Total Energy Before Impact, $E_{T,i}$ (ft-lb)	After Puncture, $E_{T,p}$ (J)	After Puncture, $E_{T,p}$ (ft-lb)	Mitigated Energy, E_M (J)	Mitigated Energy, E_M (ft-lb)
35	T063-02	F0250	14.9	11.0	2.2	1.6	12.7	9.4
36	T063-04	F0250	26.8	19.7	14.1	10.4	12.7	9.4
37	T063-05	F0250	24.9	18.3	12.0	8.9	12.9	9.5
38	T063-06	F0250	23.9	17.6	11.3	8.3	12.6	9.3
39	T063-07	F0500	52.3	38.5	29.3	21.6	23.0	16.9
40	T063-08	F0500	47.0	34.6	24.5	18.1	22.5	16.6
41	T063-09	F0500	42.7	31.5	21.2	15.6	21.5	15.9
42	T063-10	F0500	45.5	33.5	23.9	17.6	21.6	15.9
43	T063-11	F1000	96.0	70.8	55.2	40.7	40.8	30.1
44	T063-12	F1000	65.7	48.5	23.1	17.0	42.6	31.5
45	T063-13	F1000	58.1	42.8	16.6	12.3	41.5	30.6
46	T063-14	F1000	55.2	40.7	14.8	10.9	40.4	29.8
47	T063-15	F1000	53.9	39.7	13.3	9.8	40.6	30.0
49	T125-02	F0250	42.9	31.7	0.1	0.1	42.8	31.6
50	T125-03	F0250	55.3	40.8	0.1	0.1	55.2	40.7
51	T125-04	F0250	106.5	78.6	59.6	43.9	46.9	34.6
52	T125-05	F0250	89.8	66.2	46.2	34.1	43.6	32.2
59	T125-07	F0500	162.6	119.9	67.5	49.8	95.1	70.1
60	T125-08	F0500	190.4	140.4	102.6	75.7	87.8	64.8
61	T125-09	F0500	160.2	118.2	74.3	54.8	85.9	63.3
62	T125-10	F0500	166.0	122.5	84.8	62.5	81.3	59.9
64	T125-11	F1000	279.5	206.1	118.7	87.5	160.8	118.6
65	T125-12	F1000	236.8	174.6	101.2	74.7	135.5	100.0

Table 5: Total Energy in Puncture Experiments with Flat-End Probes on Disc Specimens Made from 6061-T651 Plate, Continued

Test	Specimen	Probe Design	Total Energy Before Impact, $E_{T,i}$ (J)	(ft-lb)	After Puncture, $E_{T,p}$ (J)	(ft-lb)	Mitigated Energy, E_M (J)	(ft-lb)
66	T125-13	F1000	204.0	150.4	61.1	45.0	142.9	105.4
67	T125-14	F1000	195.1	143.9	49.4	36.4	145.7	107.5
68	T125-15	F1000	207.8	153.3	61.6	45.4	146.2	107.9
73	T188-01	F0250	126.5	93.3	45.4	33.5	81.1	59.8
74	T188-02	F0250	136.4	100.6	56.4	41.6	80.1	59.0
75	T188-03	F0250	138.4	102.1	57.6	42.5	80.8	59.6
76	T188-04	F0250	133.5	98.4	54.2	40.0	79.3	58.5
77	T188-05	F0250	136.7	100.8	58.2	43.0	78.5	57.9
78	T188-06	F0500	217.6	160.5	73.1	54.0	144.5	106.6
79	T188-07	F0500	217.7	160.6	99.4	73.3	118.3	87.3
80	T188-08	F0500	214.9	158.5	54.4	40.1	160.5	118.4
81	T188-09	F0500	234.1	172.7	109.7	80.9	124.4	91.8
82	T188-10	F0500	219.5	161.9	98.7	72.8	120.9	89.1
83	T188-11	F1000	414.4	305.7	158.5	116.9	256.0	188.8
84	T188-12	F1000	415.1	306.2	144.4	106.5	270.7	199.7
85	T188-13	F1000	469.7	346.4	207.1	152.8	262.6	193.7
86	T188-14	F1000	436.6	322.0	178.0	131.3	258.6	190.7
87	T188-15	F1000	420.6	310.2	177.5	130.9	243.2	179.4
88	T250-01	F0250	135.4	99.8	42.2	31.1	93.2	68.7
89	T250-02	F0250	137.7	101.6	37.4	27.6	100.3	74.0
90	T250-03	F0250	135.4	99.9	29.7	21.9	105.8	78.0
91	T250-04	F0250	135.0	99.6	29.8	22.0	105.2	77.6
92	T250-05	F0250	167.2	123.3	50.6	37.3	116.6	86.0
94	T250-07	F0500	272.6	201.1	80.0	59.0	192.6	142.0
95	T250-08	F0500	268.2	197.8	81.5	60.1	186.7	137.7
96	T250-09	F0500	270.1	199.2	66.7	49.2	203.4	150.0
97	T250-10	F0500	264.5	195.1	78.7	58.0	185.8	137.0
98	T250-11	F1000	518	382	165	122	353	260
99	T250-12	F1000	562	414	187	138	374	276
100	T250-13	F1000	611	451	234	172	377	278
101	T250-14	F1000	584	431	211	156	373	275
102	T250-15	F1000	566	417	214	158	352	259

Stress-Strain Relations in Uniaxial Tension

Figure 25 shows a cube of material with each dimension equal to unity and the engineering stresses that act on it (Ref. 2, p. 53, Fig. 2.15; Ref. 3, p. 94, Fig. 3–1a). Forces act on all six surfaces of this unit volume; these are resolved into components directed normal to the surfaces and tangential to them. The engineering stress produced by each component is the force divided by the surface area; this is true for both normal stresses, denoted $\sigma_{i,j}$, and shear stresses, denoted $\tau_{i,j}$ (Ref. 2, p. 30, Eq. 2.2; Ref. 3, p. 102, Eq. 3–14, 3–15). The indices i and j take on the values x, y, and z to indicate the normal vector of the surface that the stress acts

on and the direction of the stress, in either order. The stresses on opposite surfaces of the volume differ slightly because the state of stress varies spatially.

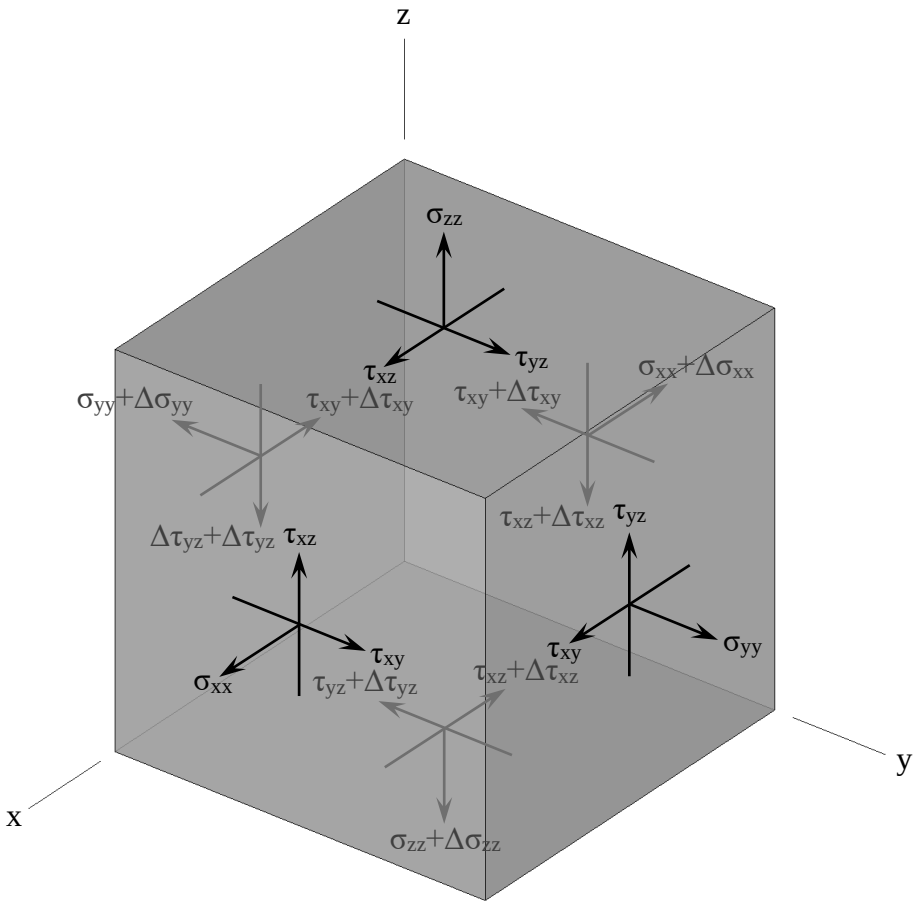

Figure 25: Components of Stress Acting on a Unit Volume

The unit volume deforms elastically and plastically in response to the state of stress. For deformations in which a surface moves in the direction normal to it (Fig. 26a), the engineering strain, labeled $\varepsilon_{i,j}$, is the ratio of the deformation to the dimension of the volume measured normal to the surface. For deformation of a surface in the direction of a vector that lies on the surface (Fig. 26b), the engineering shear strain, denoted $\gamma_{i,j}$, is the change in angle of the adjacent surfaces relative to the surface normal.

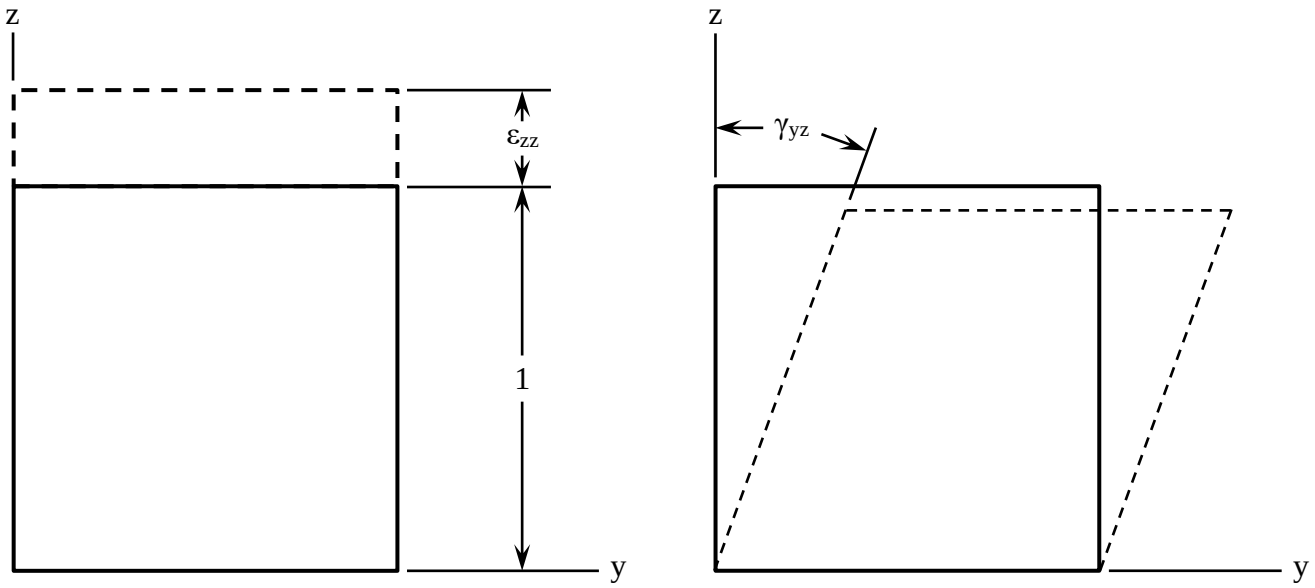

(a) Engineering Normal Strain in z Direction (b) Engineering Shear Strain in yz Plane

Figure 26: Two Types of Strain in Unit Volume

The simplest state of stress has zeros for all of the values except one axial stress. This represents pure uniaxial tension. In a real specimen under uniaxial loading, the internal stress state is more complex, having non-zero values for other components, particularly near boundaries and geometry changes, including reductions of cross-sectional area caused by strain localization. The objective of tension tests is to produce a state of stress that is as close as possible to pure uniaxial tension at the location where fracture initiates. The specimens are designed to fracture in the middle of the gauge section, where the stress is most uniform, by gradually reducing the cross-sectional area toward that location. The stress state approaches uniformity due to the length of the gauge section and Saint-Venant's principle (Ref. 2, p. 240). The state of stress and strain produced by uniaxial tension in the z coordinate direction is given in Table 6 (Ref. 2, p. 97, Eq. a & e; Ref. 3, p. 104, Table 3–1).

Table 6: State of Stress and Strain Corresponding to Tension in z Direction

Stress Component	Value	Strain Component	Value
σ_{xx}	0	ε_{xx}	$-\nu\varepsilon$
σ_{yy}	0	ε_{yy}	$-\nu\varepsilon$
σ_{zz}	σ	ε_{zz}	ε
τ_{xy}	0	γ_{xy}	0
τ_{xz}	0	γ_{xz}	0
τ_{yz}	0	γ_{yz}	0

The relationship between engineering stress and strain is initially elastic, with a constant of proportionality equal to the elastic modulus (E), and then becomes plastic as the material yields and the strain increases beyond the proportional value (Fig. 27a). Most materials harden during plastic deformation, so the stress increases beyond the yield point. As plastic strain accumulates, voids nucleate in the material and coalesce, reducing the engineering stress. When the voids become large enough, a crack propagates through the cross section and the material fractures.

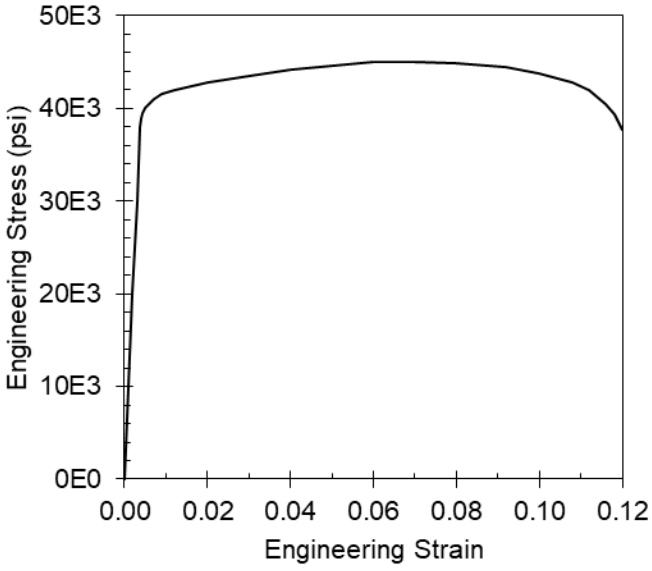

(a) Typical (Ref. 4, p. 3-479, Fig. 3.6.2.2.6(l))

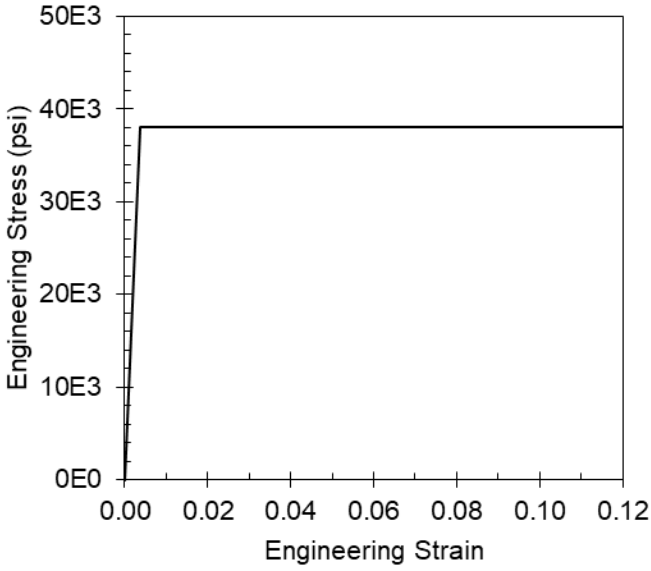

(b) Perfectly Plastic

Figure 27: Examples of Engineering Stress-Strain Relations

The ultimate values of the engineering stress and strain are the maximum values over the range from the unloaded state until the specimen fractures. These values are often cited as test results. The ultimate engineering stress (σ_u) is also referred to as the ultimate tensile strength (UTS or F_{tu}). The ultimate engineering strain (ε_u) is cited in some sources as the elongation and is often expressed as a percentage, although strain is a dimensionless quantity. Given the stress-strain relation, $\sigma(\varepsilon)$, and the ultimate strain, ε_u, the strain energy in the unit volume when it fractures is

$$E_u = \int_0^{\varepsilon_u} \sigma \, d\varepsilon \tag{8}$$

The resulting energy per unit volume has units of force/length^2 but may be multiplied by the volume (1) to obtain the energy with units of force×length. Under the assumption of perfect plasticity (Fig. 27b), the yield and ultimate strengths are equal, the material yields when the strain is $\frac{\sigma_y}{E}$, and the strain energy in a unit volume of material when it fractures in tension is

$$E_u = E_e + E_p = \frac{\sigma_y}{2}\left(\frac{\sigma_y}{E}\right) + \sigma_y\left(\varepsilon_u - \frac{\sigma_y}{E}\right) = \sigma_y\left(\varepsilon_u - \frac{\sigma_y}{2E}\right) \quad (9)$$

This equation is dominated by the plastic strain energy (E_p) because the plastic strain at fracture $\left(\varepsilon_u - \frac{\sigma_y}{E}\right)$ is much greater than the elastic strain at yield $\left(\frac{\sigma_y}{E}\right)$.

The ultimate engineering stress and strain were measured from uniaxial tension specimens (Fig. 28) of the same stock material as the disc specimens (Fig. 1–4). Fifteen tests were performed at an average quasi-static rate of 729E-6/s and ambient temperature (77°F, 25°C). Five specimens aligned with each of the three orthogonal grain directions. The engineering stress-strain relations are plotted in Figure 29. The average ultimate stress is 46.8E3 psi (322 MPa) and the average ultimate strain is 143E-3.

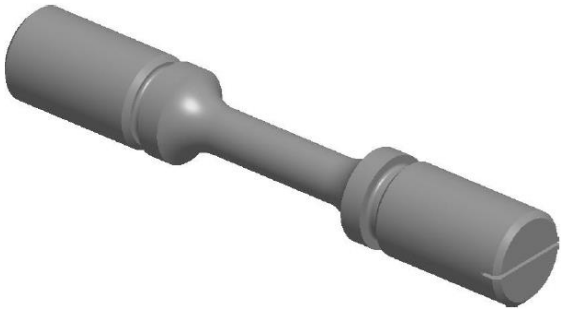

Figure 28: 6061-T651 Aluminum Uniaxial Tension Specimen with Diameter of 0.250 Inch

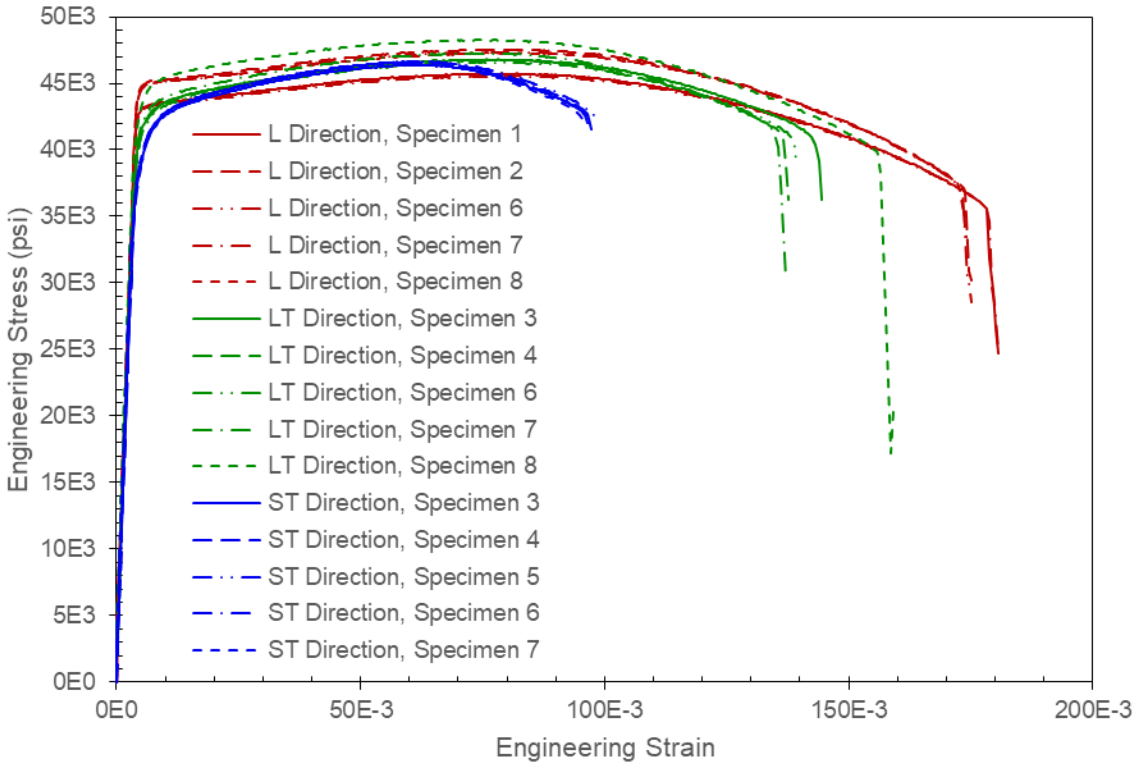

Figure 29: Engineering Stress-Strain Relations for 6061-T651 Plate

Empirical Model for Energy Mitigated During Puncture Event

The sample size for each combination of geometric parameters (4–5) is too small to apply classical statistical inference techniques with reasonable confidence in the results. However, the empirical model for puncture energy provided by Reference 5 calculates the lower bounds of confidence intervals based on the entire collection of data.

Reference 5 suggests that the total energy required for a cylindrical probe with a flat end to puncture a metal sheet or plate is a function of the ultimate tensile strength, engineering strain at fracture, specimen thickness, and probe diameter. The product of the ultimate engineering stress and strain is a simple estimate for the area under the stress-strain relation. Assuming perfect plasticity ($\sigma_u = \sigma_y$), this product ($\sigma_u\varepsilon_u$) is the dominant term in Equation 9 and approximates the strain energy in a unit volume of the material when it ruptures in tension. This same product is the area of a rectangle that envelops the actual stress-strain relation, so it exceeds the area underneath, but it is correlated to experimental data.

In order for the probe to penetrate the specimen, the material in some volume must fracture. In all of the puncture experiments, the probes are observed to eject circular plugs from the disc specimens, of which Figures 10 through 21 are representative. Figure 30 illustrates a hypothetical estimate for the volume of the fractured material between the probe diameter (d) and an additional radial width (w), in which the plastic strain is concentrated, and extending through the specimen thickness (t); the volume evaluates to $\pi t(dw + w^2)$. However, the state of stress in this volume is much more complex than uniaxial tension, and additional material surrounding this volume has strain energy due to biaxial tension, bending, and shear.

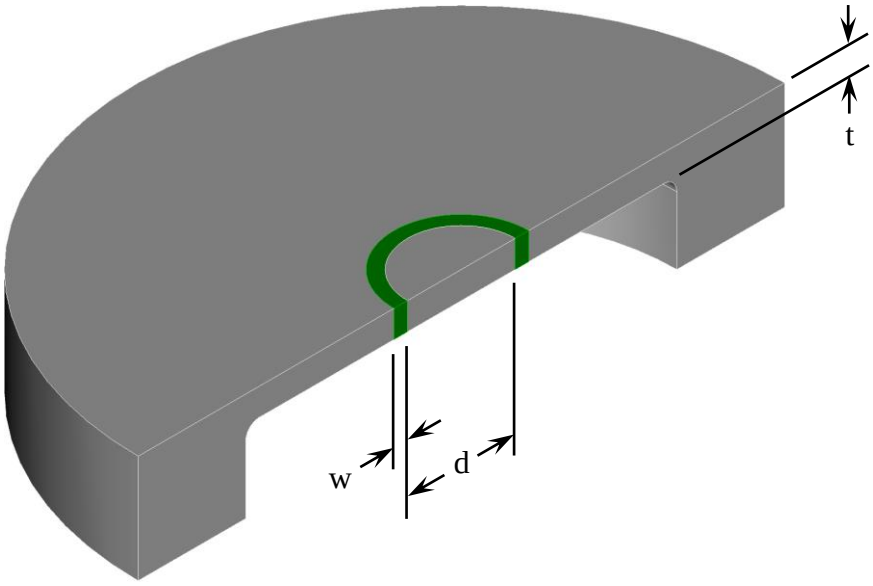

Figure 30: Half of Volume of Disc Specimen that Ruptures as Probe Penetrates

The objective is to calculate the energy expended by the probe as it penetrates the specimen. One way to obtain the energy (with units of force×length) is to multiply the product of the ultimate engineering stress and strain (which has units of stress, force/length^2) by the volume of material that ruptures (with units of length^3). The volume is hypothesized to be a combination of the specimen thickness and probe diameter, but the balance between these two parameters is determined empirically rather than by postulating the shape of the fractured volume. The other dimensions of the specimen are neglected because fracture is

assumed to be a local phenomenon. This simple approach minimizes the number of input parameters and neglects the complex state of stress and strain within the specimen. It also avoids the uncertainty in the volume of material that ruptures when cracks propagate along more complicated paths than circles.

Reference 5 proposes an empirical fit equation that calculates a lower bound for the energy measured in multiple puncture tests with specimens of different alloys and thicknesses and probes of different diameters but the same shape (Ref. 5, p. 2, Eq. 3 and 4):

$$E = K \sigma_u \varepsilon_u t^3 \left(\frac{d}{t}\right)^c \tag{10}$$

where E is the total energy mitigated by the specimen as the probe punctures it, σ_u is the ultimate engineering stress (tensile strength), ε_u is the ultimate engineering strain (elongation), t is the specimen thickness, and d is the probe diameter. The dimensionless coefficient (K) is derived statistically such that the equation calculates a lower bound at a specified confidence level. The exponent (c) is fit to the data; it specifies how much influence the probe diameter has on the energy. Dimensional analysis requires that the total exponent on all of the parameters with length units be +3. The effective exponent on the thickness is 3−c, which balances the equation to yield the correct dimensions for energy. If the diameter of the pocket were included in the equation, it would add a parameter and another calibrated exponent; the simplicity of the equation is considered more beneficial than including a term to account for the general deformation of the specimen.

Equation 10 expresses the mitigated energy as a function of both the specimen thickness and the probe diameter. It can be plotted in three dimensions, but multiple surfaces that serve as lower bounds with different confidence levels are difficult to visualize. Optimization of the parameters to fit the equation to the data is facilitated by normalizing the inputs and output such that there is only one input and the function can be plotted in two dimensions. The mitigated energy is normalized by the strain energy of the unit volume at fracture and the cube of the thickness to create a non-dimensional parameter (Ref. 5, p. 2, Eq. 4),

$$E_n = \frac{E}{\sigma_u \varepsilon_u t^3} \tag{11}$$

The diameter-to-thickness ratio (also non-dimensional) is defined as

$$M = \frac{d}{t} \tag{12}$$

Substituting Equations 11 and 12 into Equation 10 yields the exponential function (Ref. 5, p. 2, Eq. 3)

$$E_n = K M^c \tag{13}$$

Whereas Equation 10 directly depends on two parameters (d, t) of the experimental scenario, Equation 13 has only one input (M, Eq. 12) that differs between tests. The result of Equation 10 compares to the actual energy (E) from the tests, but Equation 13 is compared to the normalized energy (E_n, Eq. 11). Simple two-dimensional plots compare the results of Equations 11 and 13 for any values of the coefficient (K) and exponent (c), which are optimized such that the model best fits the data. The exponential equation (Eq. 13) is written in the form of a linear equation (Ref. 6, p. 2, Eq. 1) by taking common logarithms of both sides (Ref. 5, p. 2, Eq. 5):

$$\log E_n = \log K + c \log M \tag{14}$$

Let n be the number of data points, j = 1…n the index of the data, d_j the diameter data, t_j the thickness data, M_j the measured diameter-to-thickness ratios (Eq. 12), and E_j the mitigated energy data. The normalized energy that results from Equation 11 when it is evaluated with the experimental data is denoted $E_{n,d,j}$. When Equation 13 is evaluated with the parameters of the linear fit and the diameter-to-thickness ratios (M_j), the result is designated $E_{n,f,j}$. A line is fit to the common logarithms of the normalized energy and diameter-to-thickness ratio such that the sum of the squares of the residuals, $\sum_{j=1}^{n}\left(\log E_{n,d,j} - \log E_{n,f,j}\right)^2$, is minimized. The parameters are defined by Equations 15 and 16 (Ref. 7, p. 135, Eq. 4.37; Ref. 8, p. 353, Eq. 5.4; Ref. 9, p. 502), which evaluate to K = 9.929 and c = 1.1154. The data and fit line are plotted in Figure 31.

$$\log K = \frac{\sum_{j=1}^{n}\left(\log M_j\right)\sum_{j=1}^{n}\left(\log M_j \log E_{n,d,j}\right) - \sum_{j=1}^{n}\left(\log M_j\right)^2 \sum_{j=1}^{n}\left(\log E_{n,d,j}\right)}{\left[\sum_{j=1}^{n}\left(\log M_j\right)\right]^2 - n\sum_{j=1}^{n}\left(\log M_j\right)^2} \tag{15}$$

$$c = \frac{\sum_{j=1}^{n}\left(\log M_j\right)\sum_{j=1}^{n}\left(\log E_{n,d,j}\right) - n\sum_{j=1}^{n}\left(\log M_j \log E_{n,d,j}\right)}{\left[\sum_{j=1}^{n}\left(\log M_j\right)\right]^2 - n\sum_{j=1}^{n}\left(\log M_j\right)^2} \tag{16}$$

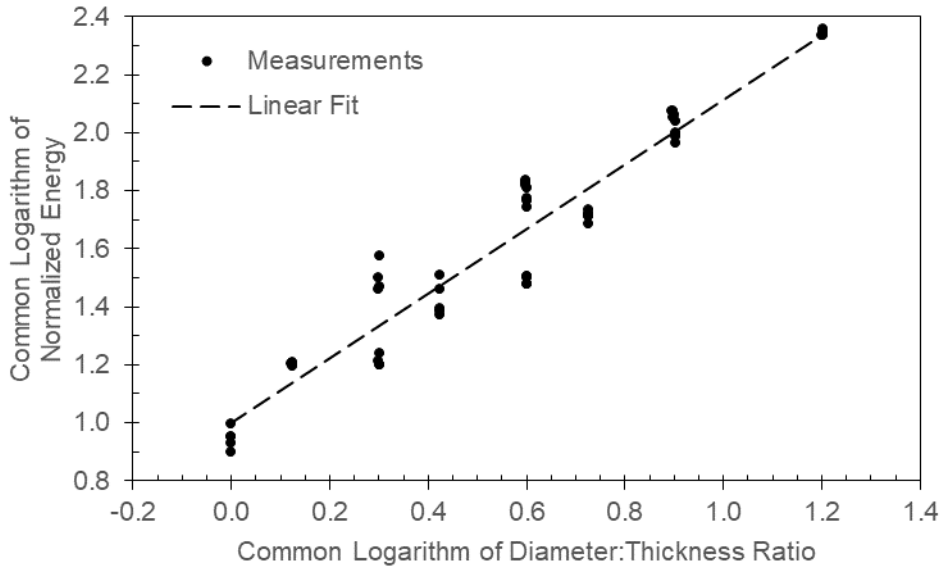

Figure 31: Linear Fit to Logarithms of Normalized Energy and Diameter-to-Thickness Ratio

The mean of the common logarithms of the normalized energy data is (Ref. 7, p. 121, Eq. 4.14a; Ref. 9, p. 264, Eq. 8.2.1)

$$E_{l,n,d} = \frac{1}{n}\sum_{j=1}^{n}\log E_{n,d,j} \tag{17}$$

and the variance is (Ref. 7, pp. 121, 136, Eq. 4.14b; Ref. 9, p. 266, Eq. 8.2.7)

$$S_E^2 = \frac{1}{n-1}\sum_{j=1}^{n}\left(\log E_{n,d,j} - E_{l,n,d}\right)^2 \tag{18}$$

The degrees of freedom (ν) are the number of data points less the number of coefficients in the polynomial fit (Ref. 7, p. 134):

$$\nu = n - 2 \tag{19}$$

The standard error of the linear fit compares the model to the data in terms of the logarithms of the normalized energy values (Ref. 7, p. 133, Eq. 4.34; Ref. 9, p. 502):

$$S_F = \sqrt{\frac{1}{\nu}\sum_{j=1}^{n}\left(\log E_{n,d,j} - \log E_{n,f,j}\right)^2} \tag{20}$$

The correlation coefficient is (Ref. 7, p. 135, Eq. 4.38; Ref. 8, p. 332; Ref. 9, p. 178, Eq. 5.3.1)

$$R^2 = 1 - \frac{S_F^2}{S_E^2} = 1 - \frac{(n-1)\sum_{j=1}^{n}\left(\log E_{n,d,j} - \log E_{n,f,j}\right)^2}{(n-2)\sum_{j=1}^{n}\left(\log E_{n,d,j} - E_{l,n,d}\right)^2} \tag{21}$$

which evaluates to 0.926.

The Student's t distribution predicts the coefficients (K) at different confidence values based on the number of degrees of freedom. If the sample size were infinite, the normal distribution would define the coefficient at any confidence value (C). The Student's t distribution accounts for additional uncertainty with finite samples and converges to the normal distribution as the degrees of freedom approach infinity. For the 55 samples in this data set (53 DoF) and 95% confidence, the difference between the one-tailed bounds is 1.8%; the difference would be less than 5% for 22 samples (20 DoF) or 1% for 96 samples (94 DoF).

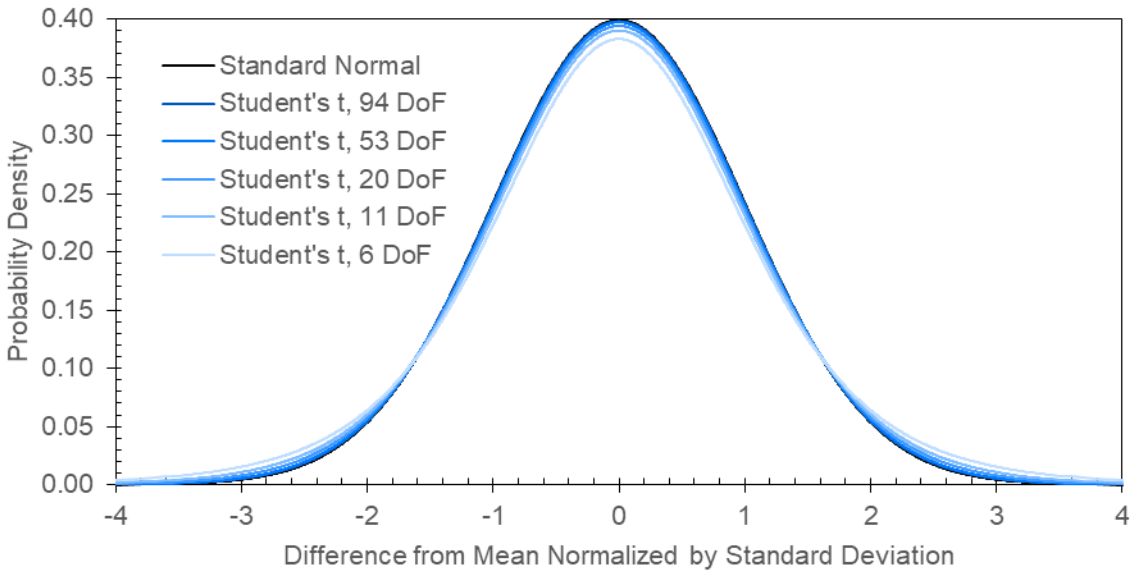

Figure 32: Convergence of Student's t and Normal Probability Density Functions

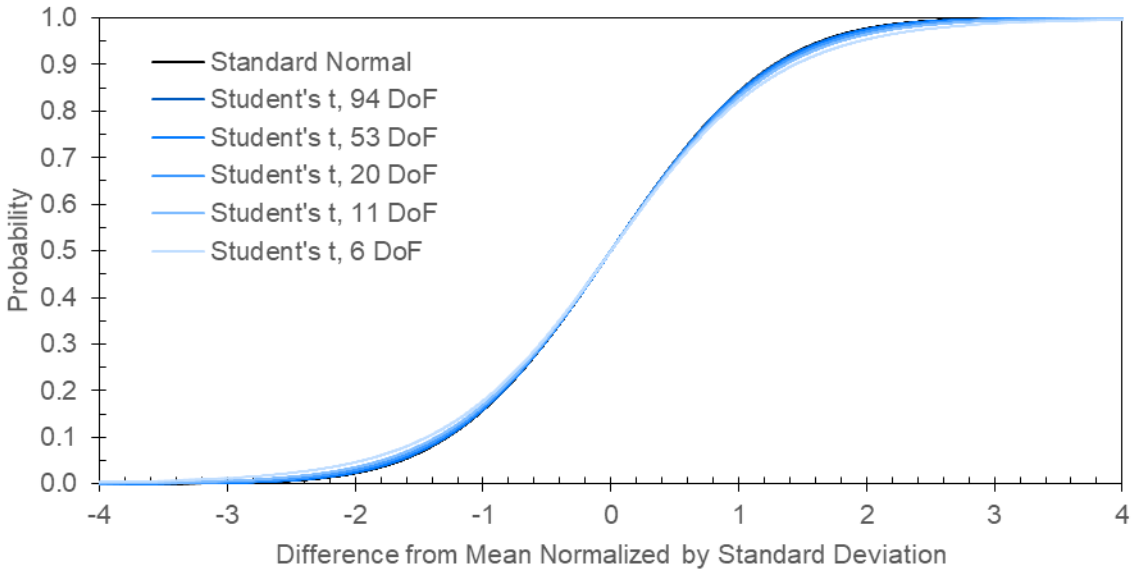

Figure 33: Convergence of Student's t and Normal Cumulative Distribution Functions

The PDF can be written (Ref. 9, p. 274, Eq. 8.4.2)

$$f(x) = \frac{\Gamma\left(\frac{\nu+1}{2}\right)}{\Gamma\left(\frac{\nu}{2}\right)\sqrt{\pi\nu\left(1+\frac{x^2}{\nu}\right)^{\nu+1}}} = \frac{\Gamma\left(\frac{\nu+1}{2}\right)}{\sqrt{\pi\nu}\,\Gamma\left(\frac{\nu}{2}\right)}\left(1+\frac{x^2}{\nu}\right)^{-\frac{\nu+1}{2}} \tag{22}$$

or

$$f(x) = \frac{1}{B\left(\frac{1}{2},\frac{\nu}{2}\right)\sqrt{\nu\left(1+\frac{x^2}{\nu}\right)^{\nu+1}}} = \frac{1}{\sqrt{\nu}\,B\left(\frac{1}{2},\frac{\nu}{2}\right)}\left(1+\frac{x^2}{\nu}\right)^{-\frac{\nu+1}{2}} \tag{23}$$

The gamma function in Equation 22 is (Ref. 8, p. 222; Ref. 9, p. 111, Eq. 3.3.4)

$$\Gamma(\gamma) = \int_0^\infty u^{\gamma-1}e^{-u}du \tag{24}$$

and the beta function in Equation 23 is (Ref. 8, p. 226)

$$B(\beta_1,\beta_2) = \int_0^1 u^{\beta_1-1}(1-u)^{\beta_2-1}du \tag{25}$$

The CDF is the integral of the PDF from negative infinity to the non-dimensional limit parameter t and may be written in terms of gamma functions by placing Equation 22 in the integral or in terms of beta functions by substituting $u = \frac{\nu}{x^2+\nu}$ into Equation 23.

$$p = C = \frac{\Gamma\left(\frac{\nu+1}{2}\right)}{\sqrt{\pi\nu}\,\Gamma\left(\frac{\nu}{2}\right)}\int_{-\infty}^{t}\left(1+\frac{x^2}{\nu}\right)^{-\frac{\nu+1}{2}}dx \tag{26}$$

or

$$p = C = \begin{cases} \dfrac{\int_0^{\frac{\nu}{t^2+\nu}} u^{\frac{\nu}{2}-1}(1-u)^{-\frac{1}{2}}du}{2\int_0^1 u^{\frac{\nu}{2}-1}(1-u)^{-\frac{1}{2}}du} & t < 0 \\ 1 - \dfrac{\int_0^{\frac{\nu}{t^2+\nu}} u^{\frac{\nu}{2}-1}(1-u)^{-\frac{1}{2}}du}{2\int_0^1 u^{\frac{\nu}{2}-1}(1-u)^{-\frac{1}{2}}du} & t \geq 0 \end{cases} \quad (27)$$

The probability (p) at which the CDF is evaluated equals the confidence (C) because a one-tailed bound is desired with that probability of bounding future observations. The objective is to make accurate predictions, so the desired probability is between 0.5 and 1. One of Equations 27 or 26 is solved for the parameter t, which is positive for any probability greater than 0.5. The confidence interval for the logarithm of the coefficient is (Ref. 7, p. 134, Eq. 4.35)

$$\log b_L = \log K - t\, S_F \leq \log K \leq \log K + t\, S_F = \log b_U \quad (28)$$

The lower bound on the coefficient (K) simplifies to

$$b_L = \frac{K}{10^{t\, S_F}} \quad (29)$$

Table 7 lists the Student's t parameter and the coefficient at several specific confidence levels. The bounding probability refers to the chance that a future test performed under identical conditions would result in a lower energy value than the model predicts with the calculated coefficient. The value at which the standard normal cumulative distribution function equals the confidence is provided for comparison to the parameter t; the relative difference is the effect of the limited sample size. Probabilities of one per million or billion are included because they define screening thresholds in Reference 10, page 2.

Table 7: Lower Bounds of Confidence Intervals on Coefficient Optimized to Linear Equation and Flat-End Probe Data

Probability of Lower Future Observation		Confidence	Standard Normal Distribution	Student's t Parameter	Relative Difference	Coefficient, K
500E-3	50%	50%	0	0	0%	9.929
100E-3	10%	90%	1.2816	1.2977	1.26%	7.179
50E-3	5%	95%	1.6449	1.6741	1.78%	6.535
10E-3	1%	99%	2.326	2.399	3.1%	5.452
1E-3	0.1%	99.9%	3.090	3.251	5.2%	4.406
1E-6	0.0001%	99.9999%	4.753	5.338	12.3%	2.616
1E-9	0.0000001%	99.9999999%	5.998	7.219	20%	1.6346

Figures 34 and 35 plot the empirical model with the coefficients in Table 7 and the exponent 1.1154 (p. 29) at several confidence levels. The experimental data are plotted with solid circles. In order to display multiple confidence levels on two-dimensional plots, the model and data are expressed in terms of the diameter-to-thickness ratio (M) and the normalized energy (E_n). Figure 36 plots the mitigated energy (E) as a function of the specimen thickness (t) and probe diameter (d), but only with the median value of the coefficient (K) so that this plot is also two-dimensional. Note that the data tend to be at opposite ends of the abscissas in these two plots because the abscissa in the first plot (Fig. 34) is inversely related to the

thickness, whereas the abscissa in the second plot (Fig. 36) is the thickness. The median curve appears to match the data more closely in the plot with non-dimensional axes (Fig. 34) than in the one with units of length and energy (Fig. 36). The difference is particularly pronounced for large diameters and thicknesses. This is simply due to the method of optimizing the parameters of the non-dimensional linear equation (Eq. 14) rather than the non-linear equation (Eq. 10) for the empirical model.

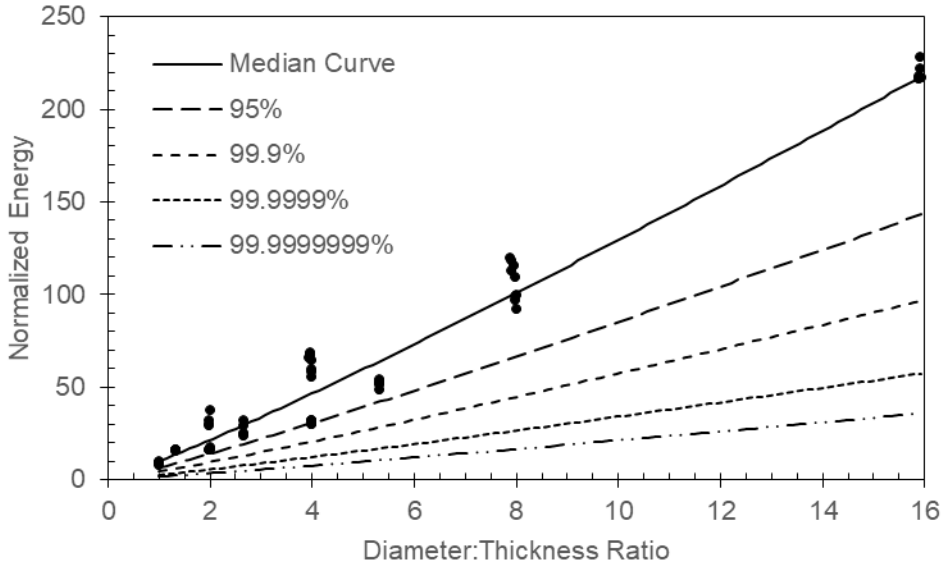

Figure 34: Empirical Model Showing Full Range of Diameter:Thickness Ratios

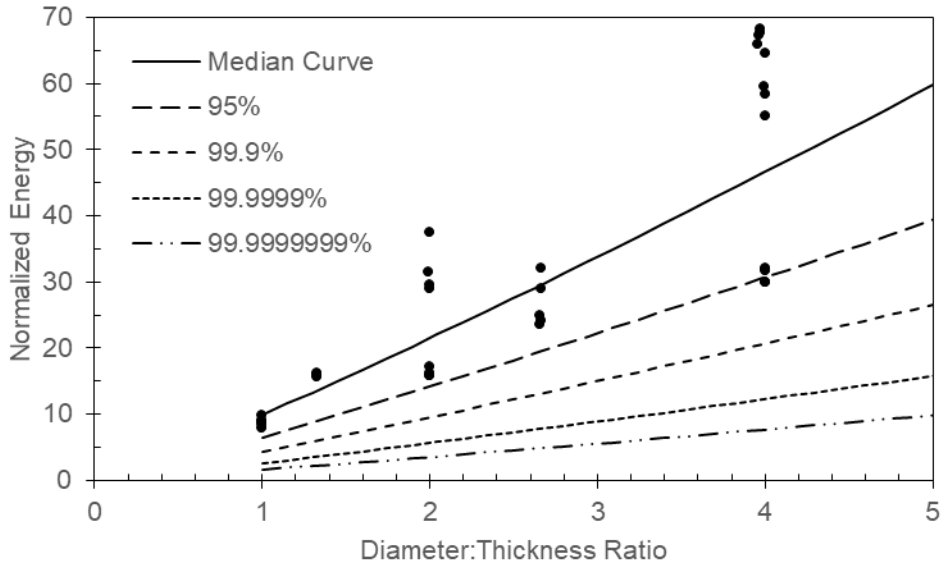

Figure 35: Empirical Model Focused on Small Diameter:Thickness Ratios

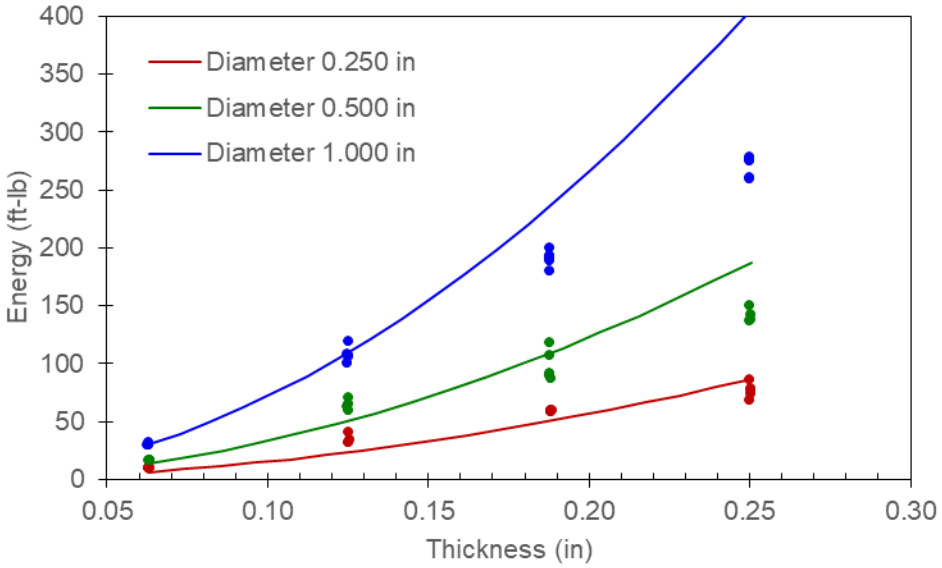

Figure 36: Empirical Model with Linearly Optimized Parameters Compared to Actual Mitigated Energy

The calibration of the empirical model alleviates error due to the simplicity of the equation. It does not reduce uncertainty in the dimensions and material properties that are provided as inputs. The statistical confidence intervals encompass differences between the properties of each specimen that was tested and the boundary conditions of the experiments that comprise the data set. However, differences between the experimental boundary conditions and those of an intended application are not accounted for. The confidence limits only bound the experiments that form the basis of the model. Engineering judgement is required to apply the results of the empirical model to specific applications.

Optimal Parameters of Non-linear Equation for Mitigated Energy

Numerical methods exist for multi-variate non-linear optimization such that the coefficient (K) and exponent (c) in Equation 10 may be found without writing it in non-dimensional linear form (Eq. 14), but they are too lengthy to present here. A coefficient (K) of 7.599 and exponent (c) of 1.0935 minimize the sum of the squares of the residuals of the mitigated energy relative to the data in Table 5. Table 8 lists the lower bounds for the coefficient at several specific confidence levels, which are calculated with Equations 20, 26, and 29.

Table 8: Lower Bounds of Confidence Intervals on Coefficient Optimized to Non-linear Equation and Flat-End Probe Data

Probability of Lower Future Observation		Confidence	Coefficient, K
500E-3	50%	50%	7.599
100E-3	10%	90%	4.571
50E-3	5%	95%	3.945
10E-3	1%	99%	2.970
1E-3	0.1%	99.9%	2.127
1E-6	0.0001%	99.9999%	0.9393
1E-9	0.0000001%	99.9999999%	0.4495

Figures 37 and 38 plot the empirical model in terms of the diameter-to-thickness ratio (M) and the normalized energy (E_n) at several confidence levels, based on the coefficients in Table 8 and the exponent 1.0935 (p. 34); the solid circles are the experimental data. Figure 39 plots the empirical model in terms of the mitigated energy (E), specimen thickness (t), and probe diameter (d), but only with the median value of the coefficient (K) in Table 8. With the parameters optimized to the non-linear equation (Eq. 10), the median curve appears to match the data more closely in the plot with units of length and energy (Fig. 39) than in the one with non-dimensional axes (Fig. 37). The difference is particularly pronounced for large diameters and thicknesses.

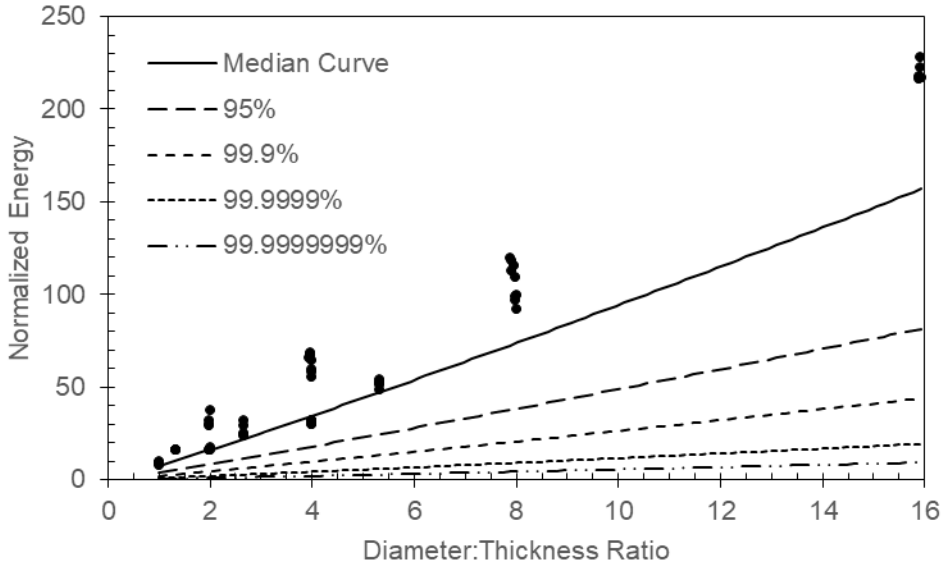

Figure 37: Empirical Model with Non-linearly Optimized Parameters Showing Full Range of Diameter:Thickness Ratios

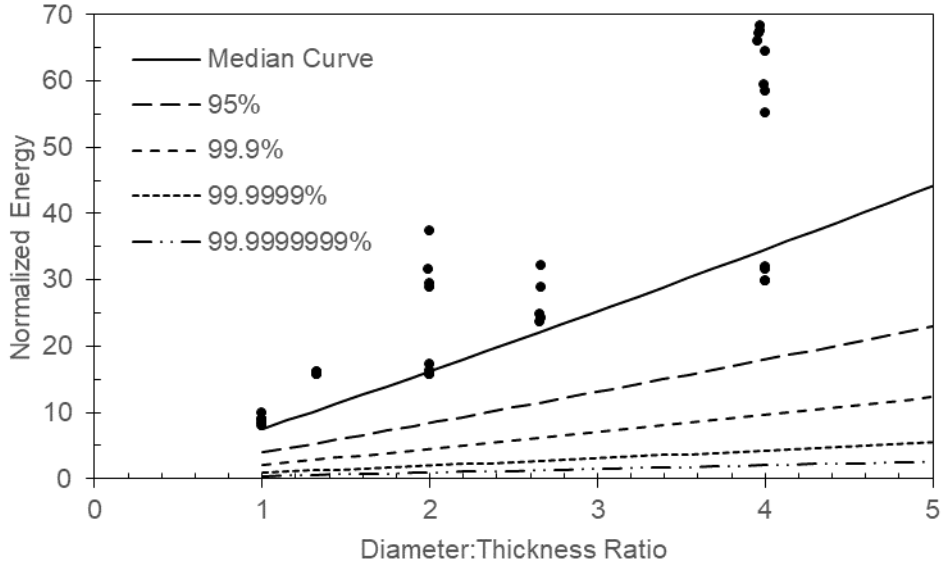

Figure 38: Empirical Model with Non-linearly Optimized Parameters Focused on Small Diameter:Thickness Ratios

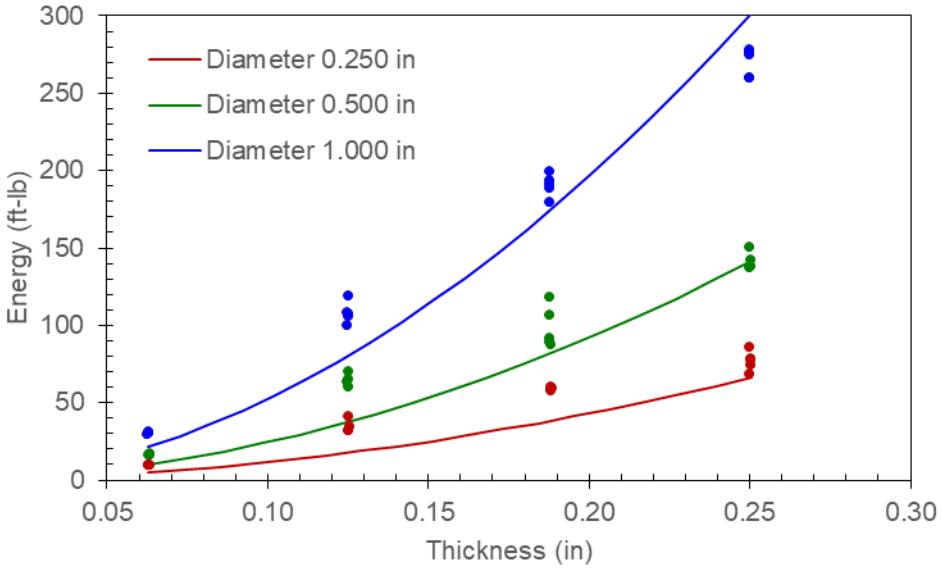

Figure 39: Empirical Model with Non-linearly Optimized Parameters Compared to Actual Mitigated Energy

With the parameter values reported on page 29, which are optimized to the linear equation (Eq. 14), the median curve shows a closer fit to the data in Figure 34 than in Figure 37. Both of these plots have non-dimensional axes and concentrate the mitigated energy data from the thickest specimens in the lower-left region. With the parameter values (p. 34) optimized to the non-linear equation (Eq. 10), the median curve shows a closer fit to the data in Figure 39 than in Figure 36. These plots have axes with units of length and energy, so the data from the thickest specimens appear on the right. The non-linear optimization method weights the data differently than the linear regression method, which normalizes the mitigated energy data with Equation 11 and applies a logarithmic transformation with Equation 14 prior to computing the residuals in Equation 20. Each method minimizes the sum of the squares of the residuals between the empirical model and the data, but the cube of the thickness in Equation 11 and the logarithm function in Equation 14 affect the residuals. Terms in Equation 11 (σ_u, ε_u) that do not vary between tests have no effect on the optimization process. Dividing the mitigated energy by the cube of the specimen thickness gives more weight to thin specimens. Taking the logarithm of the normalized energy gives less weight to large normalized energy values, which correspond to large probe diameters and thin specimens. Although the results differ, both methods are acceptable.

Conclusion

Experiments were performed to measure the total energy mitigated by specimens of 6061-T651 plate as cylindrical bars of AISI 4340 steel punctured them. The specimens were all cut from the same stock material but with four thicknesses in the zone where the probes penetrated them. The nominal thicknesses differed by 1.588 mm (0.0625 in): 1.59 mm, 3.18 mm, 4.76 mm, and 6.35 mm (0.063 in, 0.125 in, 0.188 in, and 0.250 in). The puncture probes were all right circular cylinders but had three diameters that differed by a factor of 2: 6.35 mm, 12.70 mm, and 25.40 mm (¼ in, ½ in, and 1 in). The remaining geometric parameters of the specimens and boundary conditions were equal in all of the experiments.

The experimental data are processed to determine the total energy (potential and kinetic) that was mitigated by each specimen as the probe passed through it. An empirical model (Eq. 10)

is calibrated to the data for the purpose of predicting the energy mitigated by intermediate combinations of specimen thickness and probe diameter. The model accounts for the variation in these inputs by applying exponents to them and ensuring that the exponents sum to the required number of length dimensions. This constraint reduces the empirical fit parameters to one coefficient and one exponent. The model combines the specimen thickness and probe diameter with two material properties, the ultimate strength and strain, such that the output is the mitigated energy. Table 9 summarizes the lower bounds on the optimal parameters for both the linear and non-linear forms of the empirical model (Eq. 14 and 13, respectively). Probabilities of one per thousand, million, or billion are included for convenience; however, these lower bounds are considered uncertain because they would change significantly if additional specimens were tested. The exponent is included in the table for completeness, although it is a constant.

Table 9: Parameters of Empirical Model for Energy Mitigated by 6061-T651 Plate When Punctured by Flat-End Probe

		Optimized to Linear Equation		Optimized to Non-linear Equation	
Bounding Probability	Confidence	Coefficient, K	Exponent, c	Coefficient, K	Exponent, c
Median	50%	9.929	1.1154	7.599	1.0935
One in Ten	90%	7.179	1.1154	4.571	1.0935
One in Twenty	95%	6.535	1.1154	3.945	1.0935
One in One Hundred	99%	5.452	1.1154	2.970	1.0935
One in One Thousand	99.9%	4.406	1.1154	2.127	1.0935
One in One Million	99.9999%	2.616	1.1154	0.9393	1.0935
One in One Billion	99.9999999%	1.6346	1.1154	0.4495	1.0935

Uncertainty in the measurements of the energy mitigated by each specimen is due to the accuracy of the laser interferometers, machining tolerances, spatial variation in material properties (non-homogeneity), and the stochastic nature of ductile fracture. The acceleration data serves as a trigger for selecting the time ranges over which to average the total energy, but the energy is calculated solely from position data, and the trigger times are adjusted such that the intervals appear reasonable on the total energy plot. Therefore, error in the accelerometer has no influence on the test results. The specimens are manufactured with reasonable tolerances and surface roughness limits for milling operations. The variation in thickness can be as much as 3% and remain within tolerance limits. The hardness of 6061-T651 aluminum has been shown to vary by 9% through the thickness of a plate (Ref. 11). Ductile fracture occurs when voids form in the material and coalesce into cracks. The locations of voids and the reduction in the engineering strength as they grow and combine depend on the microstructure, which is not known before a component fractures and is, therefore, assumed to be homogeneous. Uncertainty about the microstructure makes the crack paths appear random although they follow patterns based on the boundary conditions.

There is also uncertainty in applying the empirical model to metal alloys of particular ultimate strengths and strains. There is measurement error in determining the material properties, both of the alloy that was tested and the subject to which the empirical model is applied. These errors may augment or reduce each other. The form of the stress-strain relation varies from one alloy to another, and the empirical model does not account for it. The experiments were performed with specimens from the same stock material, so they experienced the same heat treatments. This minimized the variance and maximized the energy at each confidence level; however, it also neglected differences between heat

treatment lots and material production batches. Evaluating the empirical model with parameters fit to data from multiple sources, as in Reference 5, would reduce this unconservative bias.

References

1. Waymel, R., “MIP Puncture Disc Results,” Sandia National Laboratories, 15 July 2020.
2. Boresi, A. P., Schmidt, R. J., and Sidebottom, O. M., *Advanced Mechanics of Materials*, 5th ed., John Wiley & Sons, 1993.
3. Shigley, J. E., and Mischke, C. R., *Mechanical Engineering Design*, McGraw-Hill, 2001.
4. Battelle Memorial Institute, MMPDS-17, “Metallic Materials Properties Development and Standardization (MMPDS),” 1 July 2022.
5. Corona, E., SAND2020-12660R, “Empirical Formula for Puncture Energy of Flat Plates by a Cylindrical Punch,” Sandia National Laboratories, 6 November 2020.
6. Lay, D. C., *Linear Algebra and its Applications*, 1st ed., Addison-Wesley, 1994.
7. Figliola, R. S., and Beasley, D. E., *Theory and Design for Mechanical Measurements*, 3rd ed., John Wiley & Sons, 2000.
8. Ross, S., *A First Course in Probability*, 5th ed., Prentice Hall, 1998.
9. Bain, L. J., and Engelhardt, M., *Introduction to Probability and Mathematical Statistics*, 2nd ed., Duxbury Press, 1992.
10. Department of Energy, DOE-NA-STD-3016-2023, “Hazard Analysis Reports for Nuclear Explosive Operations,” 2023.
11. Kramer, S., Antoun, B., Lu, W., Jones, A., Sanborn, B., Song, B., Jin, H., and Deibler, L., SAND2019-10152PE, “DE L2 Milestone Presentation: Ductile Failure,” Sandia National Laboratories, 21 August 2019.

Appendix A: Acceleration

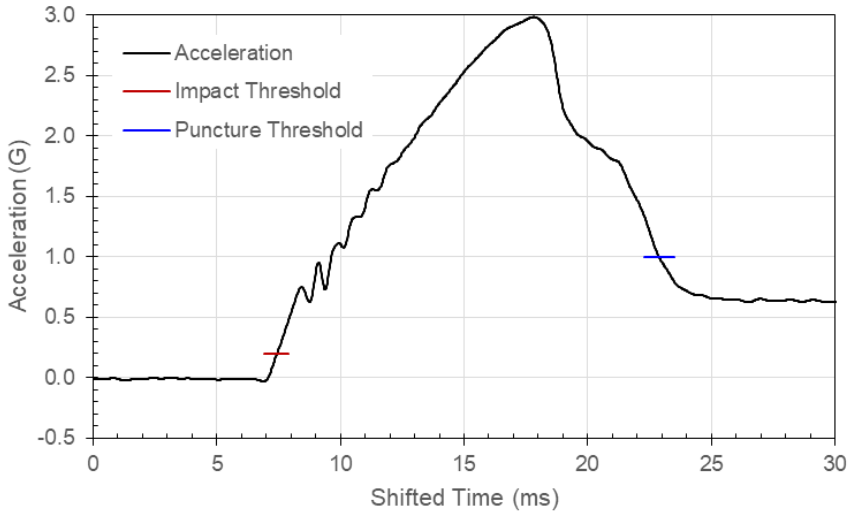

Figure 40: Carriage Acceleration in Test 35 with Specimen T063-02 and 0.250-Inch Probe

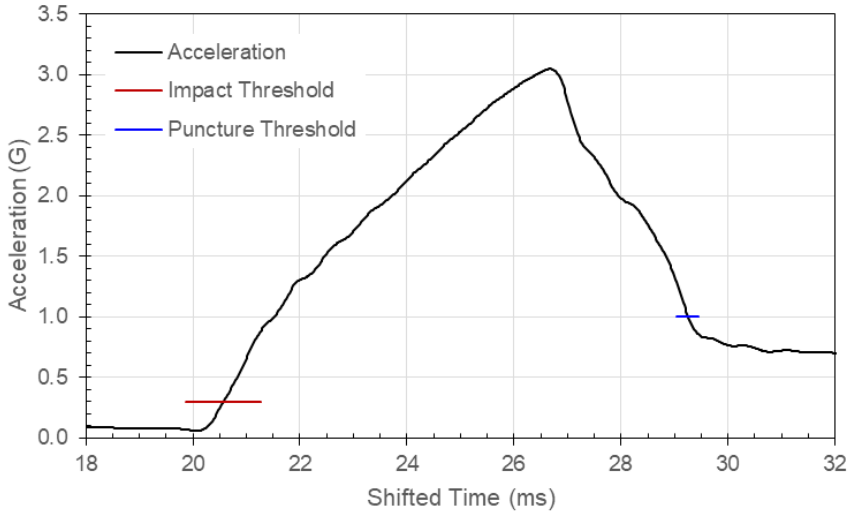

Figure 41: Carriage Acceleration in Test 36 with Specimen T063-04 and 0.250-Inch Probe

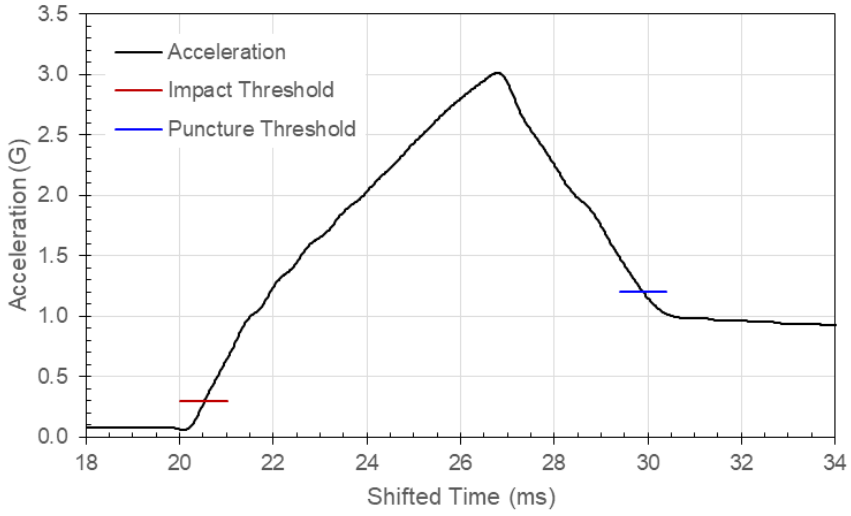

Figure 42: Carriage Acceleration in Test 37 with Specimen T063-05 and 0.250-Inch Probe

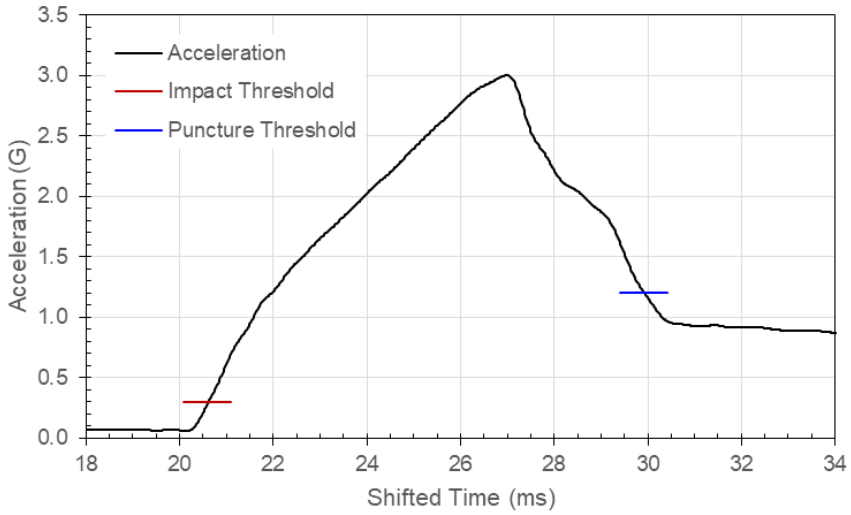

Figure 43: Carriage Acceleration in Test 38 with Specimen T063-06 and 0.250-Inch Probe

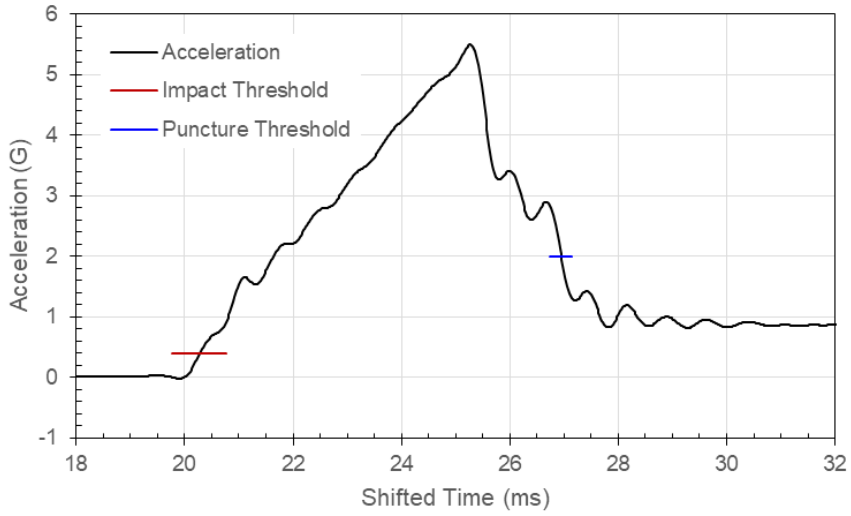

Figure 44: Carriage Acceleration in Test 39 with Specimen T063-07 and 0.500-Inch Probe

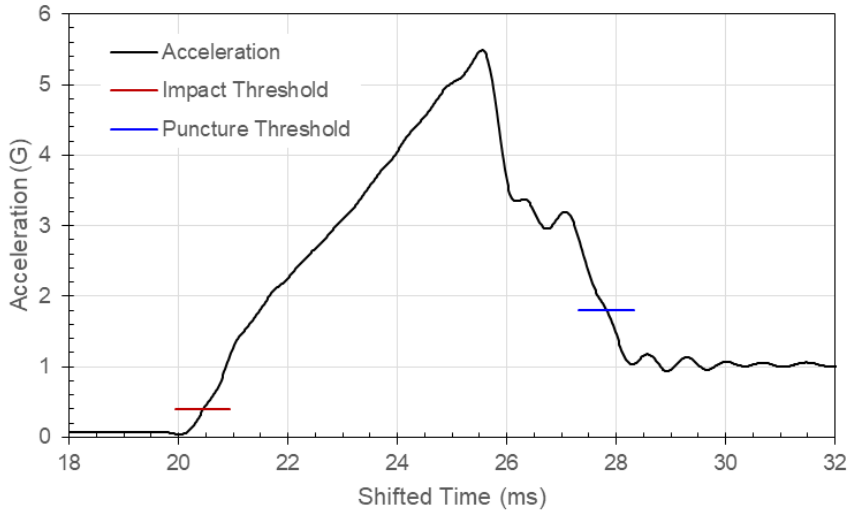

Figure 45: Carriage Acceleration in Test 40 with Specimen T063-08 and 0.500-Inch Probe

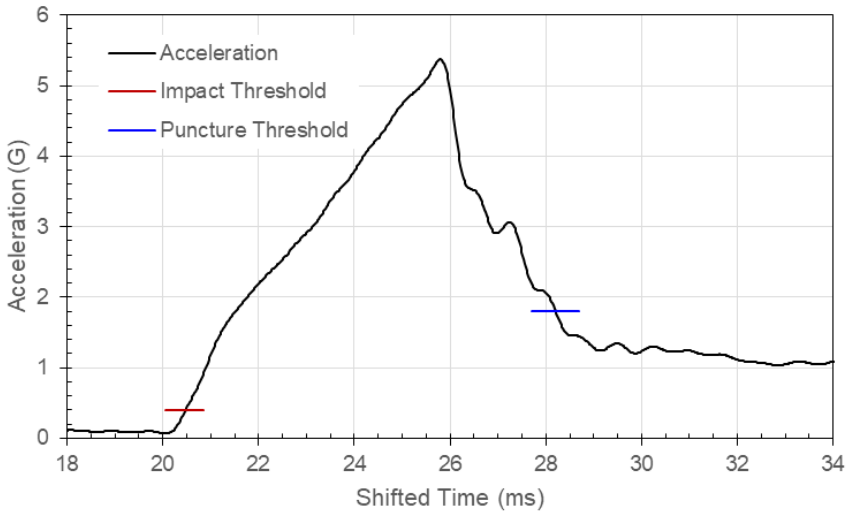

Figure 46: Carriage Acceleration in Test 41 with Specimen T063-09 and 0.500-Inch Probe

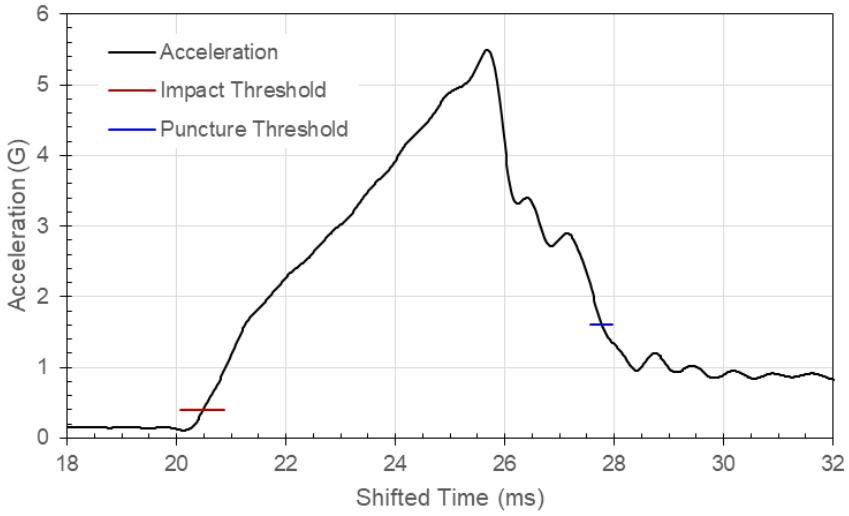

Figure 47: Carriage Acceleration in Test 42 with Specimen T063-10 and 0.500-Inch Probe

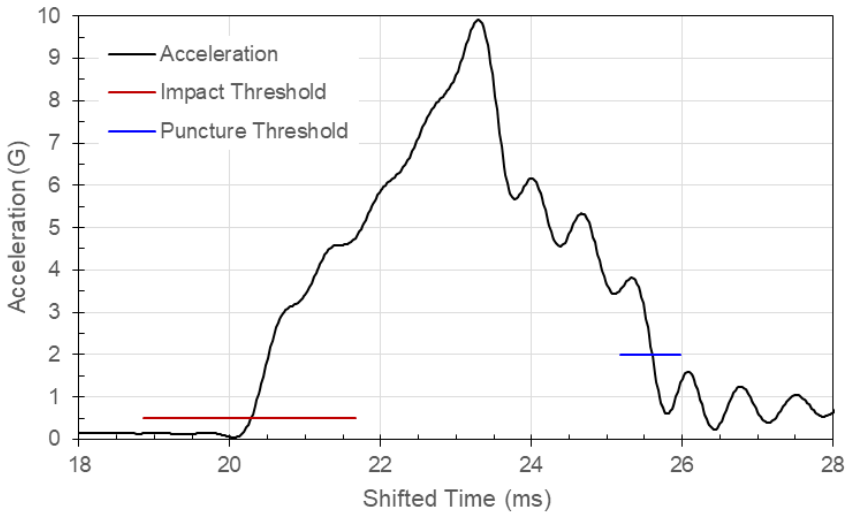

Figure 48: Carriage Acceleration in Test 43 with Specimen T063-11 and 1.000-Inch Probe

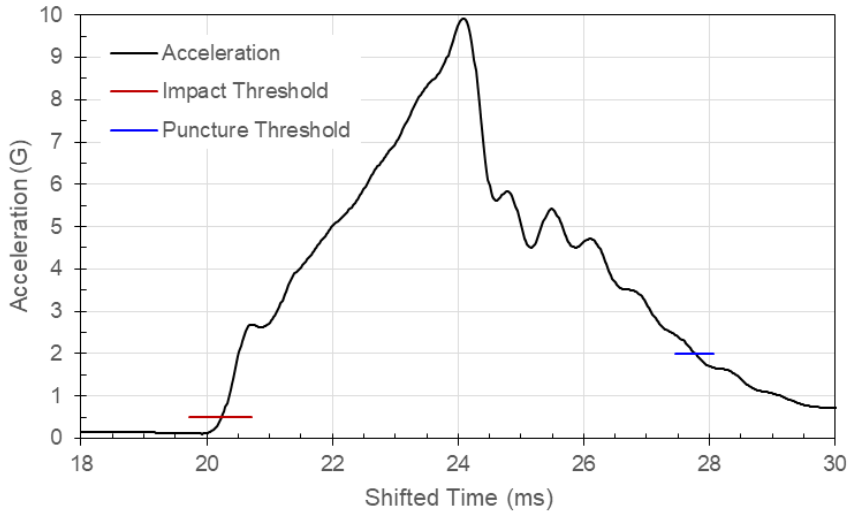

Figure 49: Carriage Acceleration in Test 44 with Specimen T063-12 and 1.000-Inch Probe

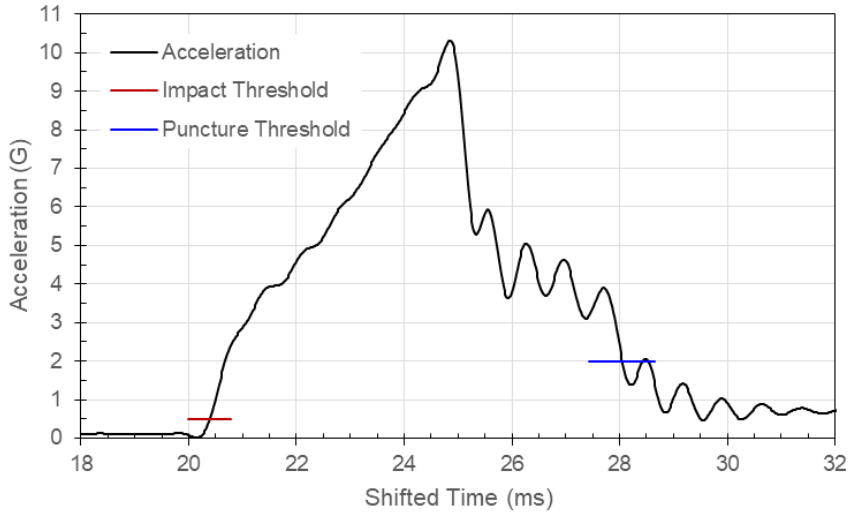

Figure 50: Carriage Acceleration in Test 45 with Specimen T063-13 and 1.000-Inch Probe

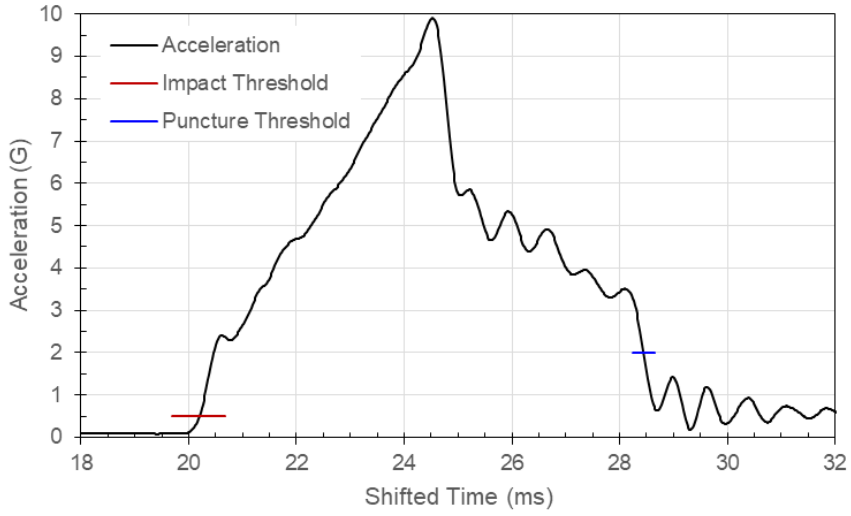

Figure 51: Carriage Acceleration in Test 46 with Specimen T063-14 and 1.000-Inch Probe

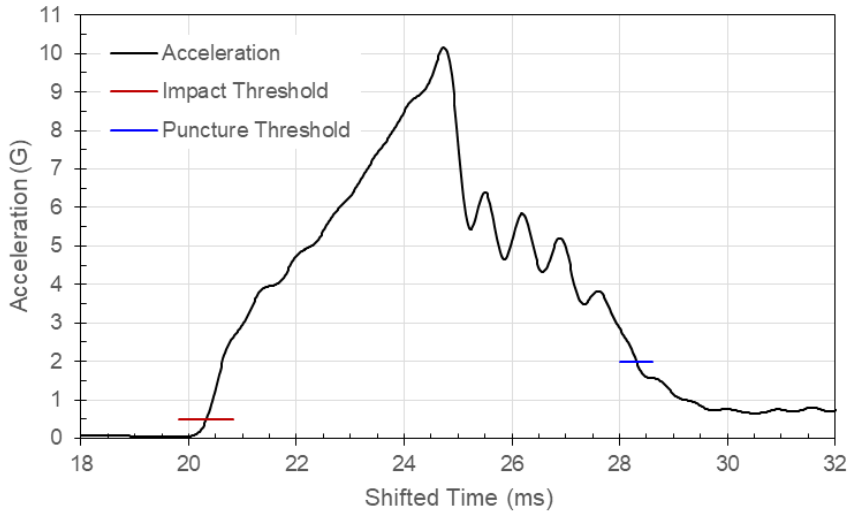

Figure 52: Carriage Acceleration in Test 47 with Specimen T063-15 and 1.000-Inch Probe

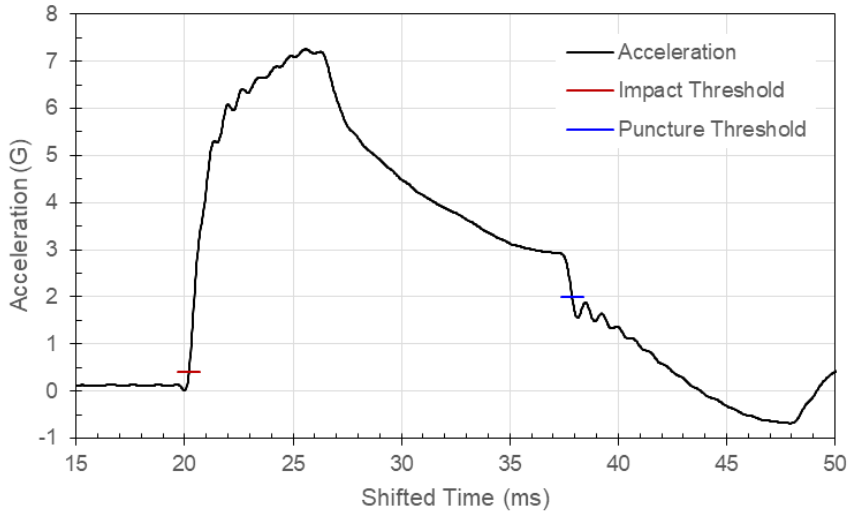

Figure 53: Carriage Acceleration in Test 49 with Specimen T125-02 and 0.250-Inch Probe

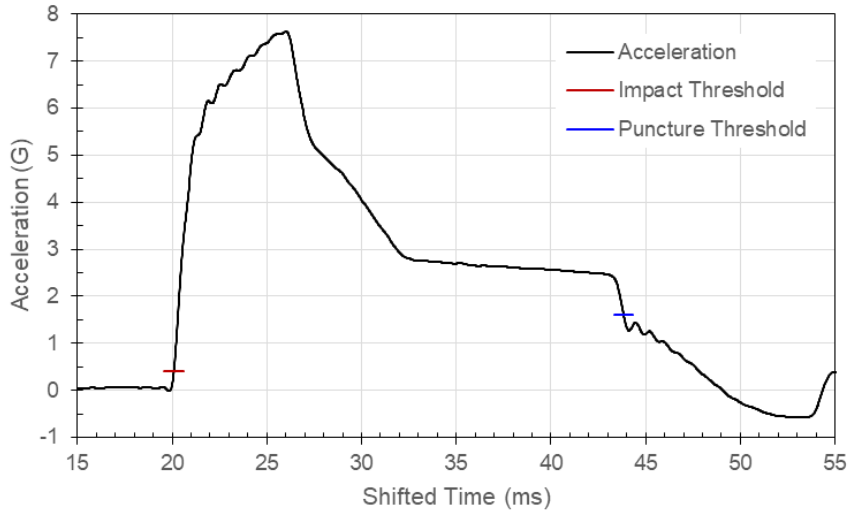

Figure 54: Carriage Acceleration in Test 50 with Specimen T125-03 and 0.250-Inch Probe

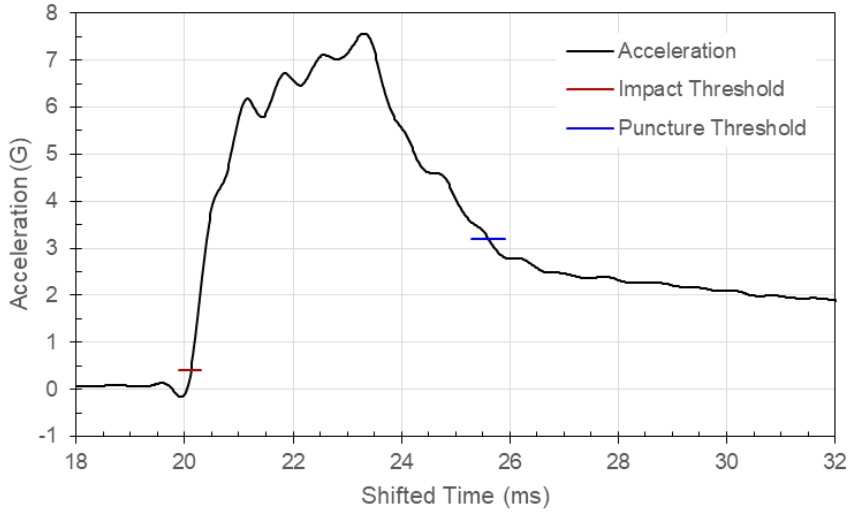

Figure 55: Carriage Acceleration in Test 51 with Specimen T125-04 and 0.250-Inch Probe

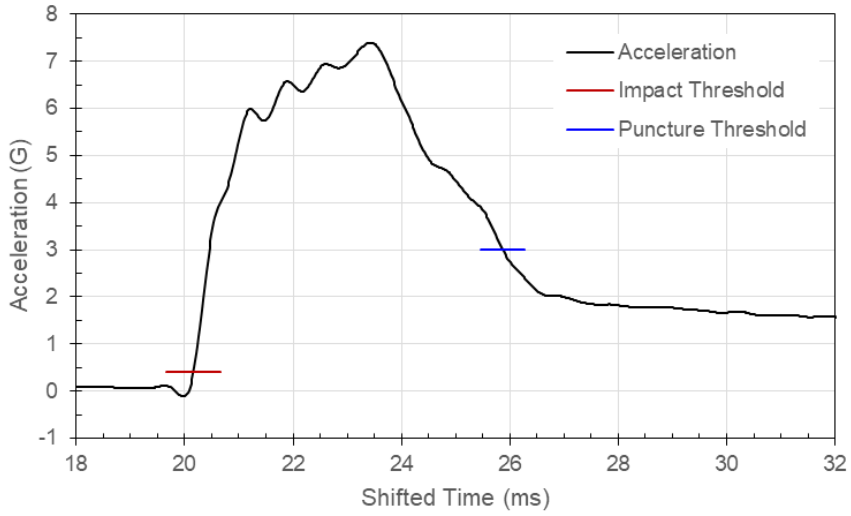

Figure 56: Carriage Acceleration in Test 52 with Specimen T125-05 and 0.250-Inch Probe

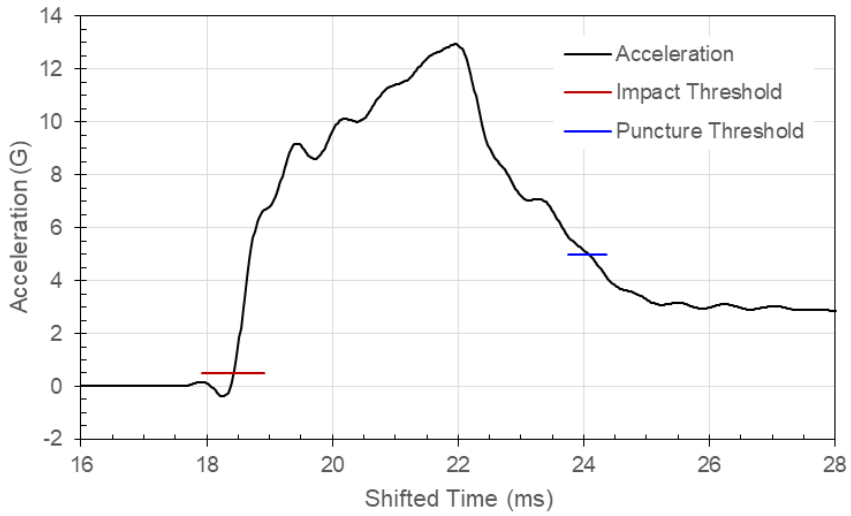

Figure 57: Carriage Acceleration in Test 59 with Specimen T125-07 and 0.500-Inch Probe

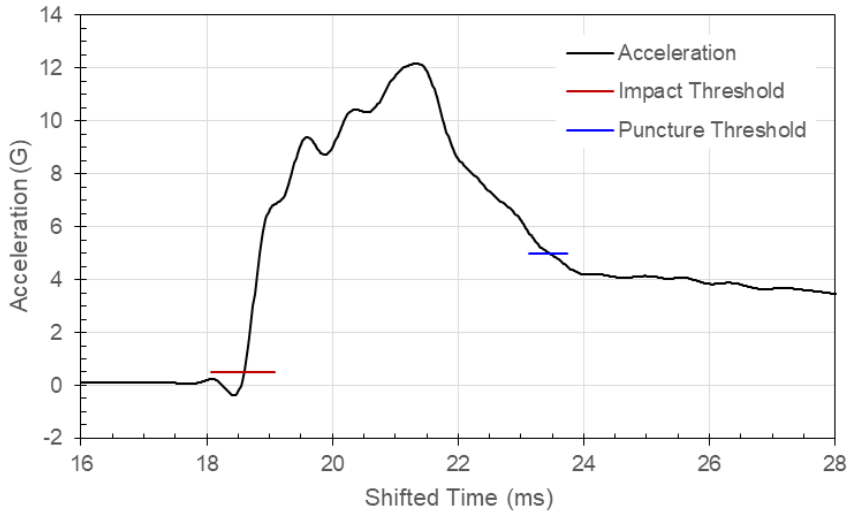

Figure 58: Carriage Acceleration in Test 60 with Specimen T125-08 and 0.500-Inch Probe

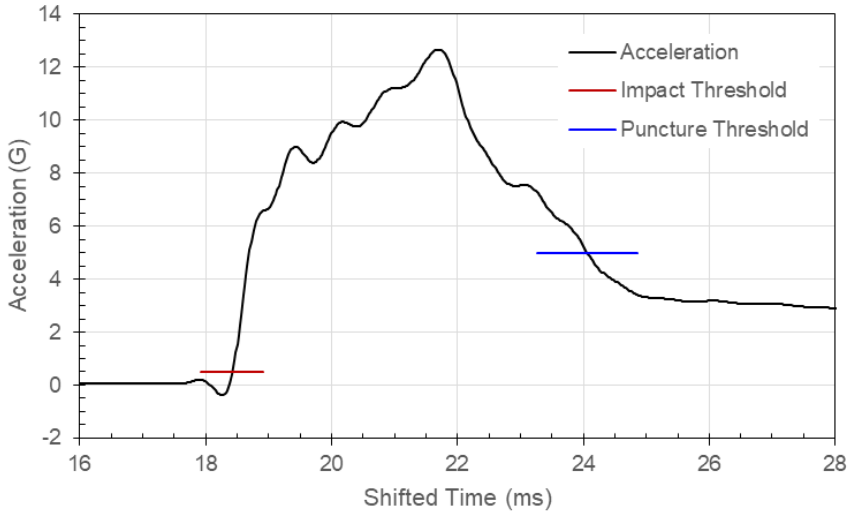

Figure 59: Carriage Acceleration in Test 61 with Specimen T125-09 and 0.500-Inch Probe

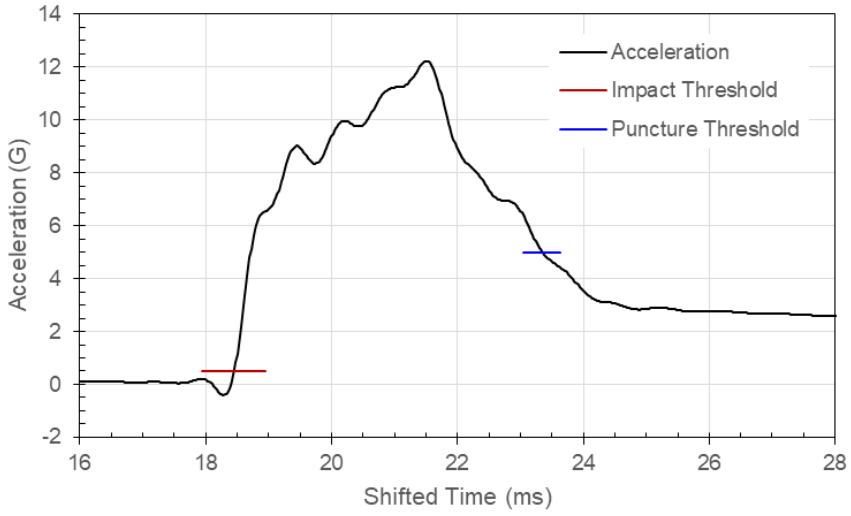

Figure 60: Carriage Acceleration in Test 62 with Specimen T125-10 and 0.500-Inch Probe

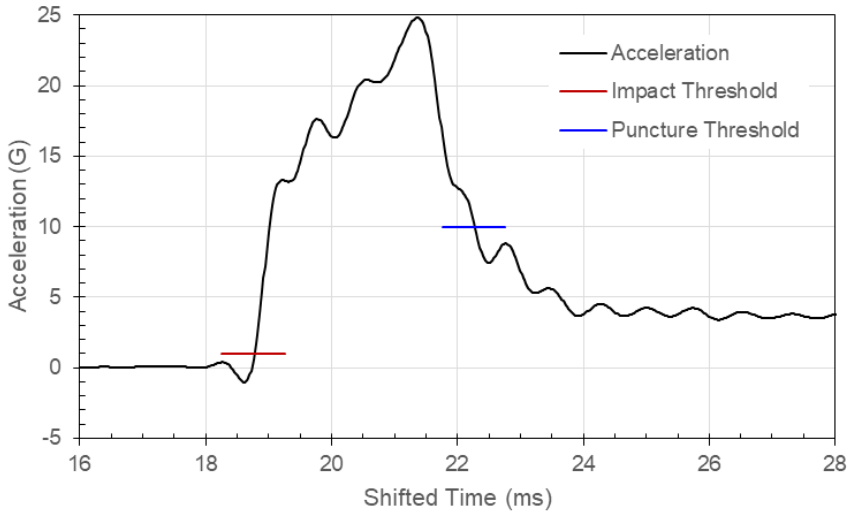

Figure 61: Carriage Acceleration in Test 64 with Specimen T125-11 and 1.000-Inch Probe

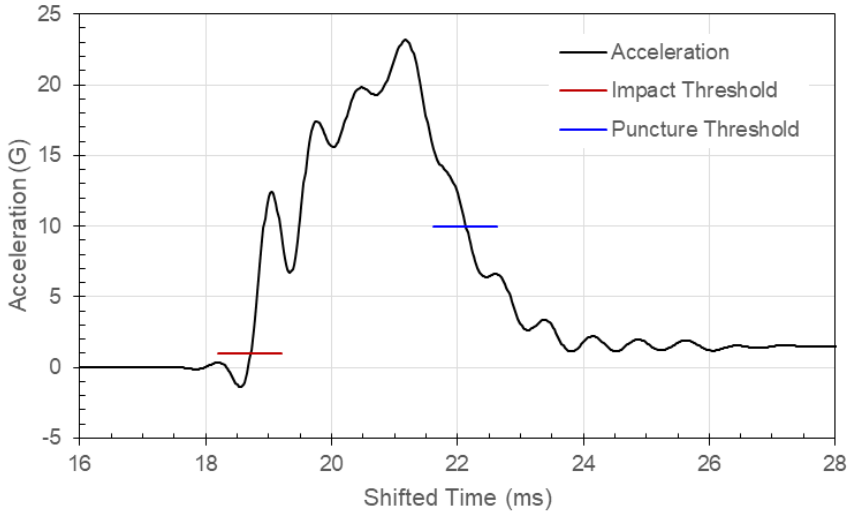

Figure 62: Carriage Acceleration in Test 65 with Specimen T125-12 and 1.000-Inch Probe

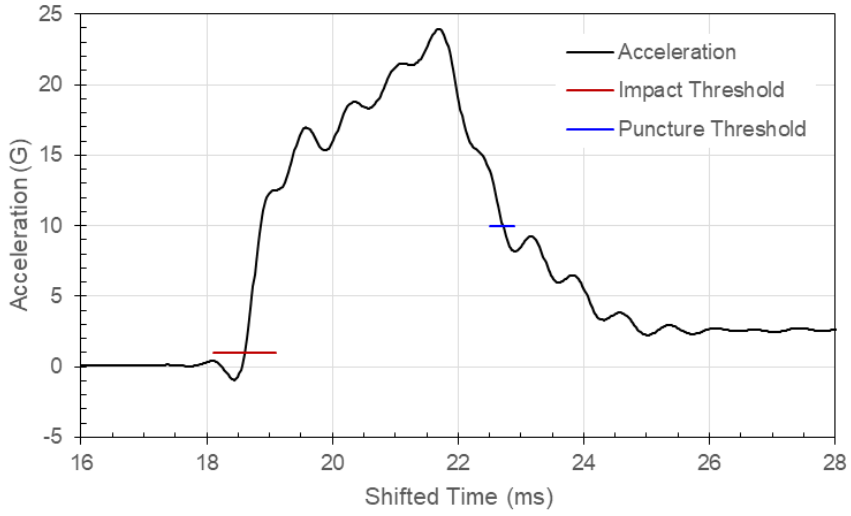

Figure 63: Carriage Acceleration in Test 66 with Specimen T125-13 and 1.000-Inch Probe

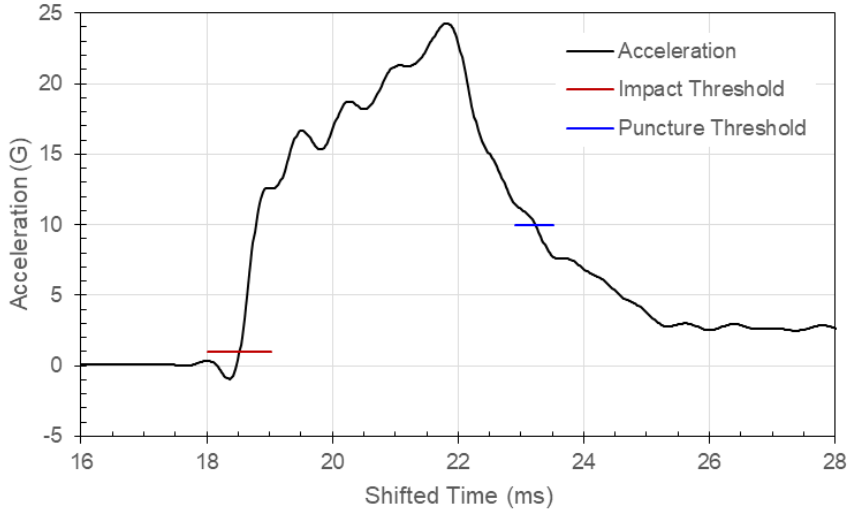

Figure 64: Carriage Acceleration in Test 67 with Specimen T125-14 and 1.000-Inch Probe

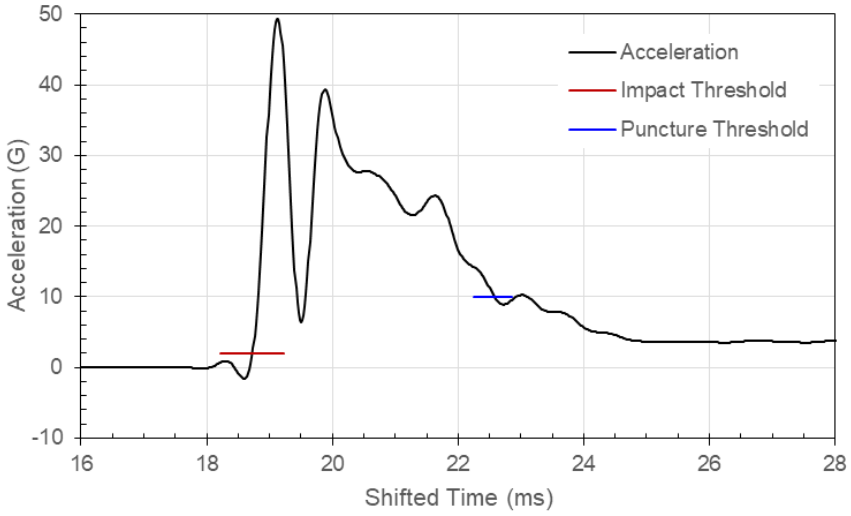

Figure 65: Carriage Acceleration in Test 68 with Specimen T125-15 and 1.000-Inch Probe

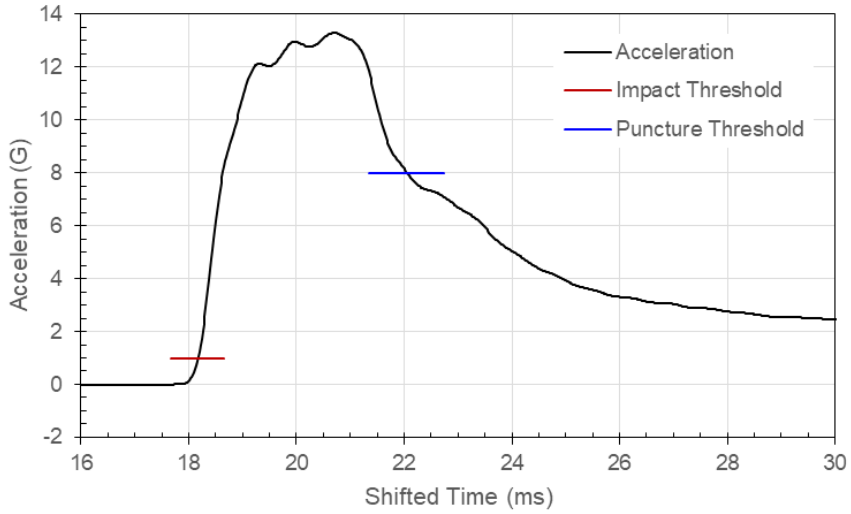

Figure 66: Carriage Acceleration in Test 73 with Specimen T188-01 and 0.250-Inch Probe

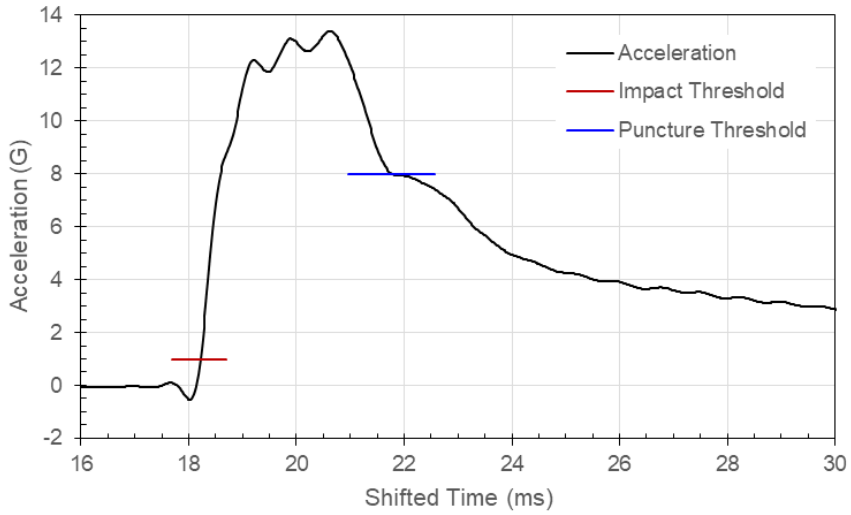

Figure 67: Carriage Acceleration in Test 74 with Specimen T188-02 and 0.250-Inch Probe

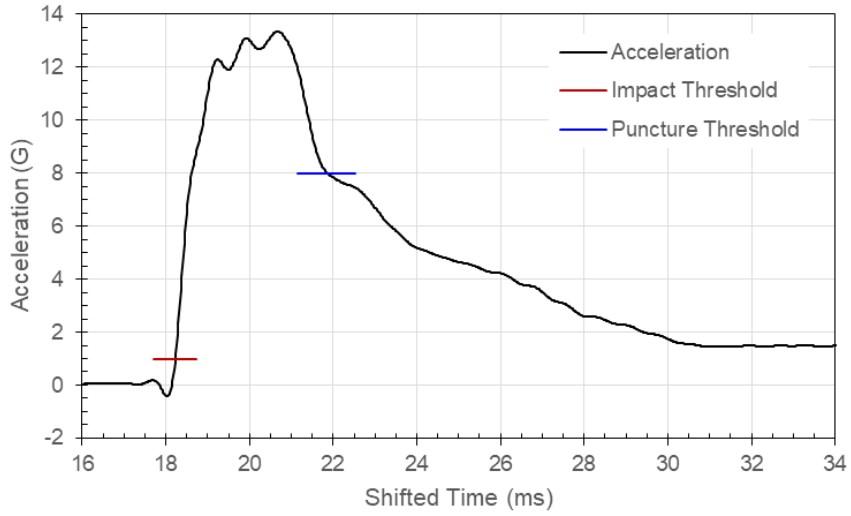

Figure 68: Carriage Acceleration in Test 75 with Specimen T188-03 and 0.250-Inch Probe

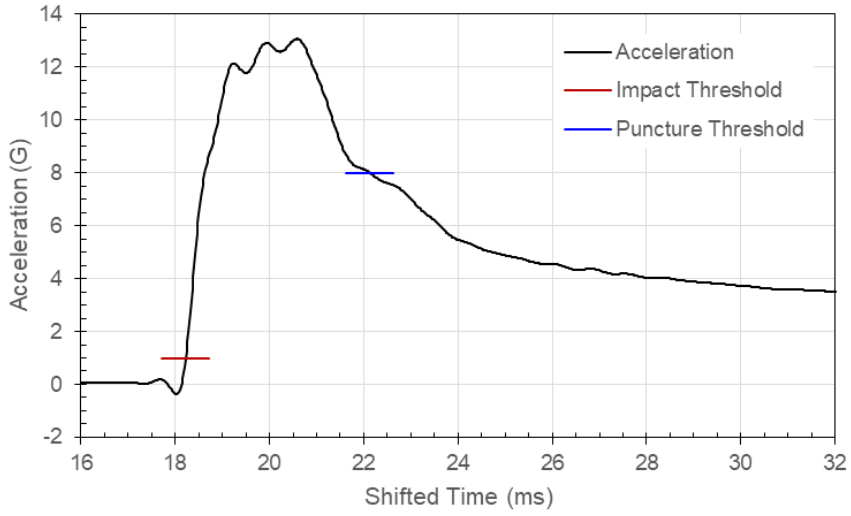

Figure 69: Carriage Acceleration in Test 76 with Specimen T188-04 and 0.250-Inch Probe

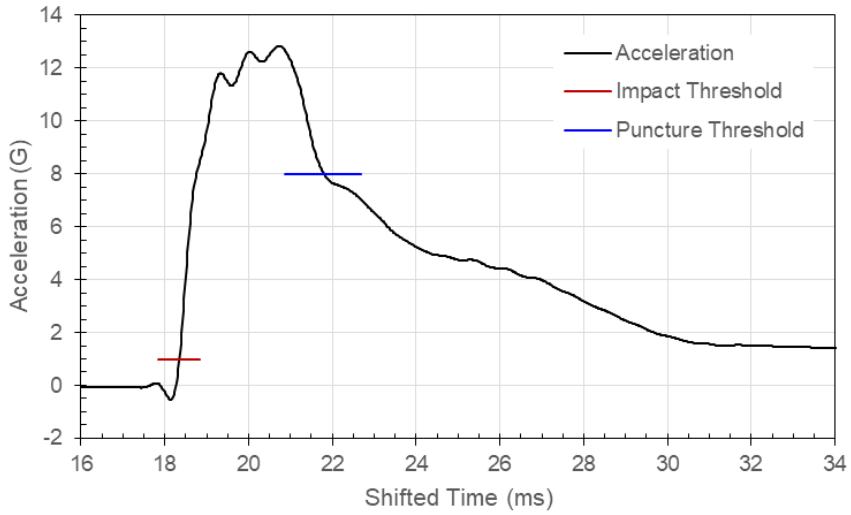

Figure 70: Carriage Acceleration in Test 77 with Specimen T188-05 and 0.250-Inch Probe

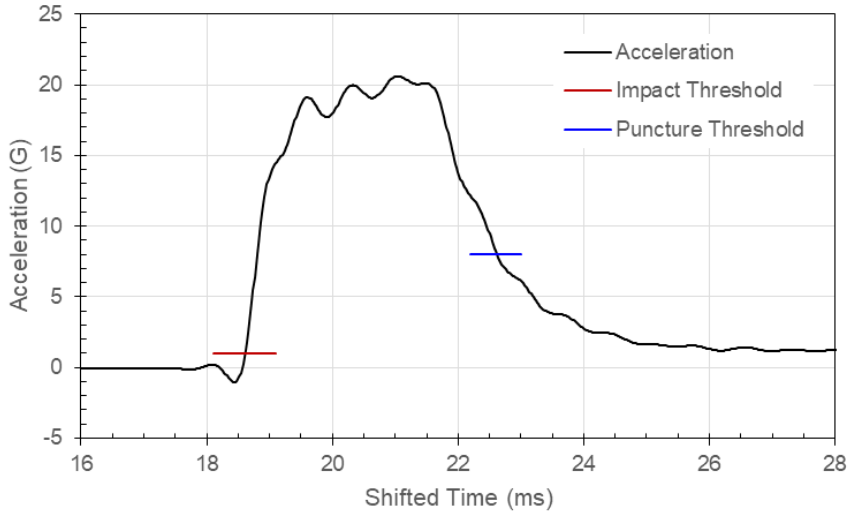

Figure 71: Carriage Acceleration in Test 78 with Specimen T188-06 and 0.500-Inch Probe

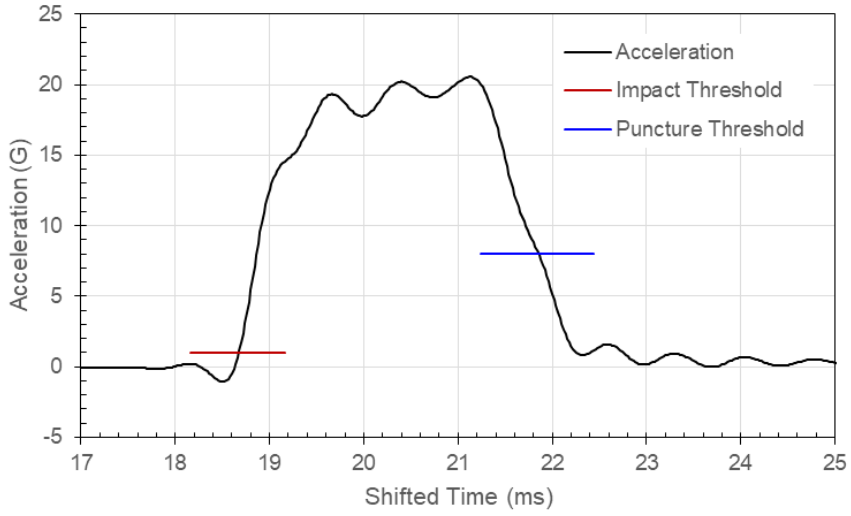

Figure 72: Carriage Acceleration in Test 79 with Specimen T188-07 and 0.500-Inch Probe

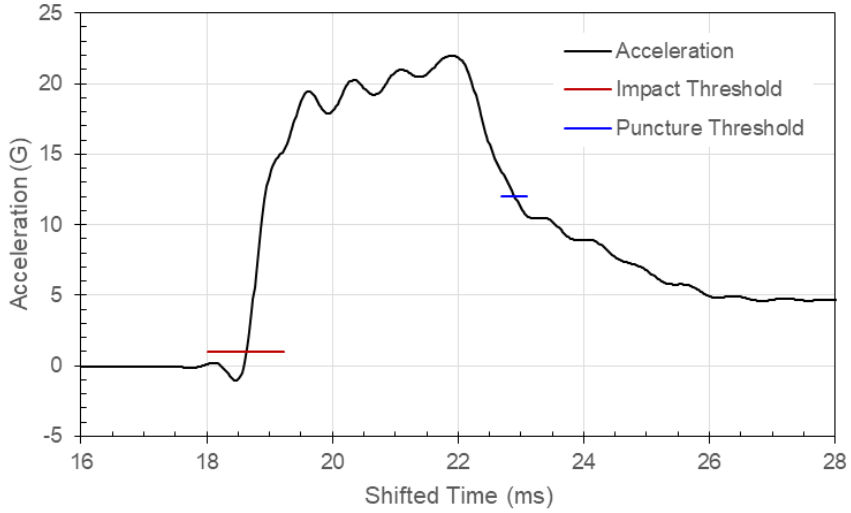

Figure 73: Carriage Acceleration in Test 80 with Specimen T188-08 and 0.500-Inch Probe

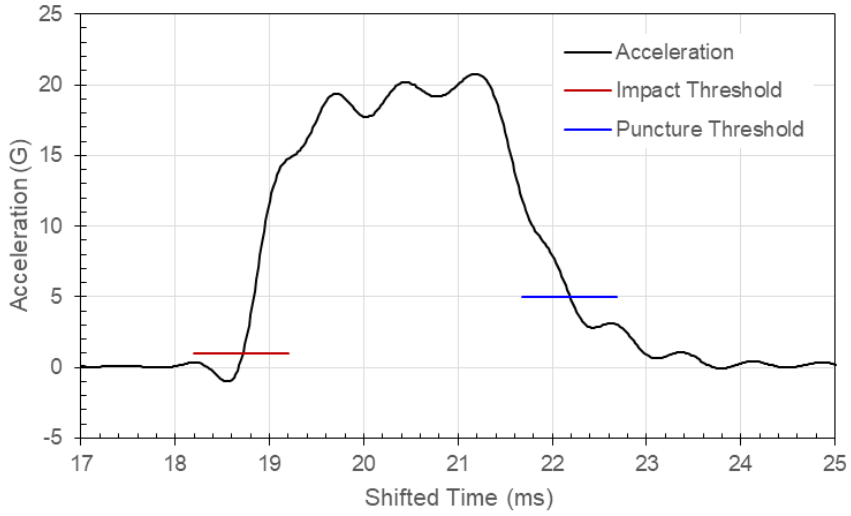

Figure 74: Carriage Acceleration in Test 81 with Specimen T188-09 and 0.500-Inch Probe

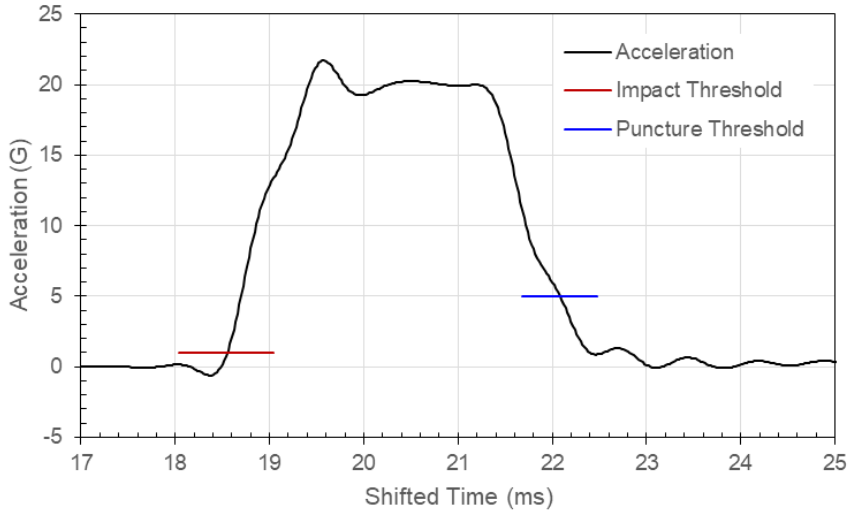

Figure 75: Carriage Acceleration in Test 82 with Specimen T188-10 and 0.500-Inch Probe

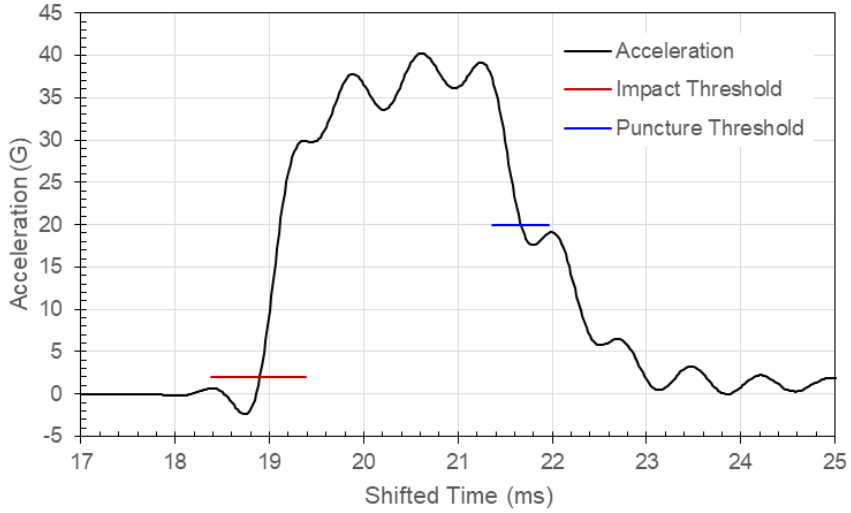

Figure 76: Carriage Acceleration in Test 83 with Specimen T188-11 and 1.000-Inch Probe

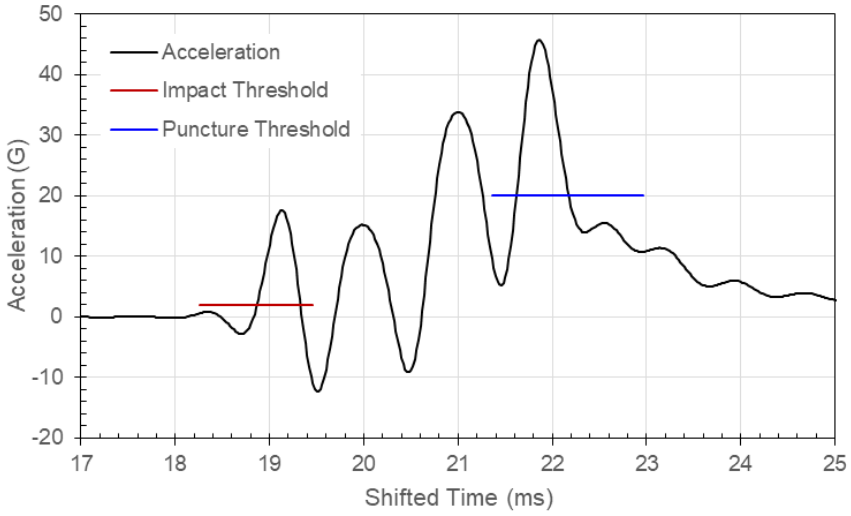

Figure 77: Carriage Acceleration in Test 84 with Specimen T188-12 and 1.000-Inch Probe

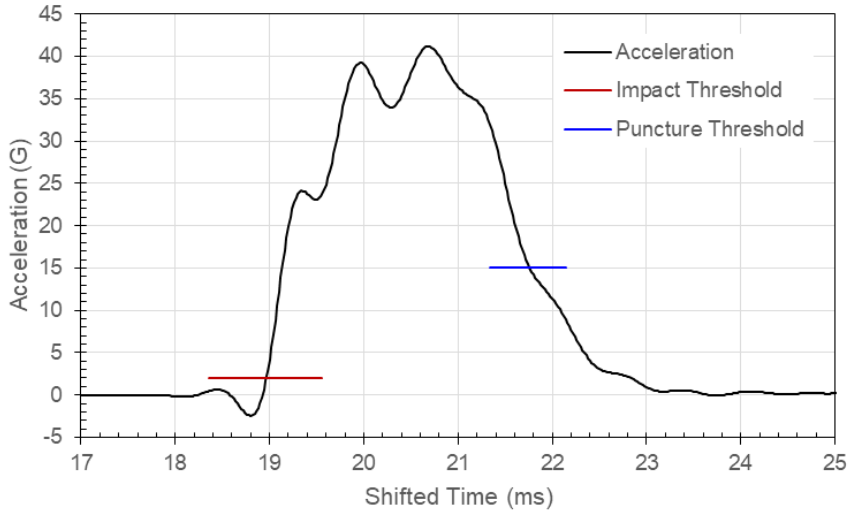

Figure 78: Carriage Acceleration in Test 85 with Specimen T188-13 and 1.000-Inch Probe

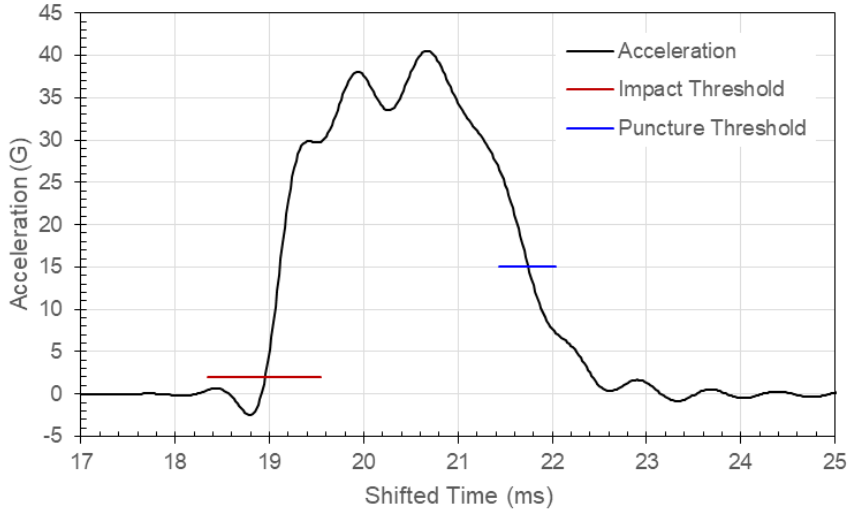

Figure 79: Carriage Acceleration in Test 86 with Specimen T188-14 and 1.000-Inch Probe

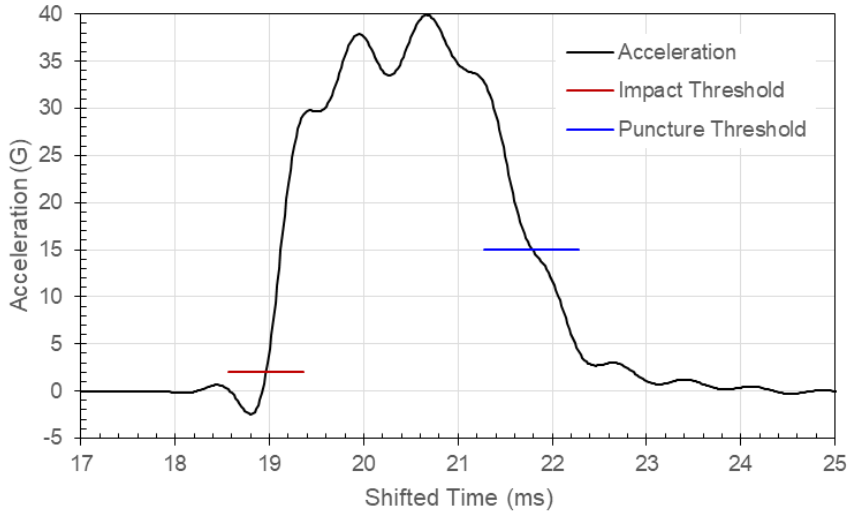

Figure 80: Carriage Acceleration in Test 87 with Specimen T188-15 and 1.000-Inch Probe

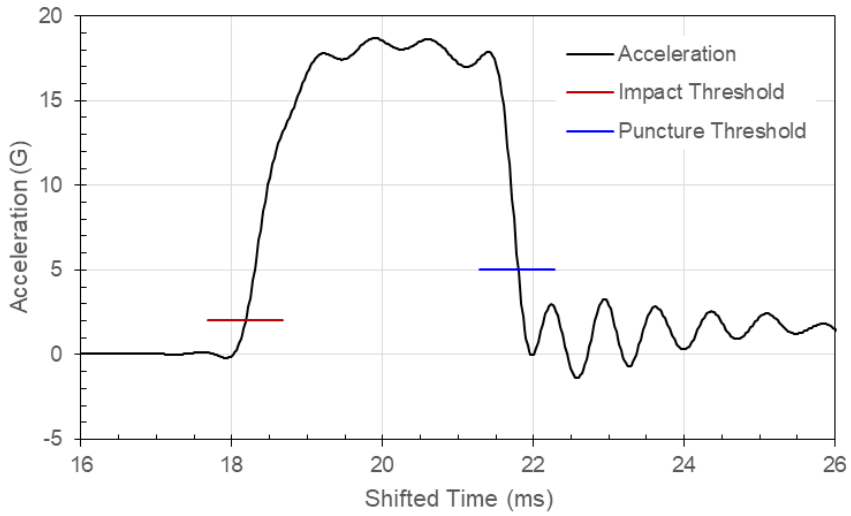

Figure 81: Carriage Acceleration in Test 88 with Specimen T250-01 and 0.250-Inch Probe

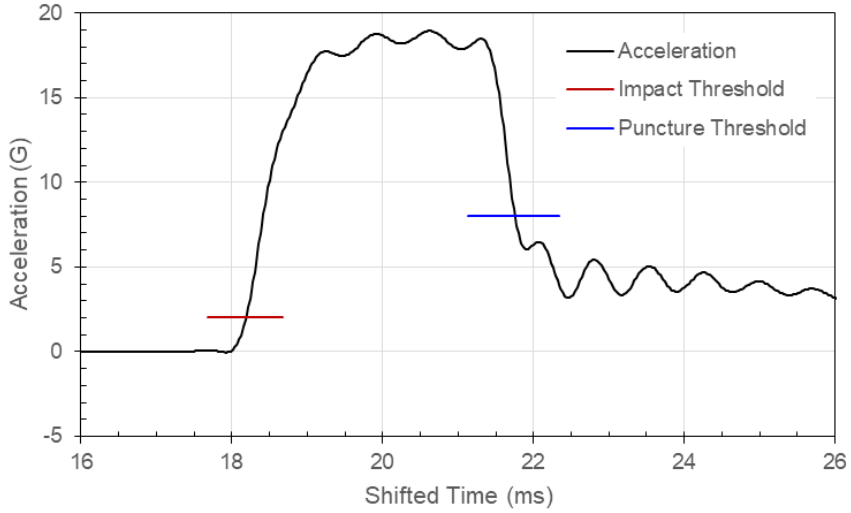

Figure 82: Carriage Acceleration in Test 89 with Specimen T250-02 and 0.250-Inch Probe

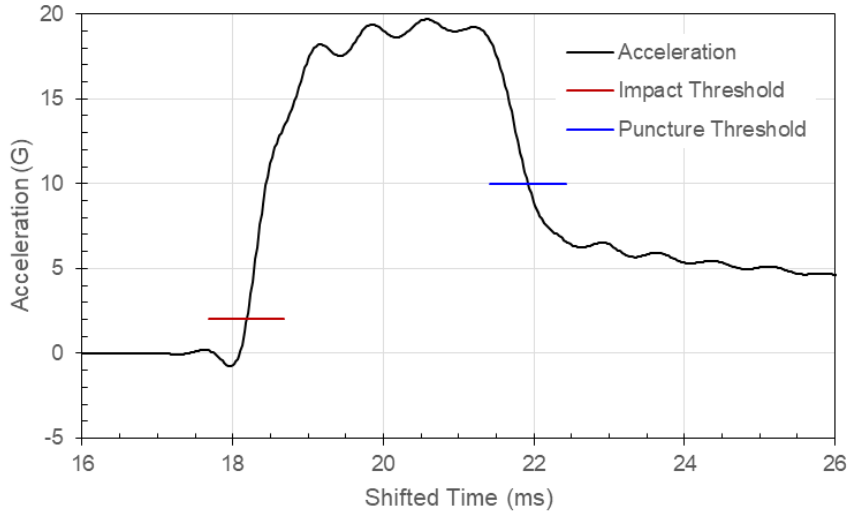

Figure 83: Carriage Acceleration in Test 90 with Specimen T250-03 and 0.250-Inch Probe

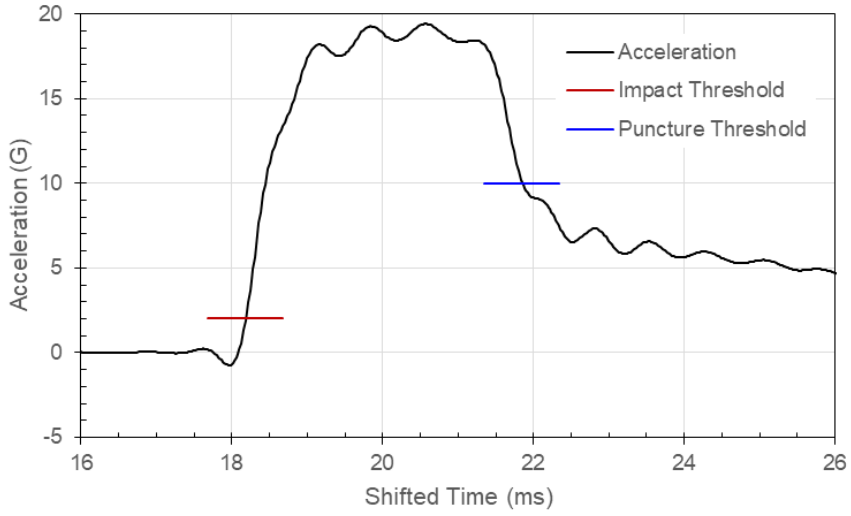

Figure 84: Carriage Acceleration in Test 91 with Specimen T250-04 and 0.250-Inch Probe

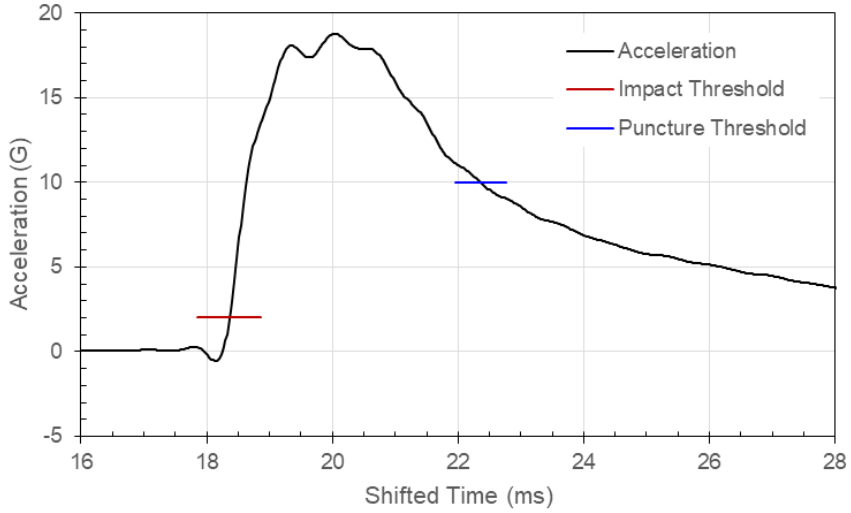

Figure 85: Carriage Acceleration in Test 92 with Specimen T250-05 and 0.250-Inch Probe

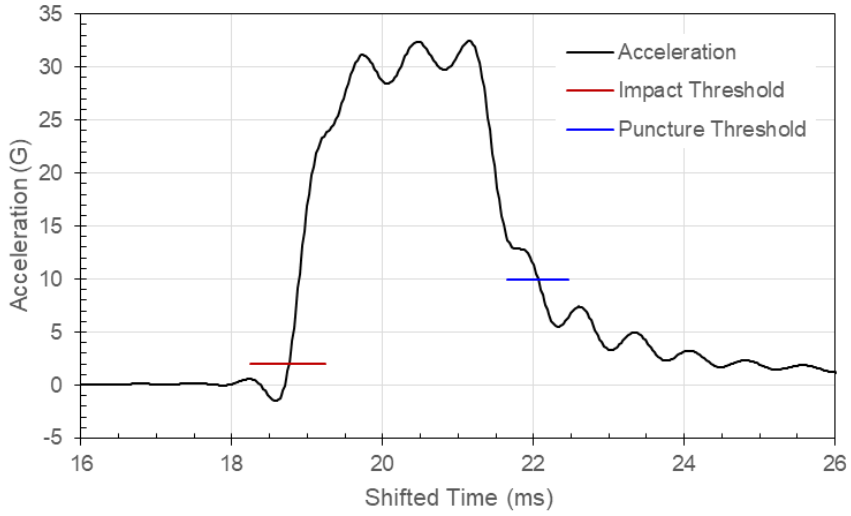

Figure 86: Carriage Acceleration in Test 94 with Specimen T250-07 and 0.500-Inch Probe

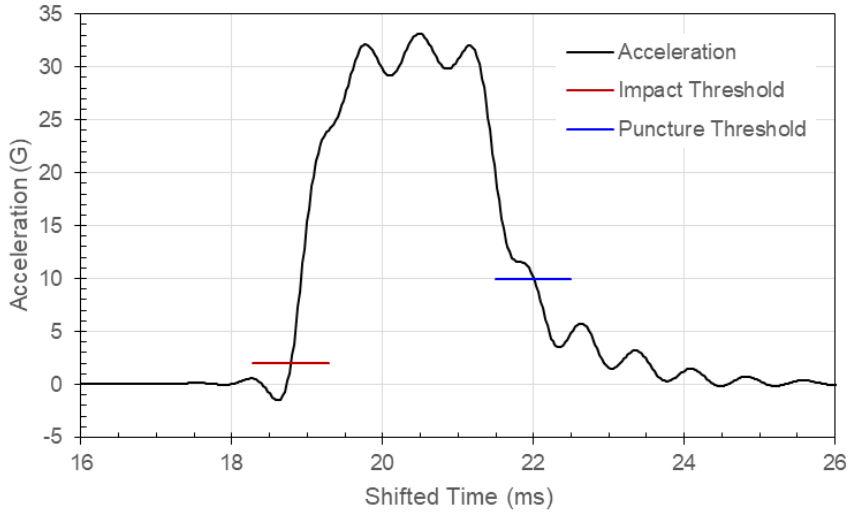

Figure 87: Carriage Acceleration in Test 95 with Specimen T250-08 and 0.500-Inch Probe

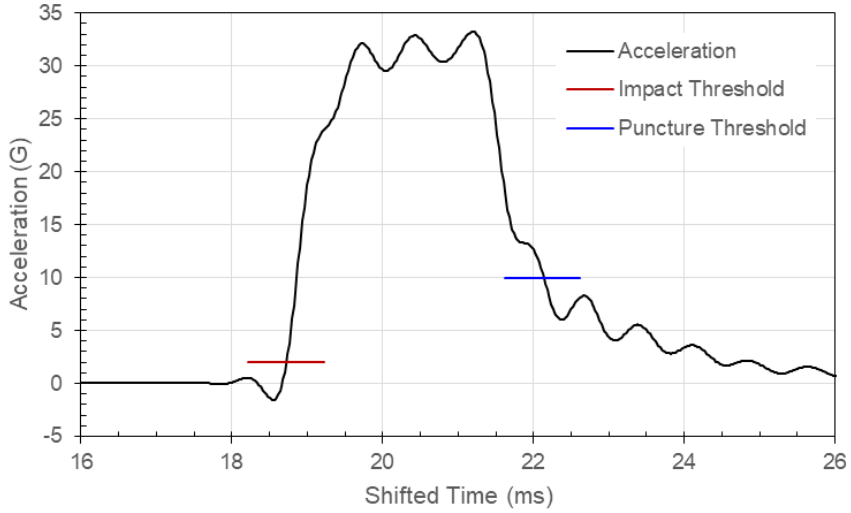

Figure 88: Carriage Acceleration in Test 96 with Specimen T250-09 and 0.500-Inch Probe

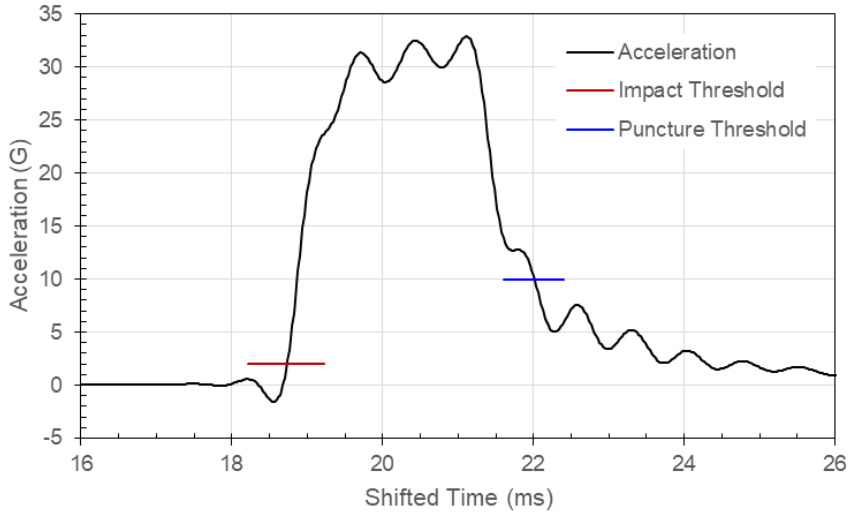

Figure 89: Carriage Acceleration in Test 97 with Specimen T250-10 and 0.500-Inch Probe

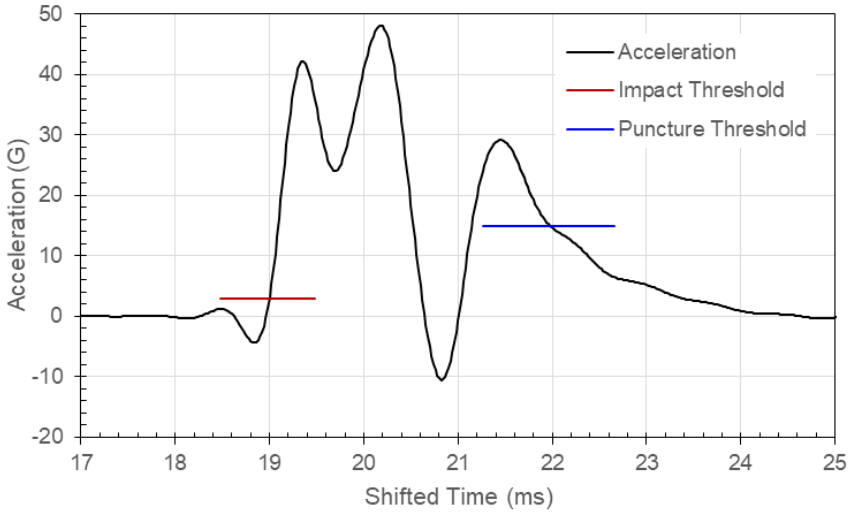

Figure 90: Carriage Acceleration in Test 98 with Specimen T250-11 and 1.000-Inch Probe

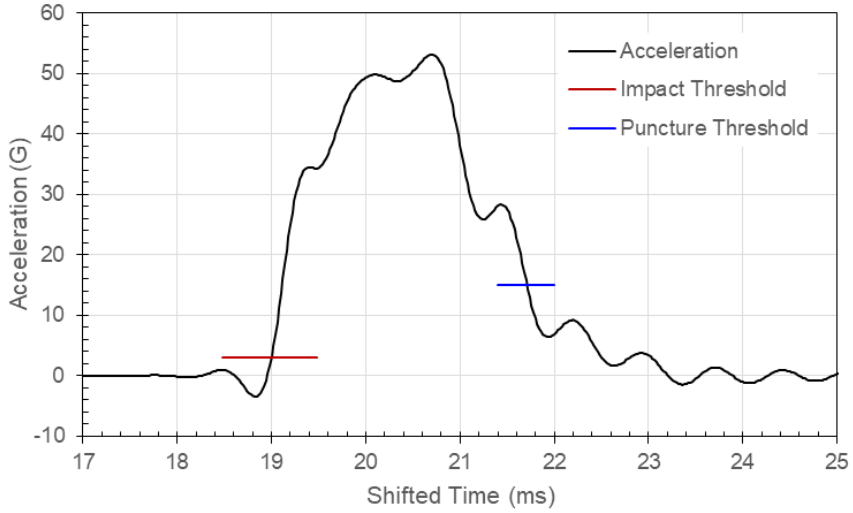

Figure 91: Carriage Acceleration in Test 99 with Specimen T250-12 and 1.000-Inch Probe

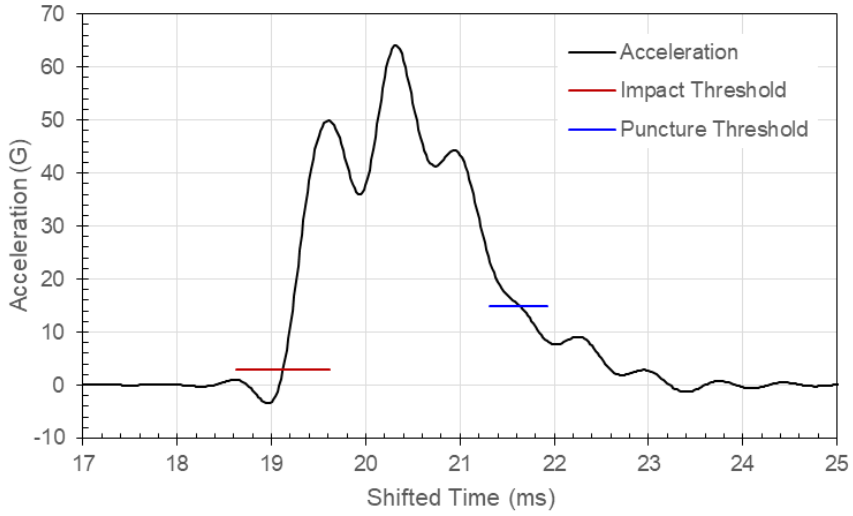

Figure 92: Carriage Acceleration in Test 100 with Specimen T250-13 and 1.000-Inch Probe

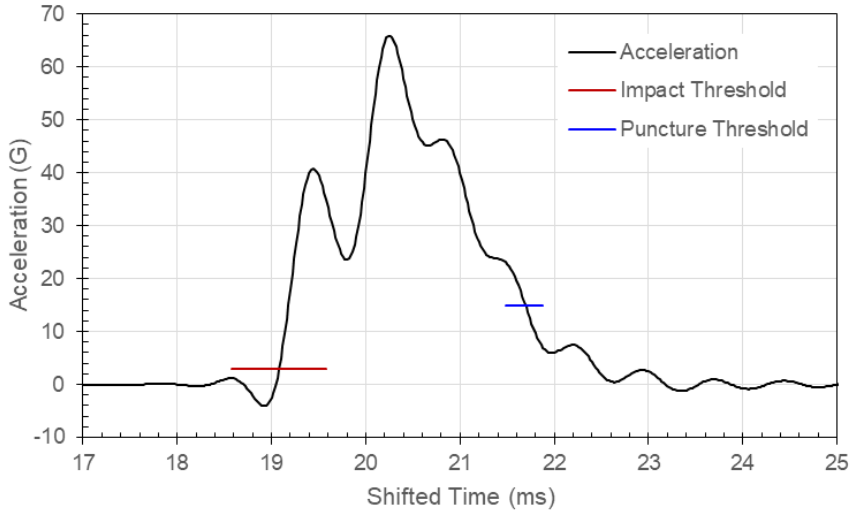

Figure 93: Carriage Acceleration in Test 101 with Specimen T250-14 and 1.000-Inch Probe

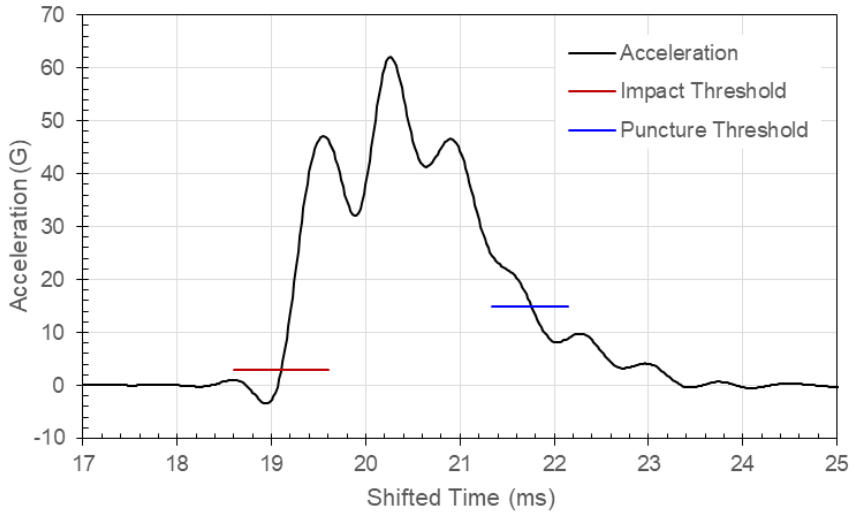

Figure 94: Carriage Acceleration in Test 102 with Specimen T250-15 and 1.000-Inch Probe

Appendix B: Total Energy

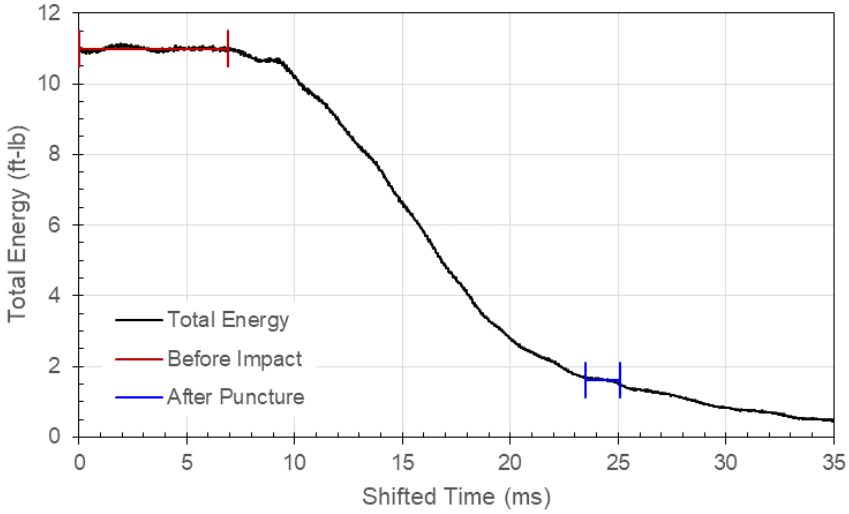

Figure 95: Carriage Total Energy in Test 35 with Specimen T063-02 and 0.250-Inch Probe

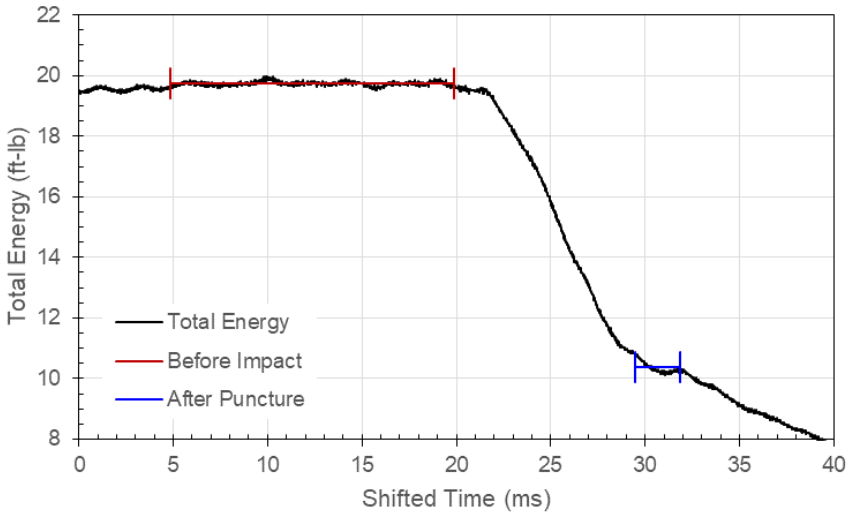

Figure 96: Carriage Total Energy in Test 36 with Specimen T063-04 and 0.250-Inch Probe

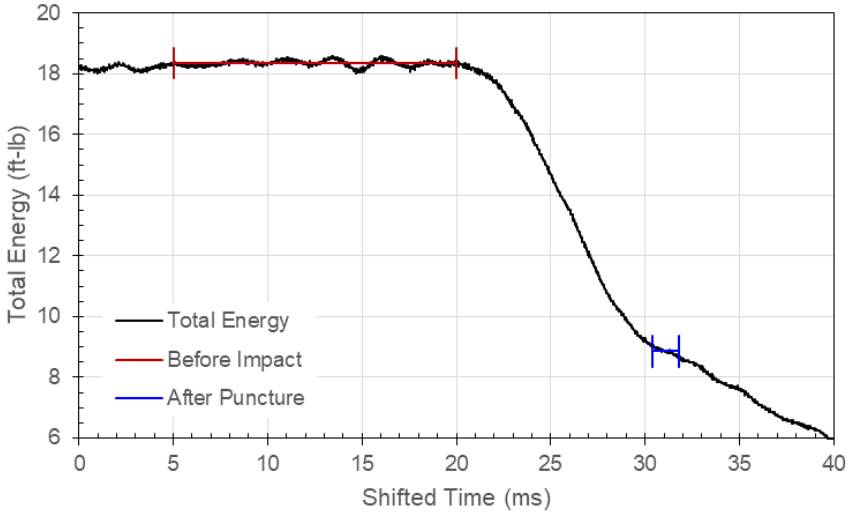

Figure 97: Carriage Total Energy in Test 37 with Specimen T063-05 and 0.250-Inch Probe

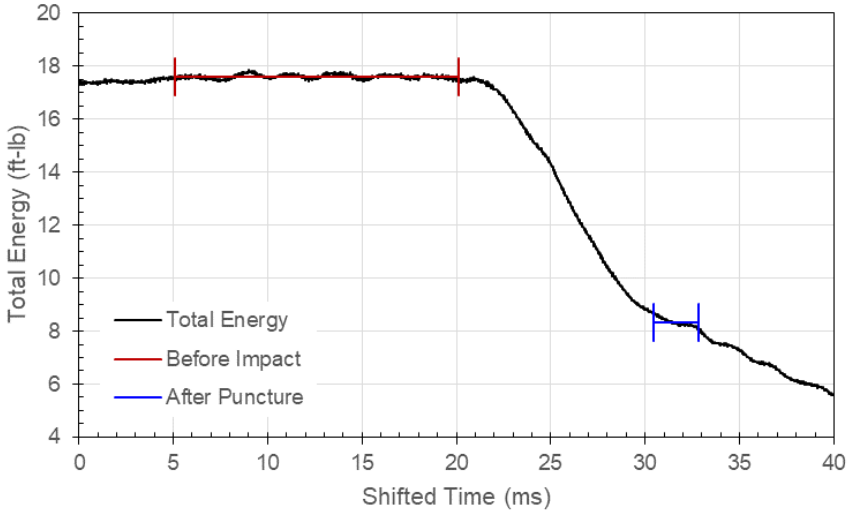

Figure 98: Carriage Total Energy in Test 38 with Specimen T063-06 and 0.250-Inch Probe

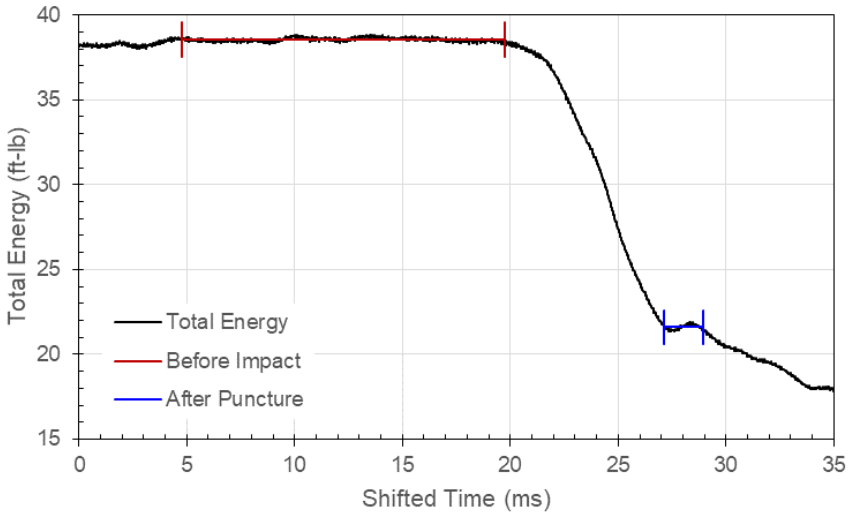

Figure 99: Carriage Total Energy in Test 39 with Specimen T063-07 and 0.500-Inch Probe

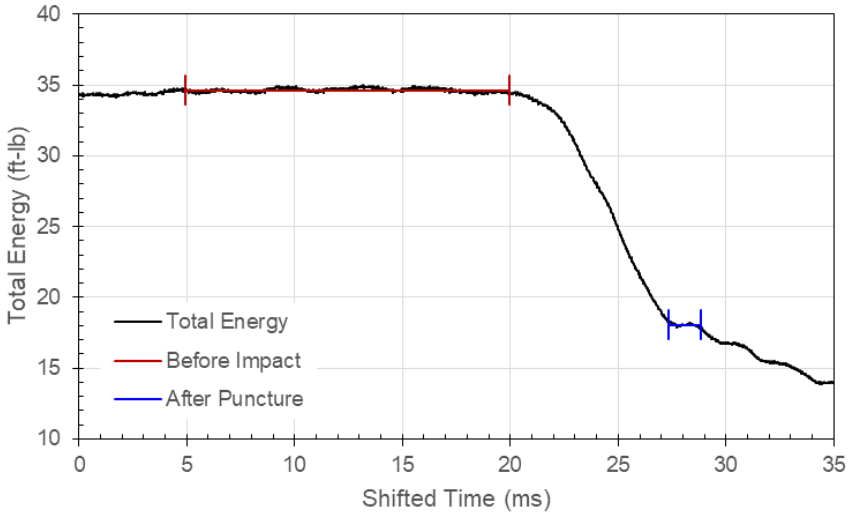

Figure 100: Carriage Total Energy in Test 40 with Specimen T063-08 and 0.500-Inch Probe

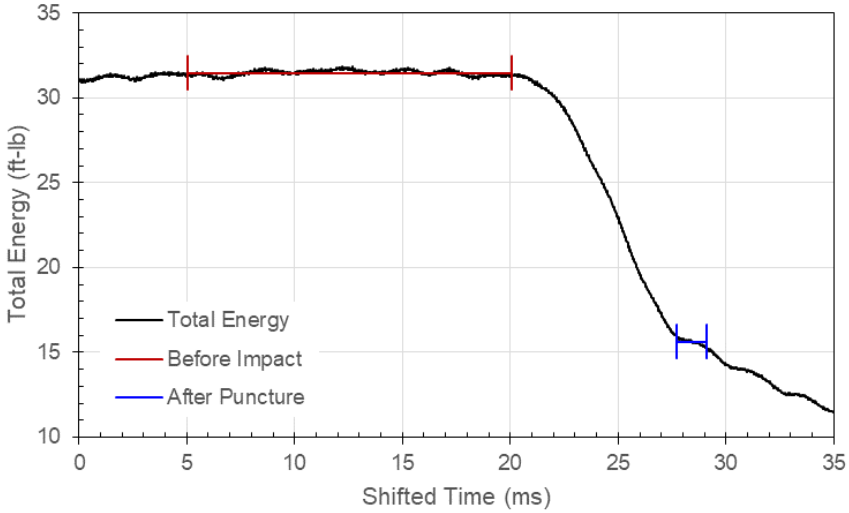

Figure 101: Carriage Total Energy in Test 41 with Specimen T063-09 and 0.500-Inch Probe

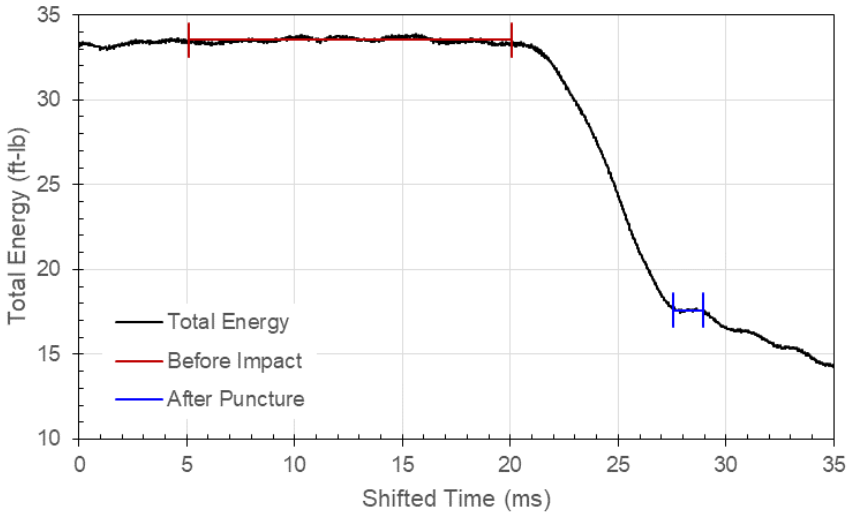

Figure 102: Carriage Total Energy in Test 42 with Specimen T063-10 and 0.500-Inch Probe

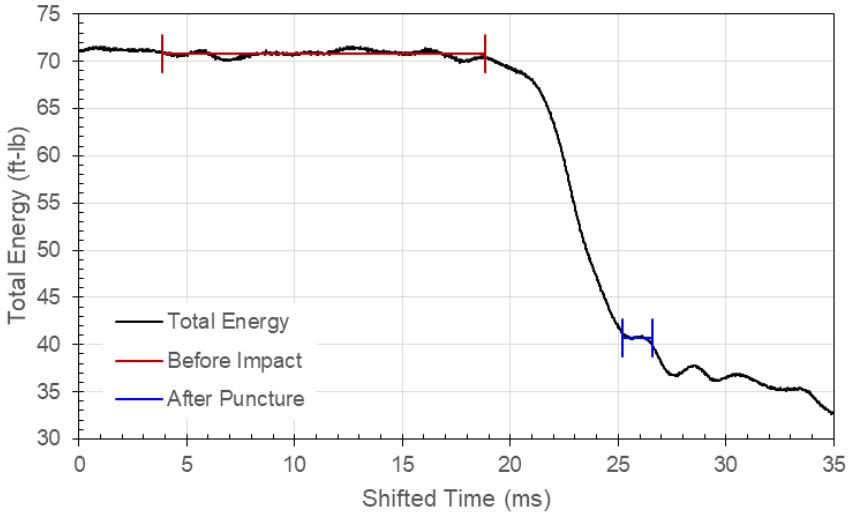

Figure 103: Carriage Total Energy in Test 43 with Specimen T063-11 and 1.000-Inch Probe

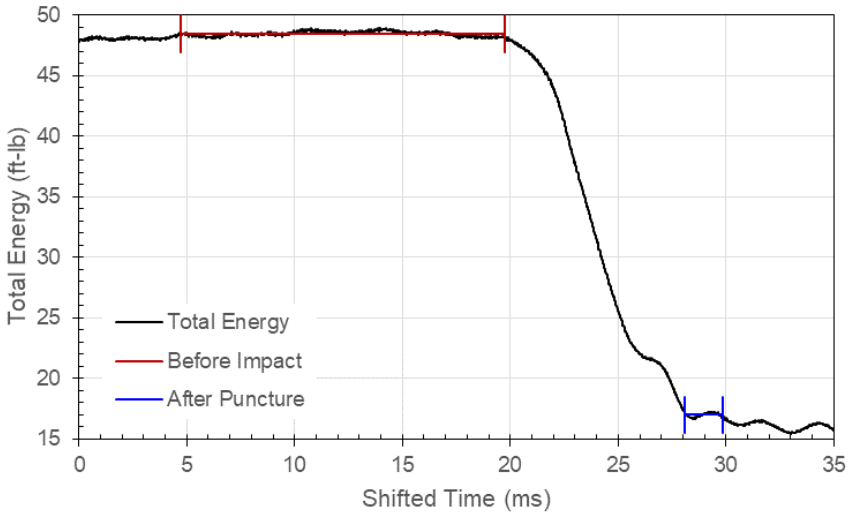

Figure 104: Carriage Total Energy in Test 44 with Specimen T063-12 and 1.000-Inch Probe

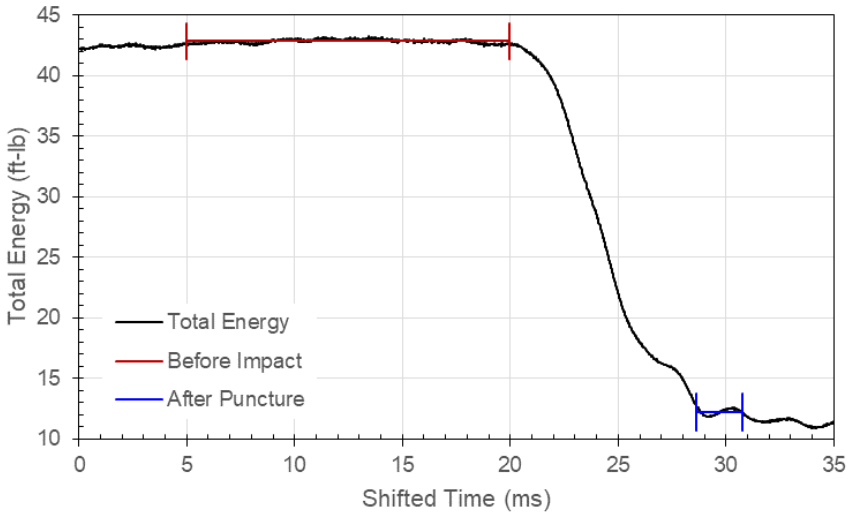

Figure 105: Carriage Total Energy in Test 45 with Specimen T063-13 and 1.000-Inch Probe

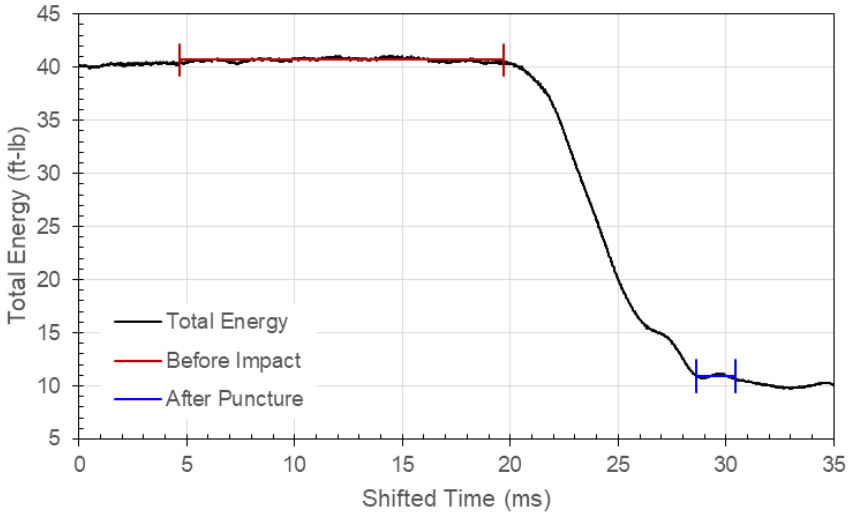

Figure 106: Carriage Total Energy in Test 46 with Specimen T063-14 and 1.000-Inch Probe

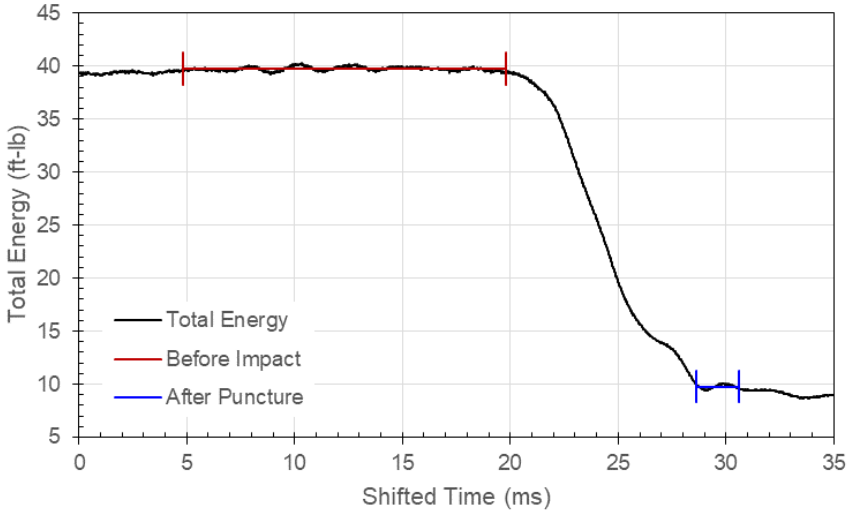

Figure 107: Carriage Total Energy in Test 47 with Specimen T063-15 and 1.000-Inch Probe

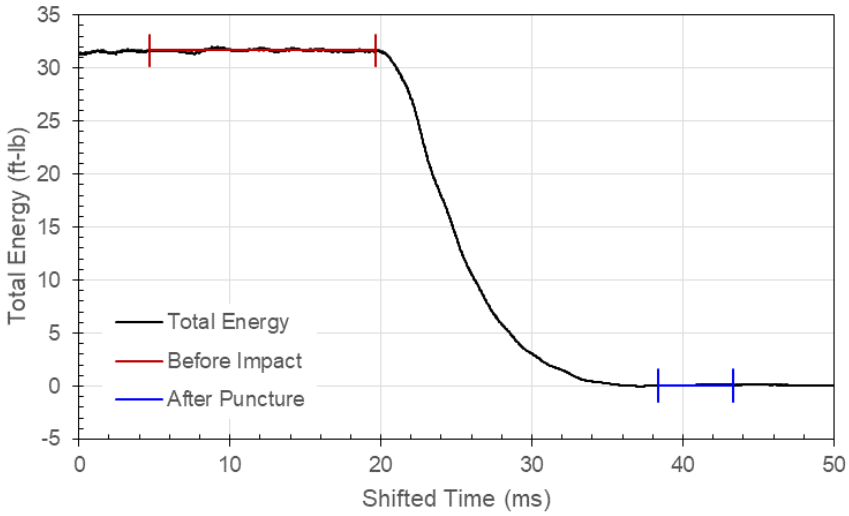

Figure 108: Carriage Total Energy in Test 49 with Specimen T125-02 and 0.250-Inch Probe

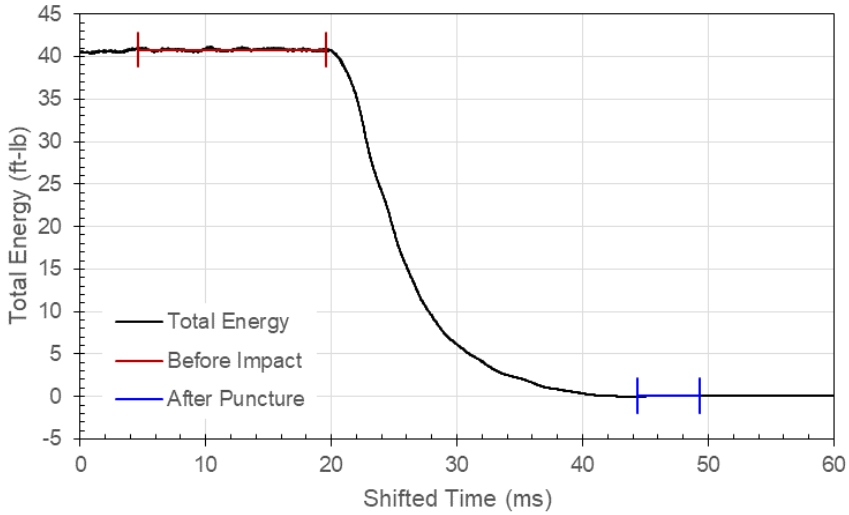

Figure 109: Carriage Total Energy in Test 50 with Specimen T125-03 and 0.250-Inch Probe

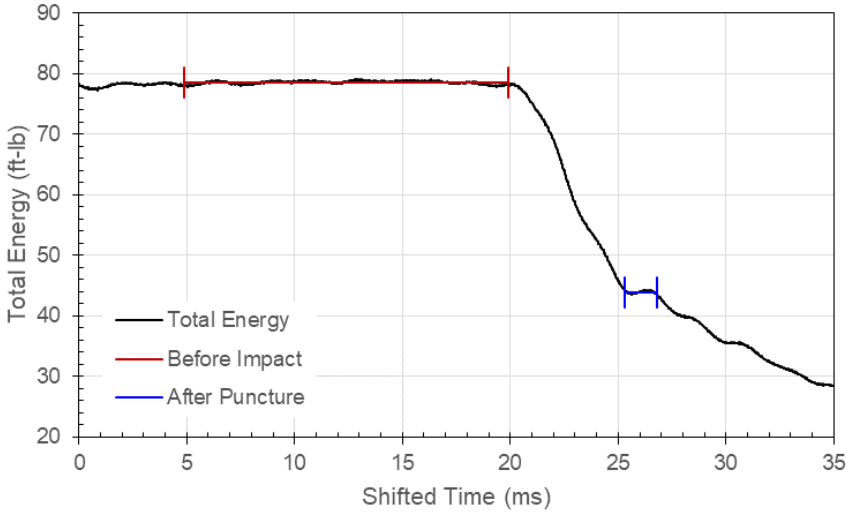

Figure 110: Carriage Total Energy in Test 51 with Specimen T125-04 and 0.250-Inch Probe

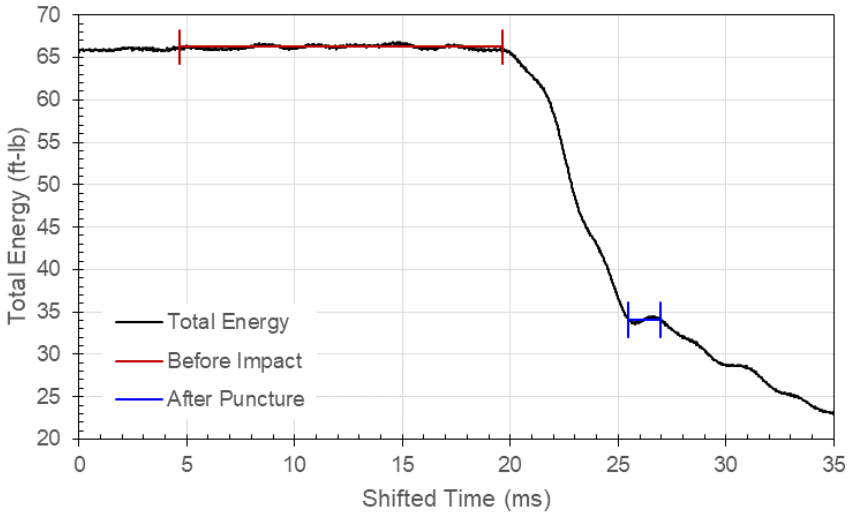

Figure 111: Carriage Total Energy in Test 52 with Specimen T125-05 and 0.250-Inch Probe

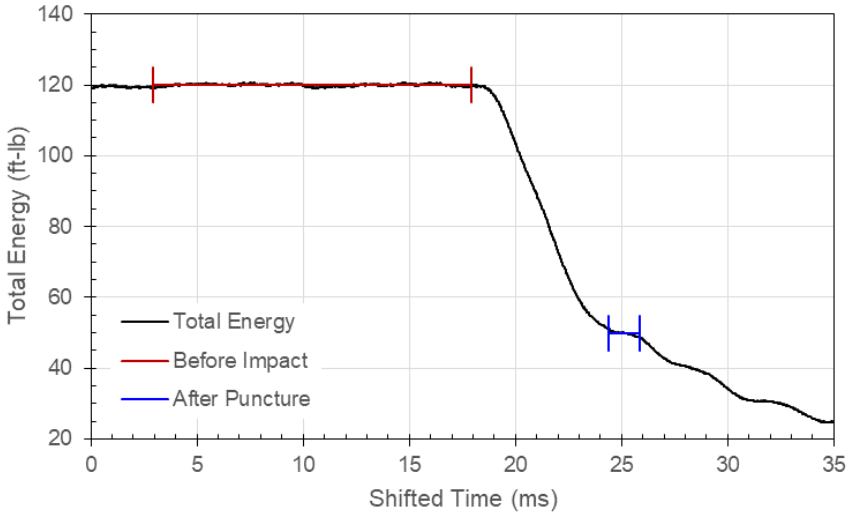

Figure 112: Carriage Total Energy in Test 59 with Specimen T125-07 and 0.500-Inch Probe

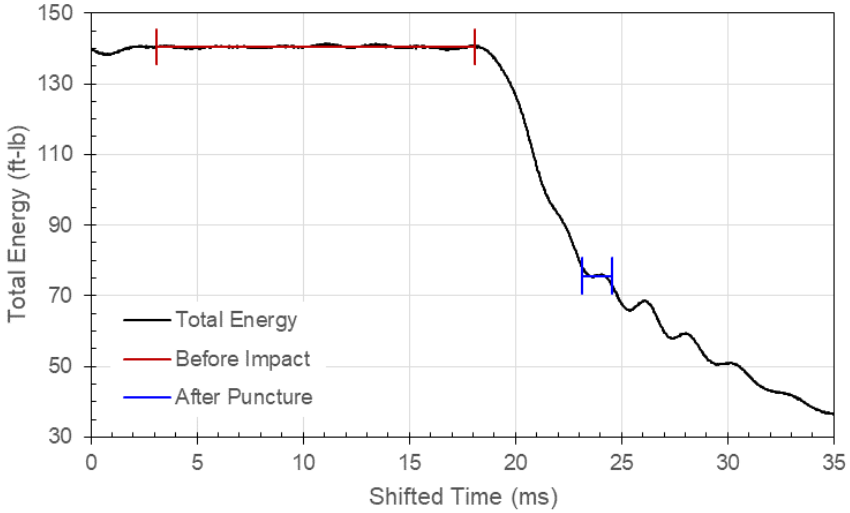

Figure 113: Carriage Total Energy in Test 60 with Specimen T125-08 and 0.500-Inch Probe

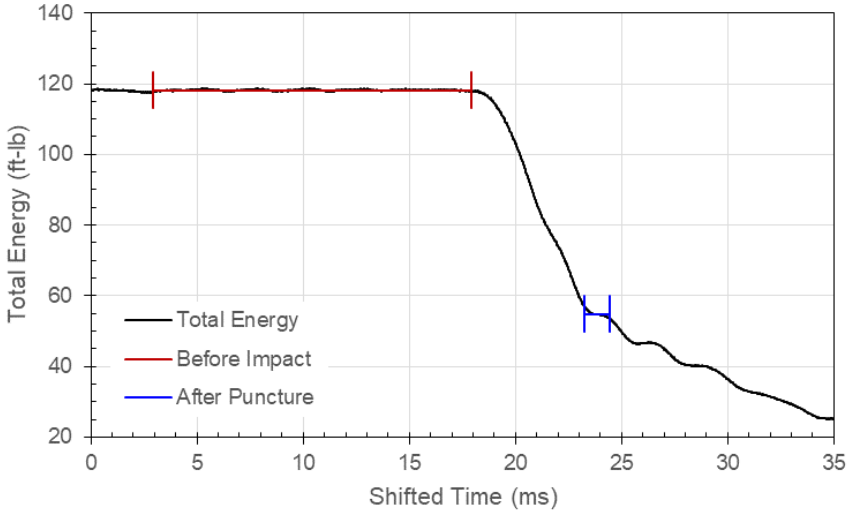

Figure 114: Carriage Total Energy in Test 61 with Specimen T125-09 and 0.500-Inch Probe

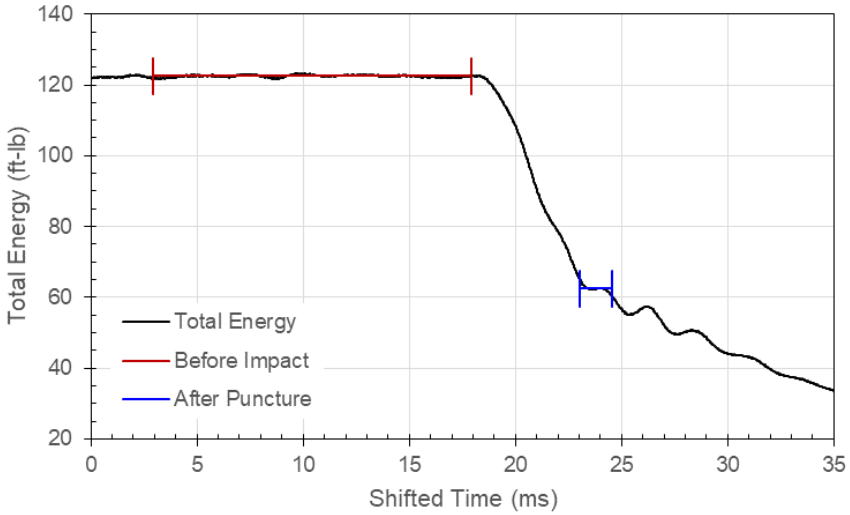

Figure 115: Carriage Total Energy in Test 62 with Specimen T125-10 and 0.500-Inch Probe

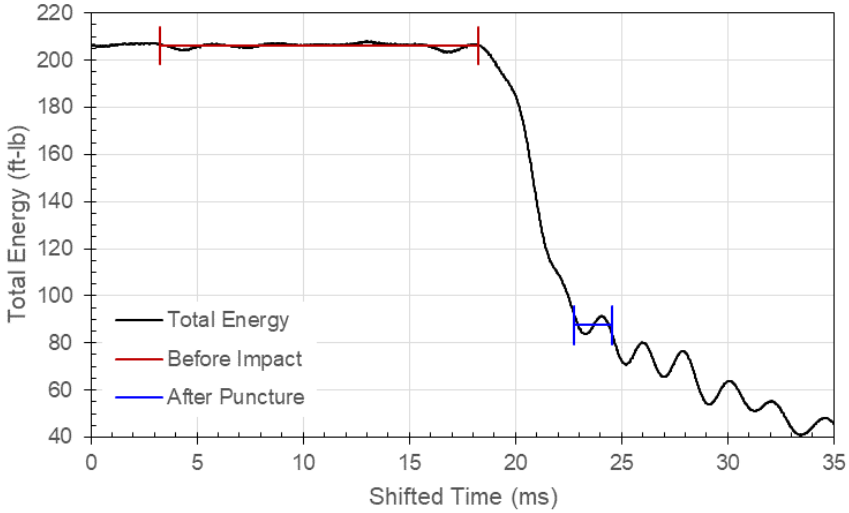

Figure 116: Carriage Total Energy in Test 64 with Specimen T125-11 and 1.000-Inch Probe

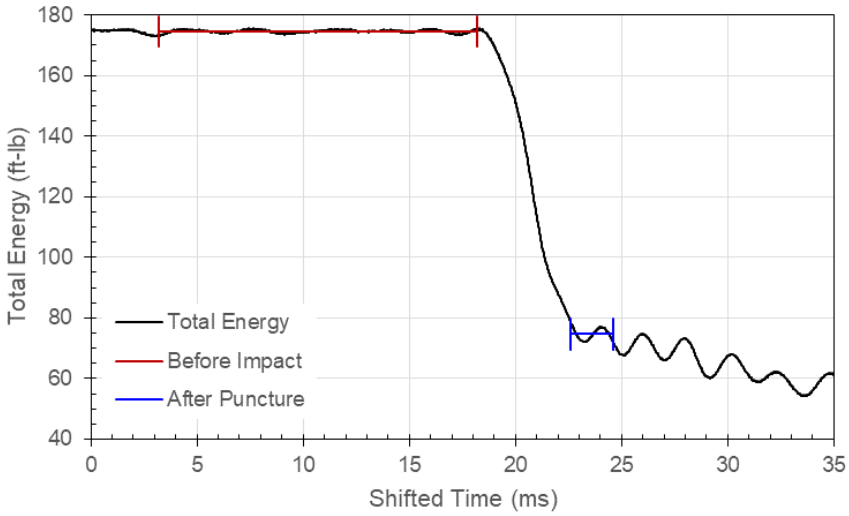

Figure 117: Carriage Total Energy in Test 65 with Specimen T125-12 and 1.000-Inch Probe

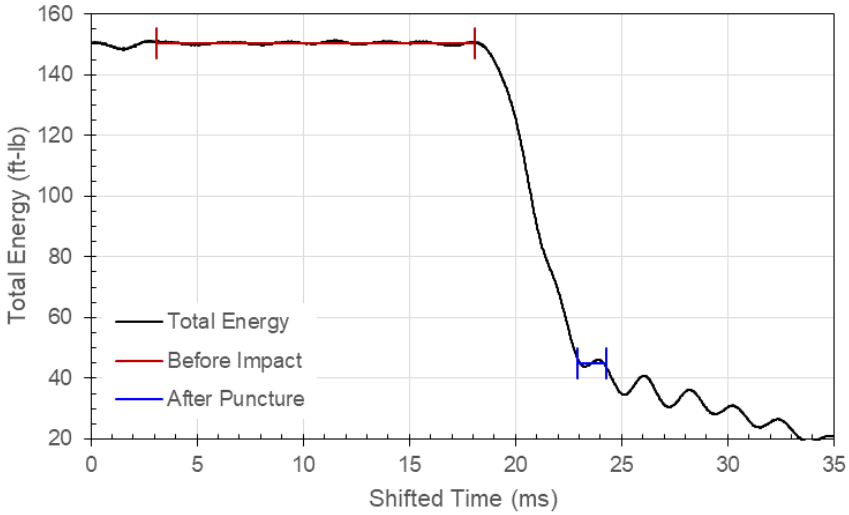

Figure 118: Carriage Total Energy in Test 66 with Specimen T125-13 and 1.000-Inch Probe

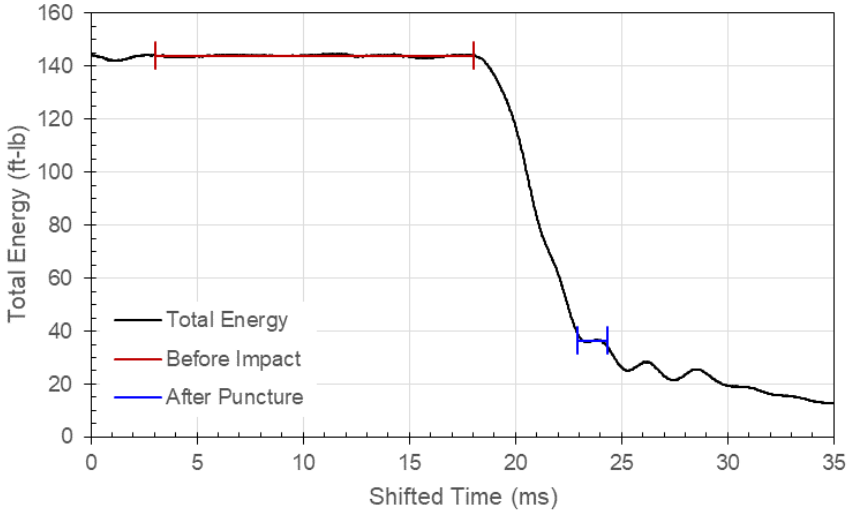

Figure 119: Carriage Total Energy in Test 67 with Specimen T125-14 and 1.000-Inch Probe

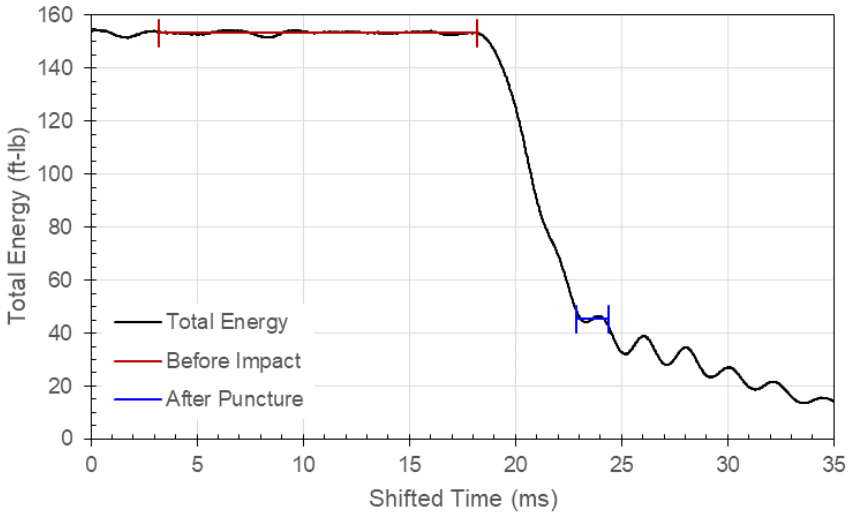

Figure 120: Carriage Total Energy in Test 68 with Specimen T125-15 and 1.000-Inch Probe

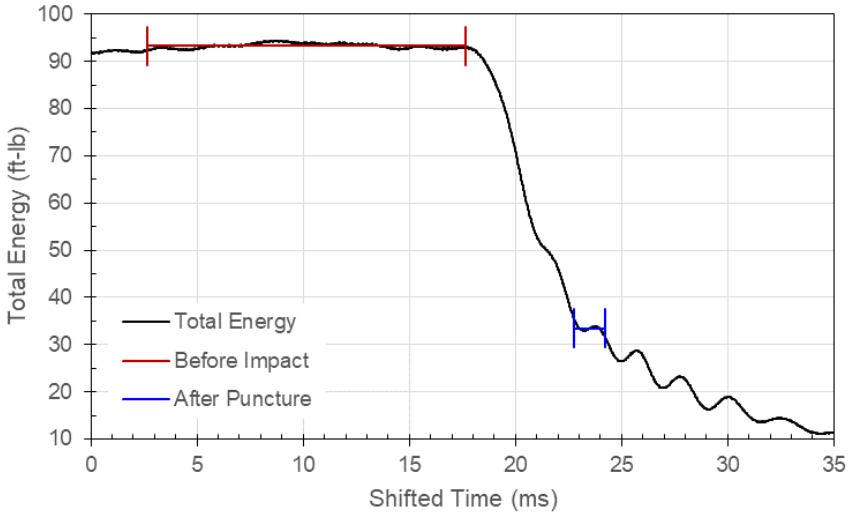

Figure 121: Carriage Total Energy in Test 73 with Specimen T188-01 and 0.250-Inch Probe

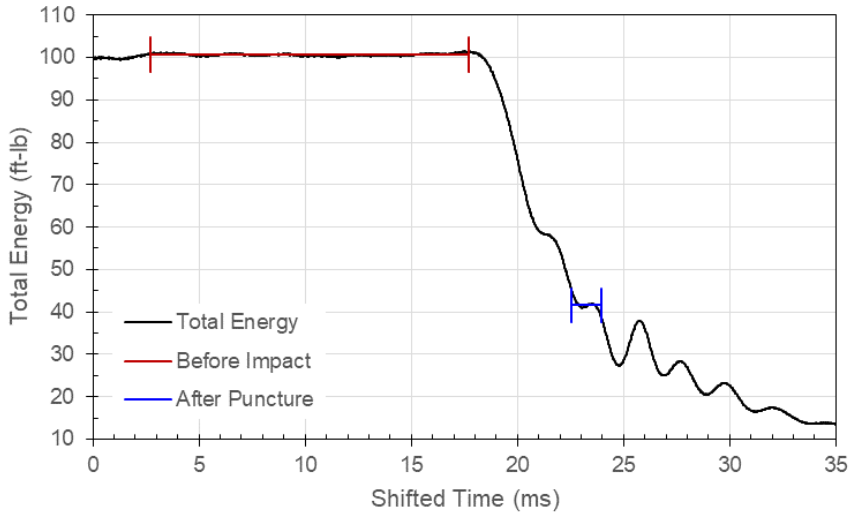

Figure 122: Carriage Total Energy in Test 74 with Specimen T188-02 and 0.250-Inch Probe

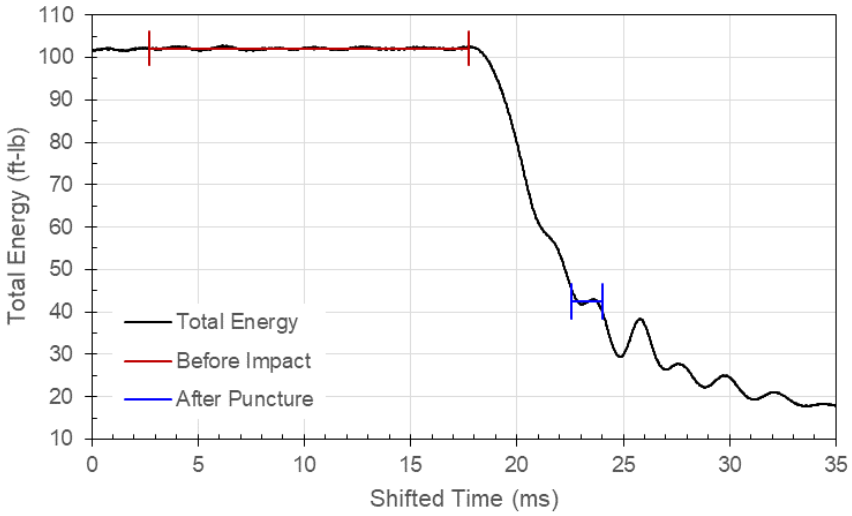

Figure 123: Carriage Total Energy in Test 75 with Specimen T188-03 and 0.250-Inch Probe

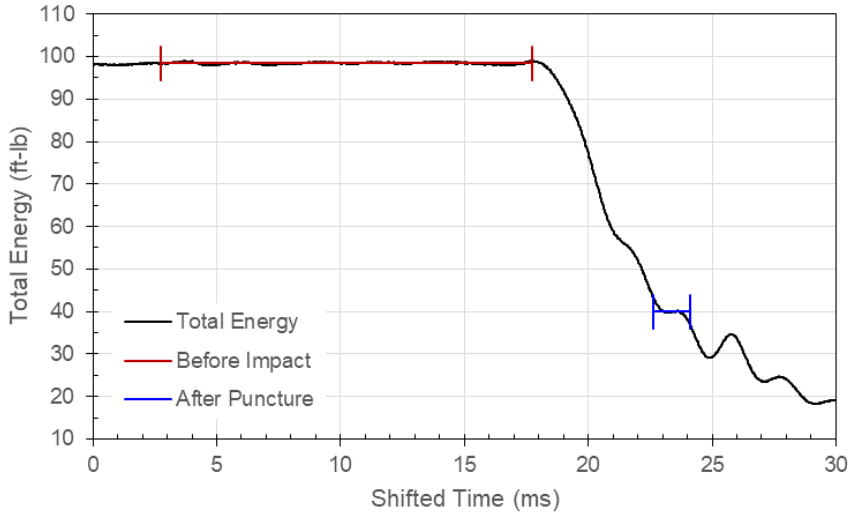

Figure 124: Carriage Total Energy in Test 76 with Specimen T188-04 and 0.250-Inch Probe

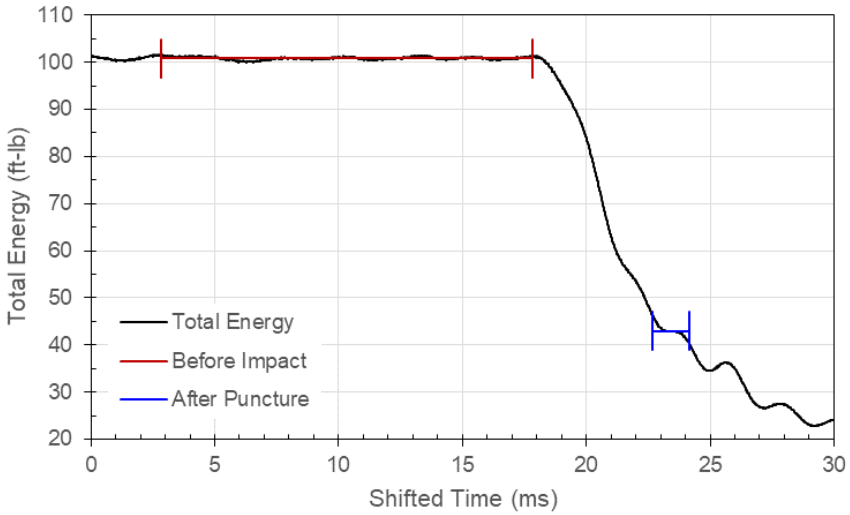

Figure 125: Carriage Total Energy in Test 77 with Specimen T188-05 and 0.250-Inch Probe

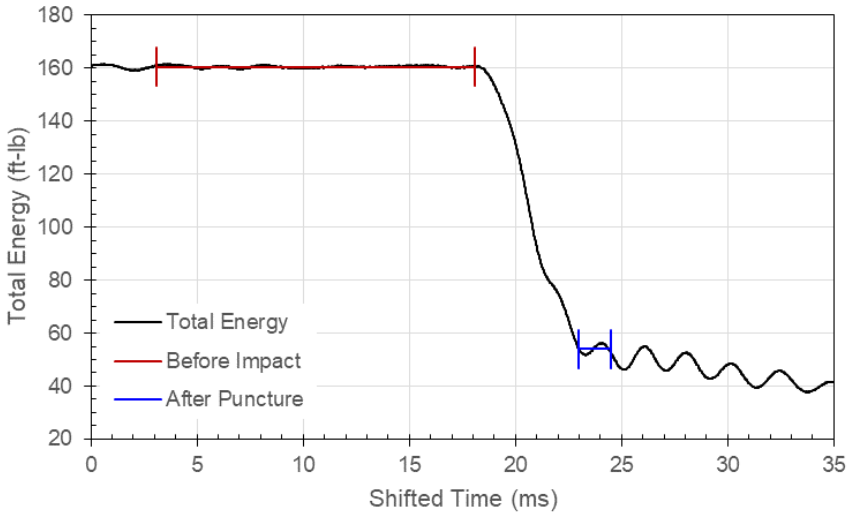

Figure 126: Carriage Total Energy in Test 78 with Specimen T188-06 and 0.500-Inch Probe

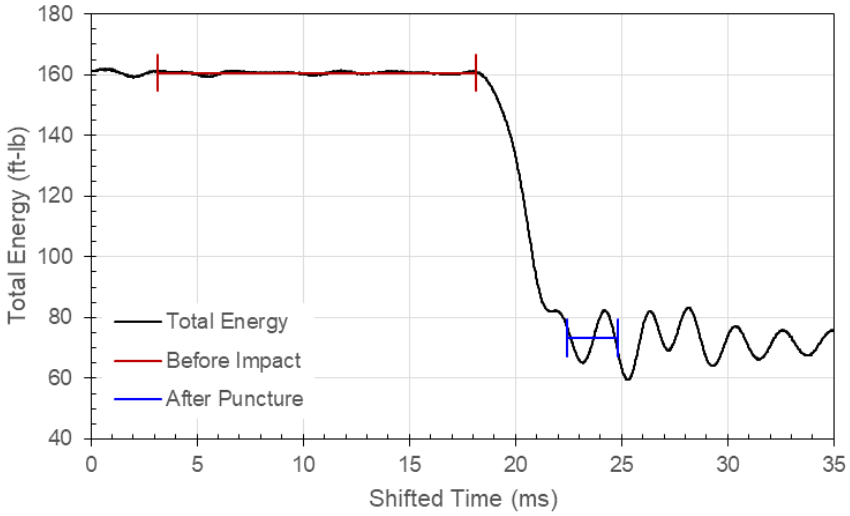

Figure 127: Carriage Total Energy in Test 79 with Specimen T188-07 and 0.500-Inch Probe

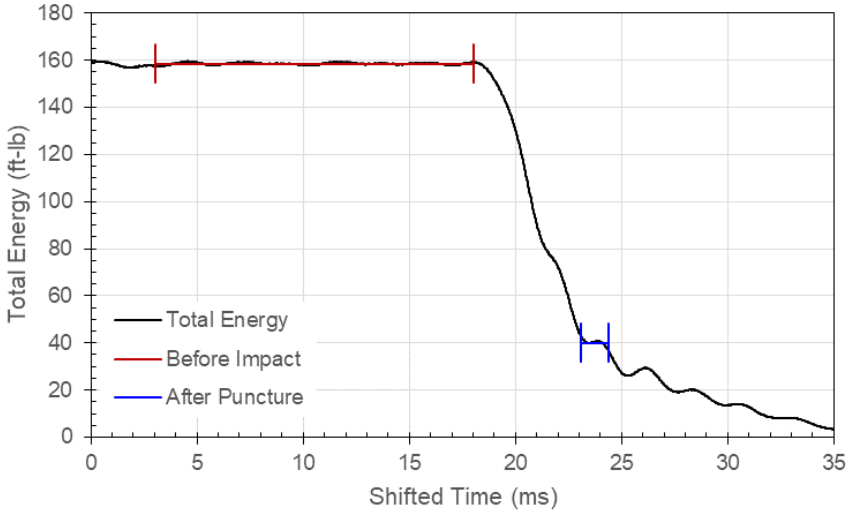

Figure 128: Carriage Total Energy in Test 80 with Specimen T188-08 and 0.500-Inch Probe

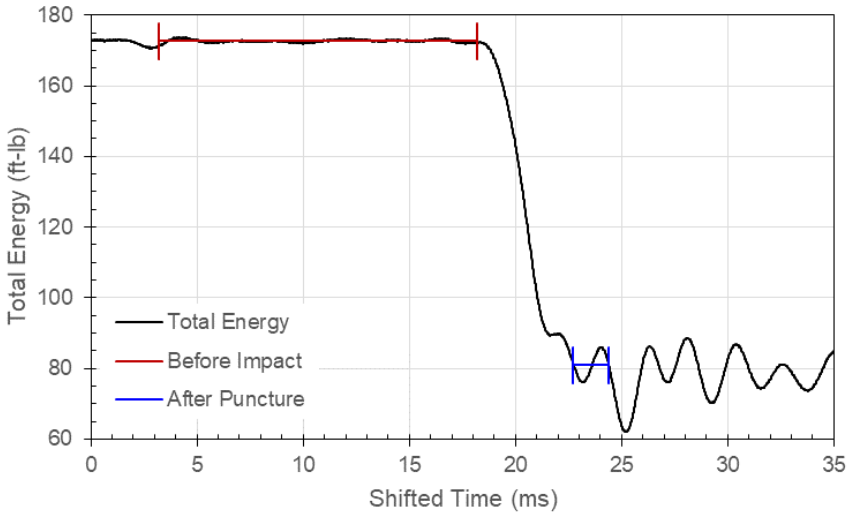

Figure 129: Carriage Total Energy in Test 81 with Specimen T188-09 and 0.500-Inch Probe

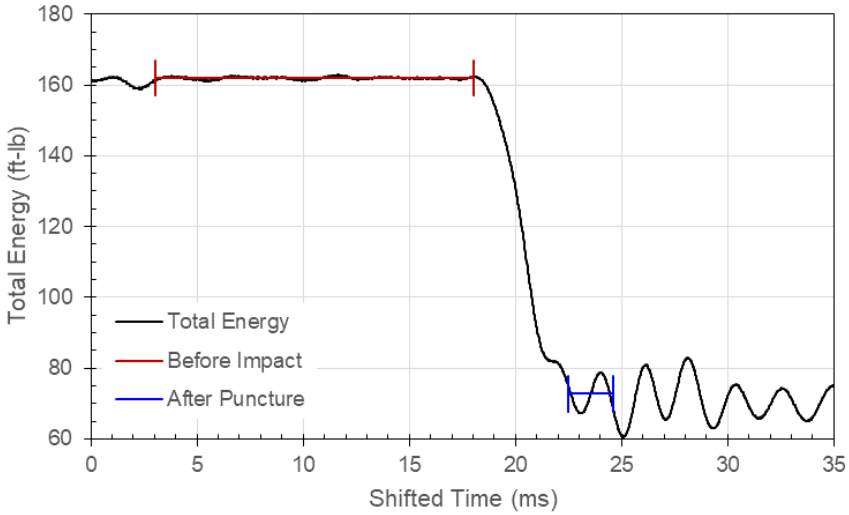

Figure 130: Carriage Total Energy in Test 82 with Specimen T188-10 and 0.500-Inch Probe

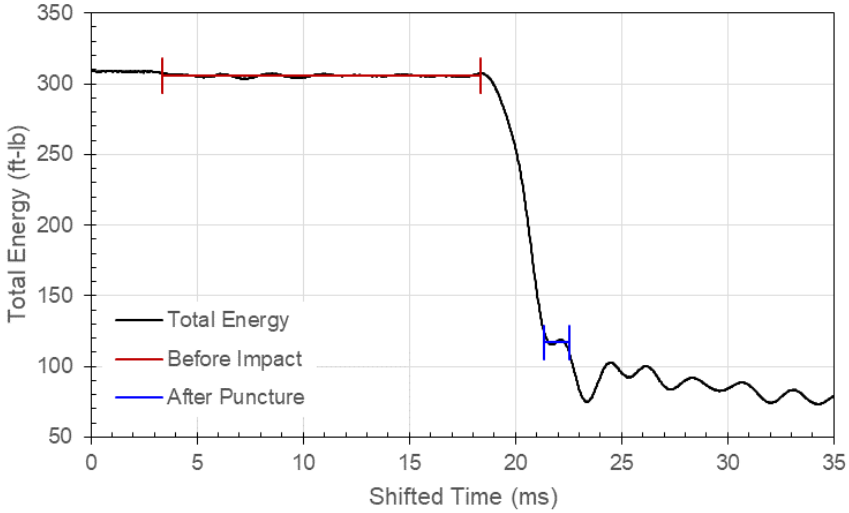

Figure 131: Carriage Total Energy in Test 83 with Specimen T188-11 and 1.000-Inch Probe

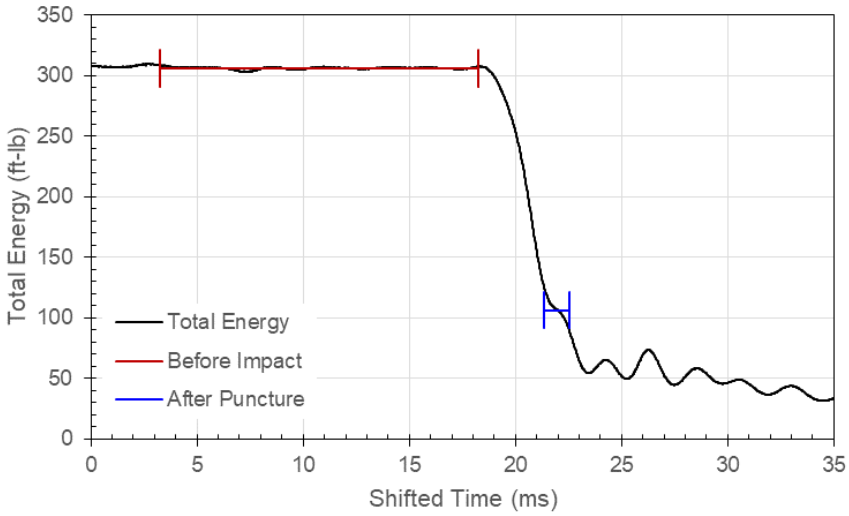

Figure 132: Carriage Total Energy in Test 84 with Specimen T188-12 and 1.000-Inch Probe

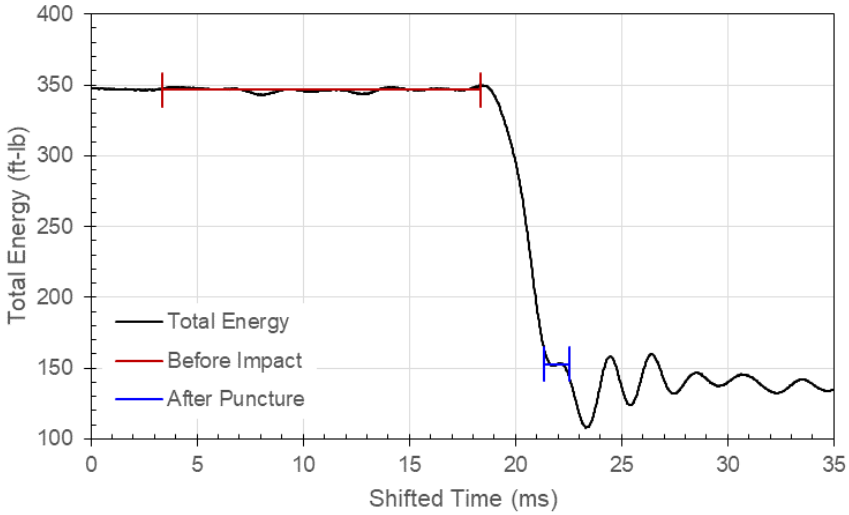

Figure 133: Carriage Total Energy in Test 85 with Specimen T188-13 and 1.000-Inch Probe

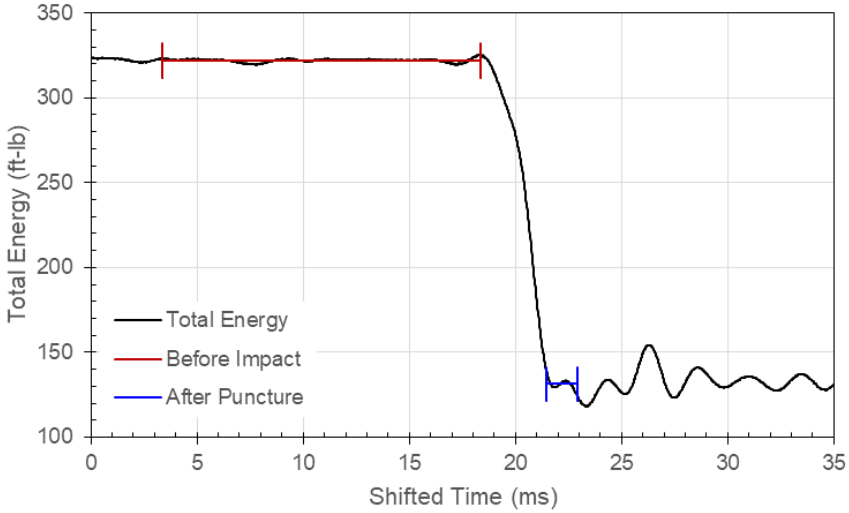

Figure 134: Carriage Total Energy in Test 86 with Specimen T188-14 and 1.000-Inch Probe

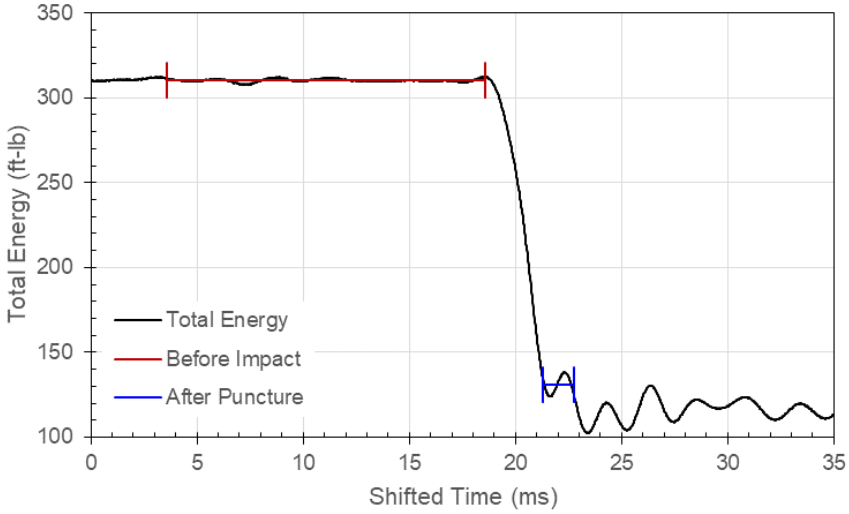

Figure 135: Carriage Total Energy in Test 87 with Specimen T188-15 and 1.000-Inch Probe

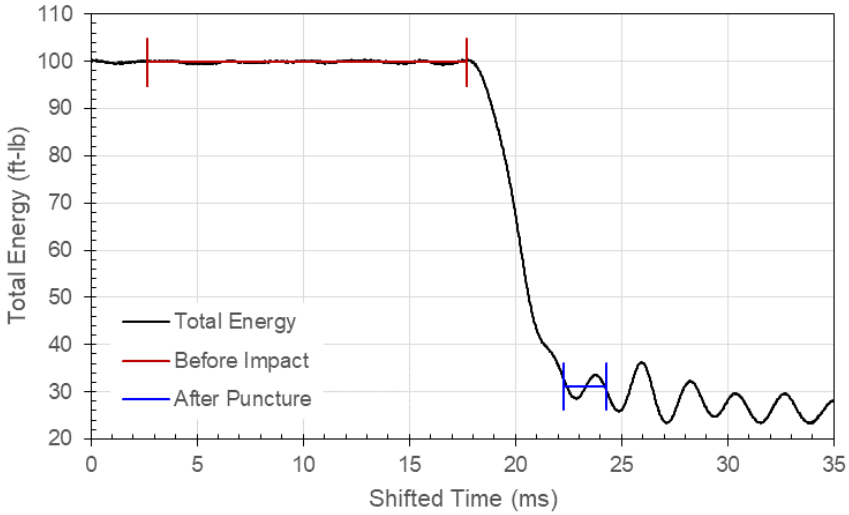

Figure 136: Carriage Total Energy in Test 88 with Specimen T250-01 and 0.250-Inch Probe

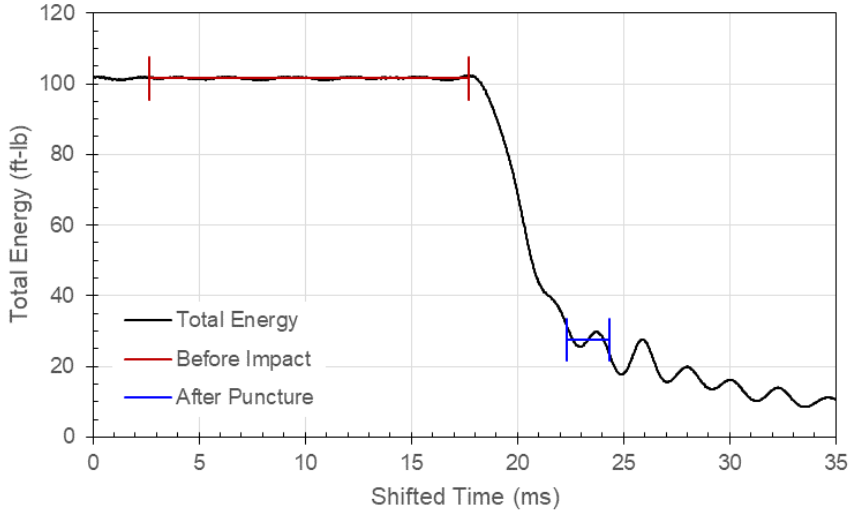

Figure 137: Carriage Total Energy in Test 89 with Specimen T250-02 and 0.250-Inch Probe

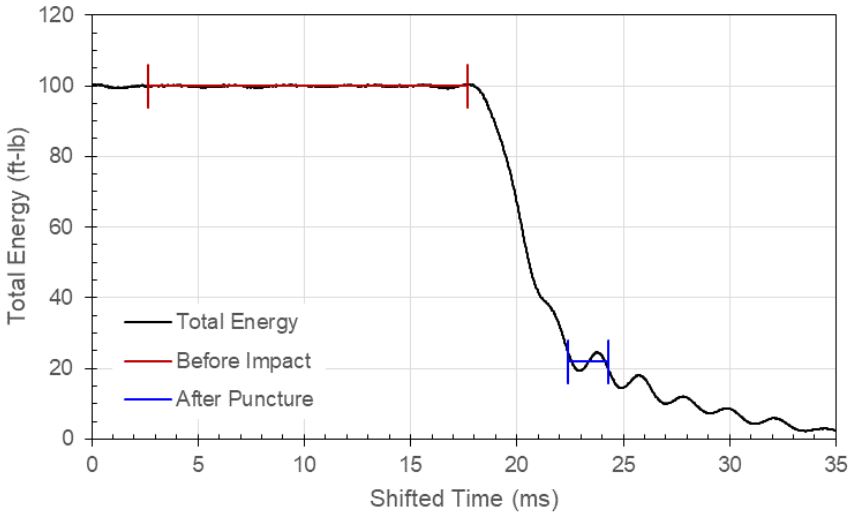

Figure 138: Carriage Total Energy in Test 90 with Specimen T250-03 and 0.250-Inch Probe

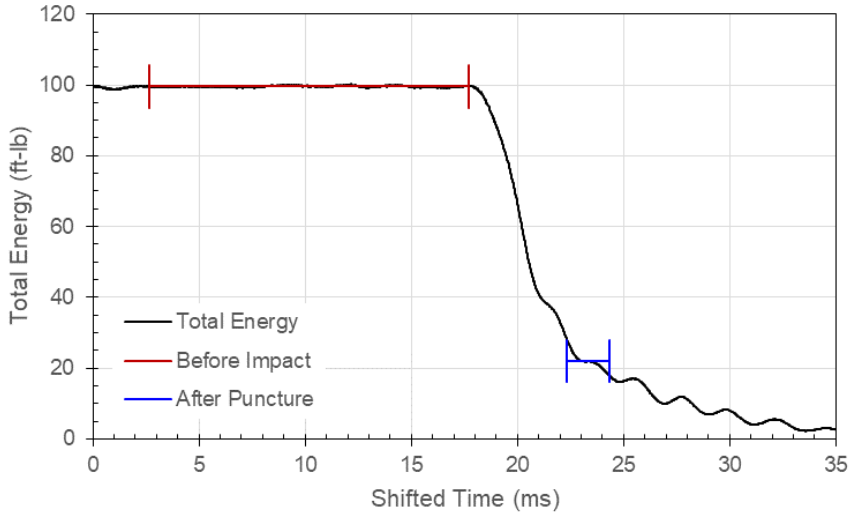

Figure 139: Carriage Total Energy in Test 91 with Specimen T250-04 and 0.250-Inch Probe

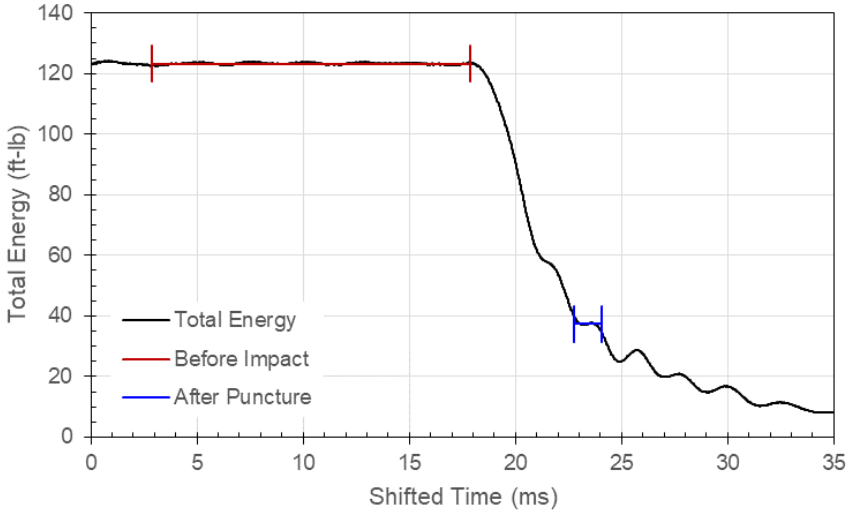

Figure 140: Carriage Total Energy in Test 92 with Specimen T250-05 and 0.250-Inch Probe

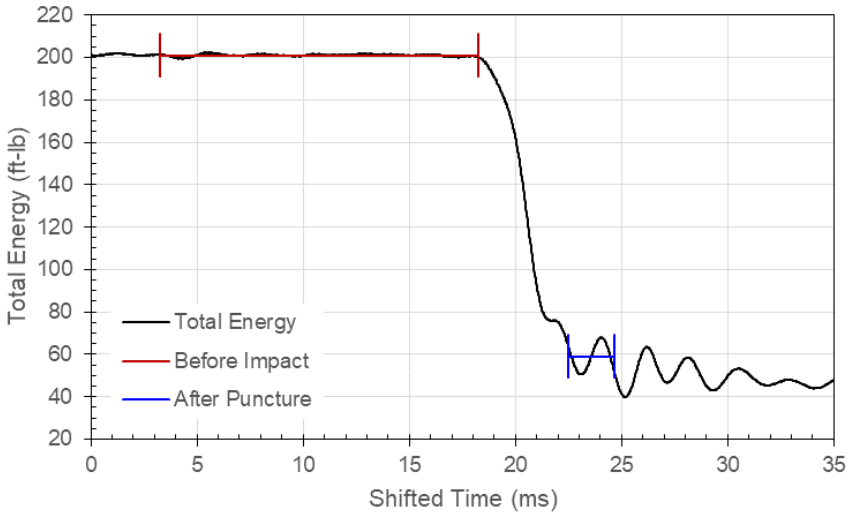

Figure 141: Carriage Total Energy in Test 94 with Specimen T250-07 and 0.500-Inch Probe

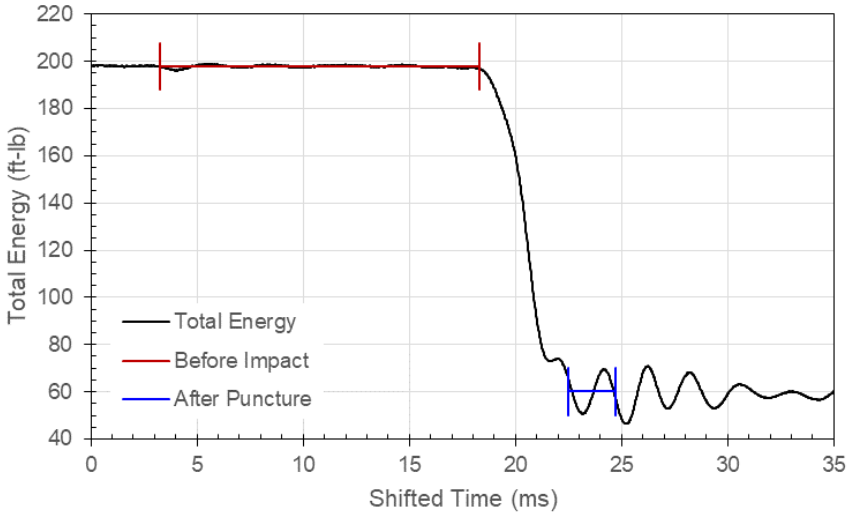

Figure 142: Carriage Total Energy in Test 95 with Specimen T250-08 and 0.500-Inch Probe

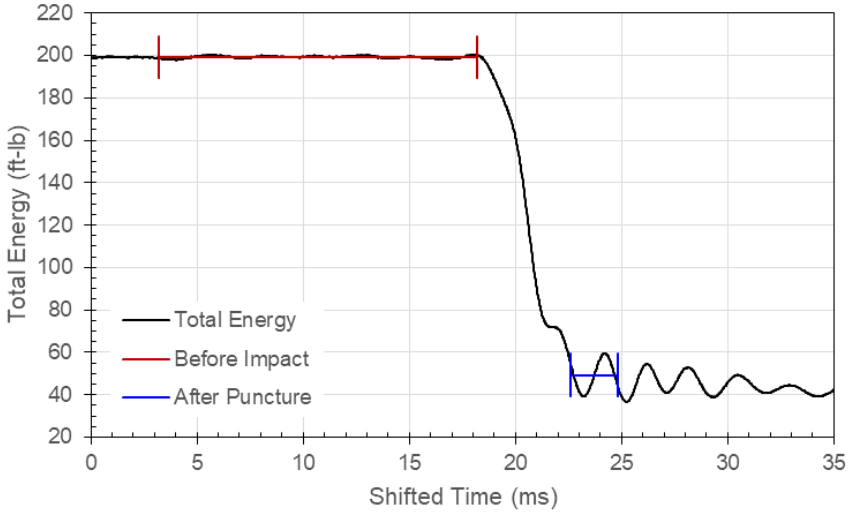

Figure 143: Carriage Total Energy in Test 96 with Specimen T250-09 and 0.500-Inch Probe

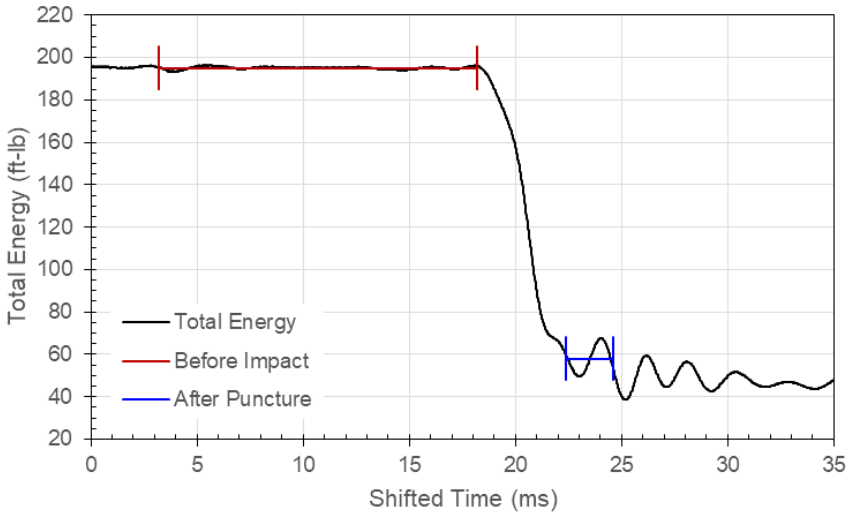

Figure 144: Carriage Total Energy in Test 97 with Specimen T250-10 and 0.500-Inch Probe

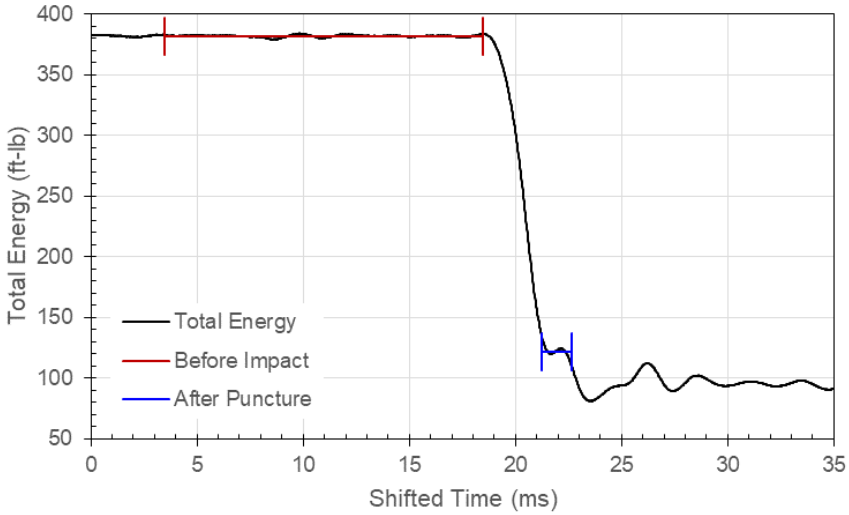

Figure 145: Carriage Total Energy in Test 98 with Specimen T250-11 and 1.000-Inch Probe

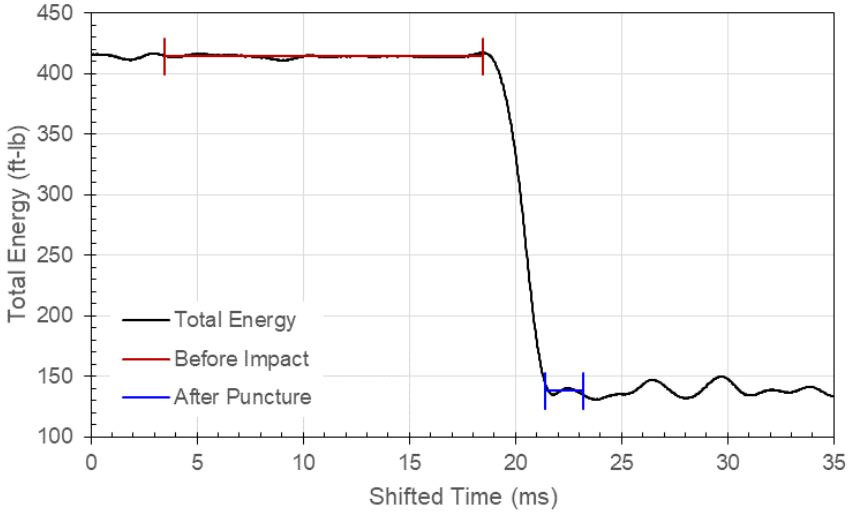

Figure 146: Carriage Total Energy in Test 99 with Specimen T250-12 and 1.000-Inch Probe

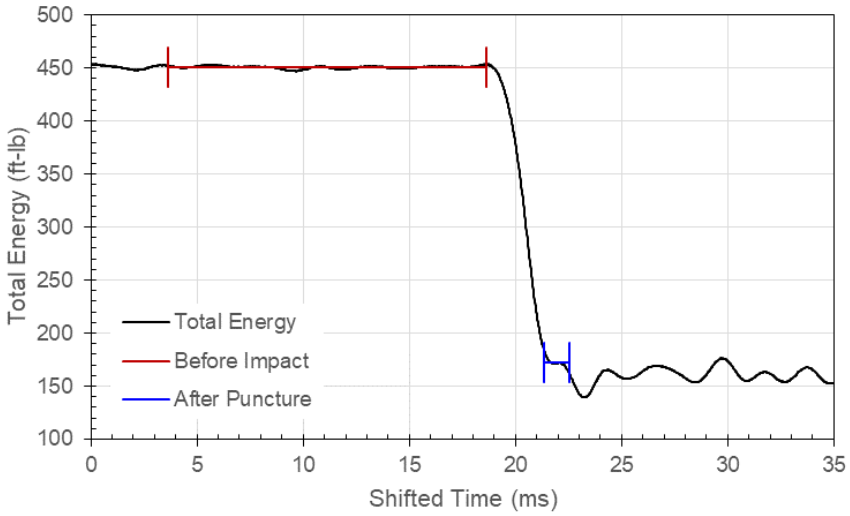

Figure 147: Carriage Total Energy in Test 100 with Specimen T250-13 and 1.000-Inch Probe

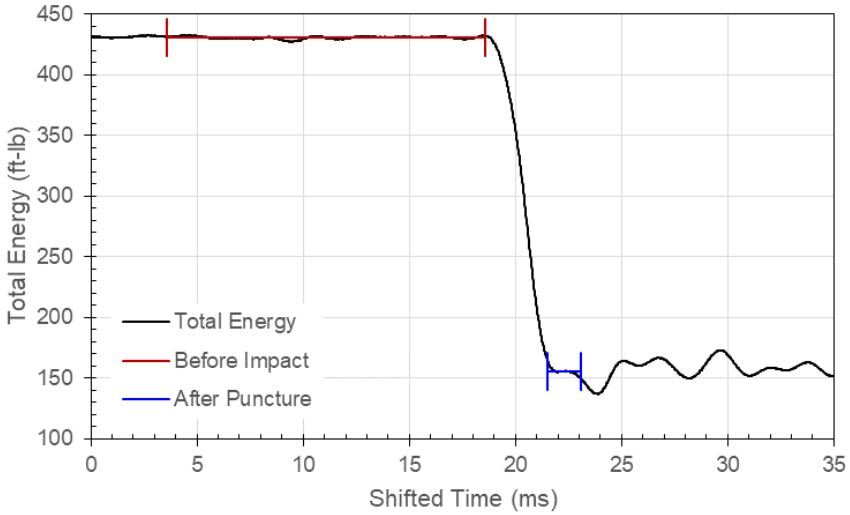

Figure 148: Carriage Total Energy in Test 101 with Specimen T250-14 and 1.000-Inch Probe

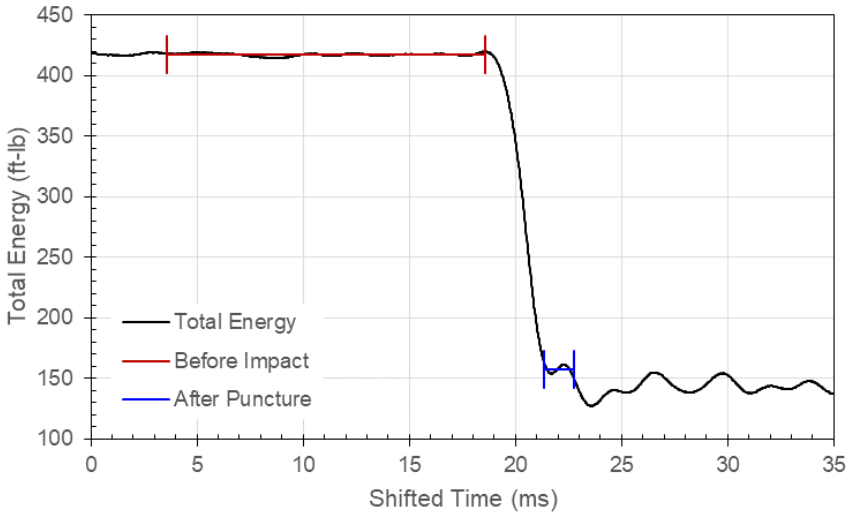

Figure 149: Carriage Total Energy in Test 102 with Specimen T250-15 and 1.000-Inch Probe

Appendix C: Velocity

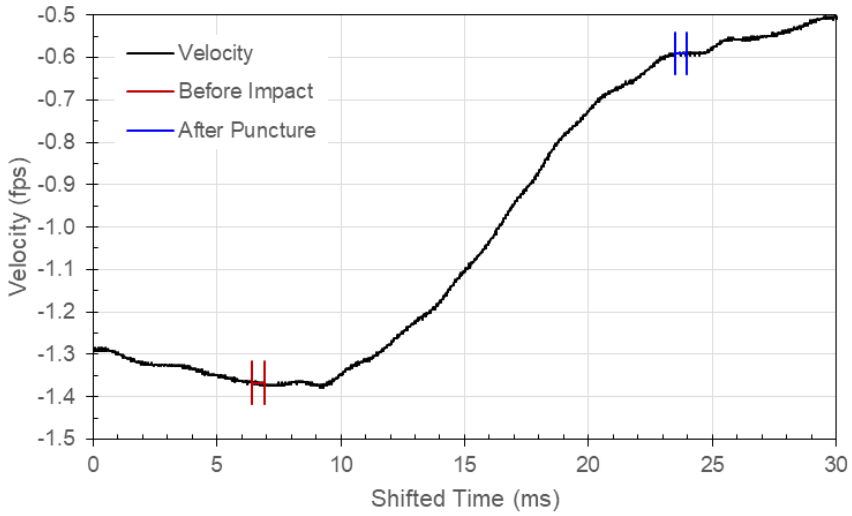

Figure 150: Carriage Velocity in Test 35 with Specimen T063-02 and 0.250-Inch Probe

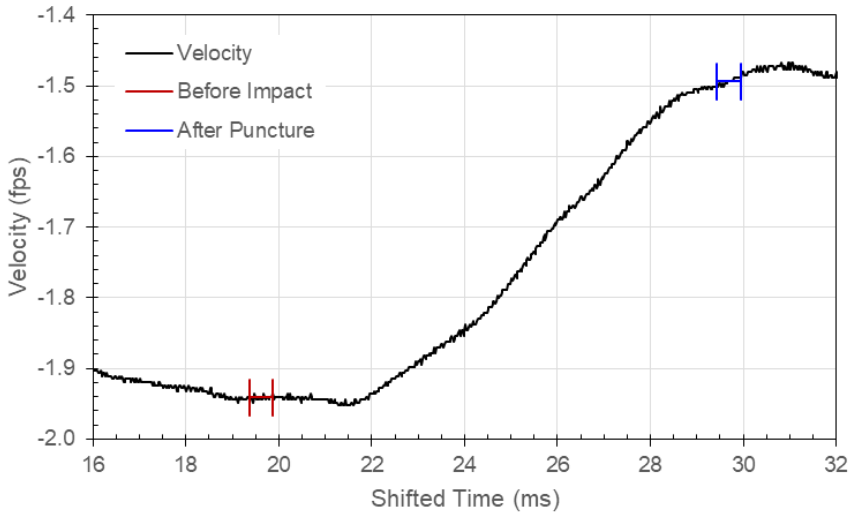

Figure 151: Carriage Velocity in Test 36 with Specimen T063-04 and 0.250-Inch Probe

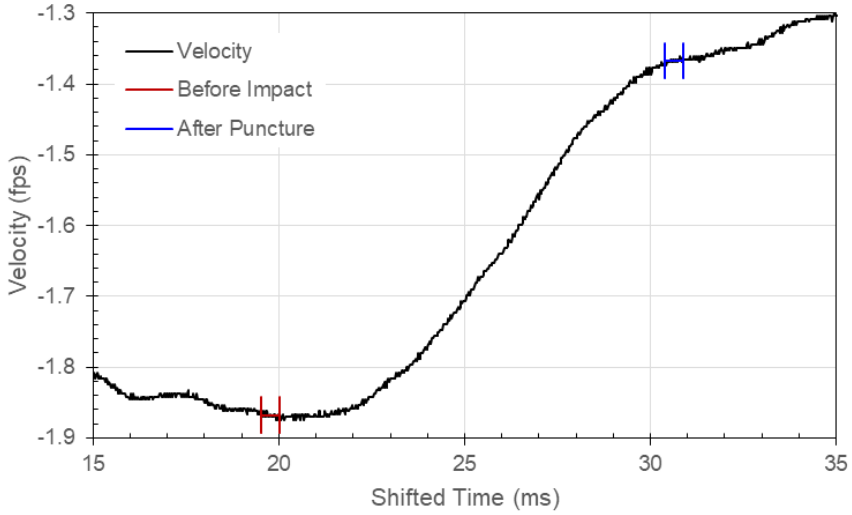

Figure 152: Carriage Velocity in Test 37 with Specimen T063-05 and 0.250-Inch Probe

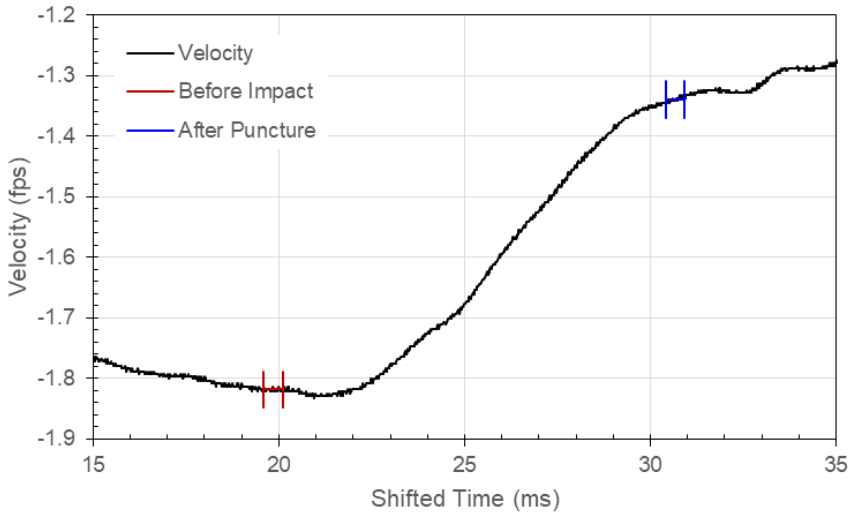

Figure 153: Carriage Velocity in Test 38 with Specimen T063-06 and 0.250-Inch Probe

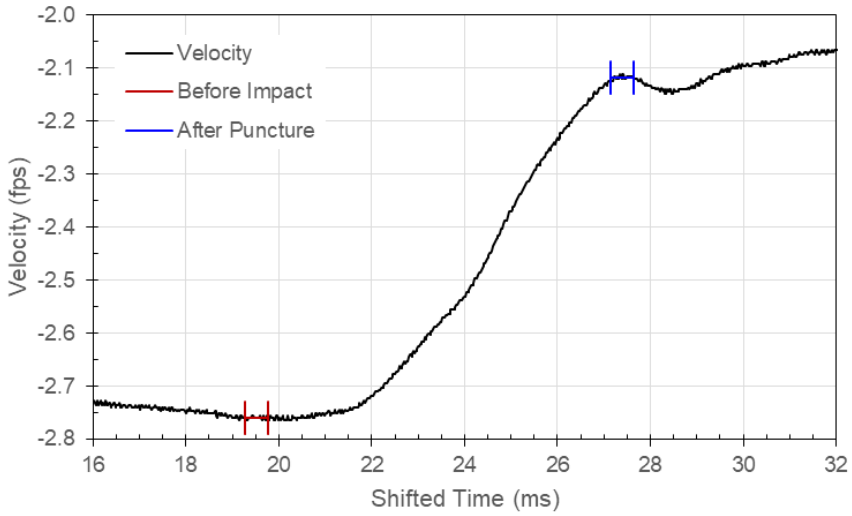

Figure 154: Carriage Velocity in Test 39 with Specimen T063-07 and 0.500-Inch Probe

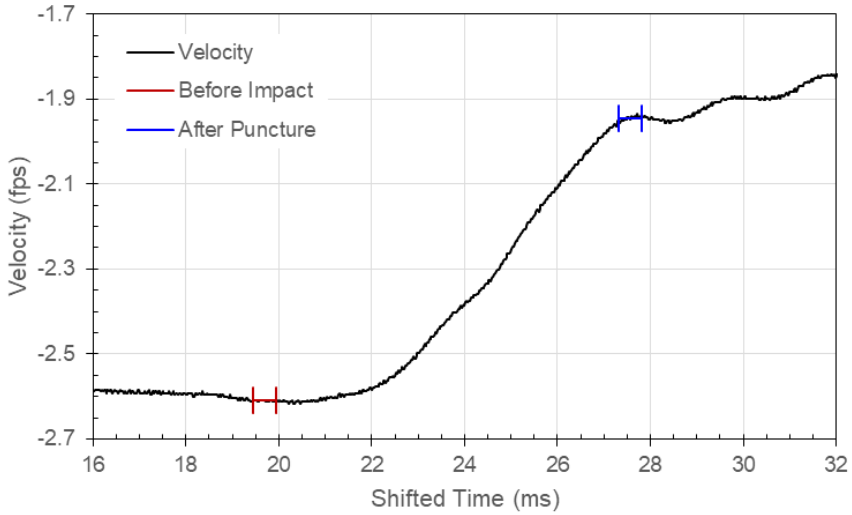

Figure 155: Carriage Velocity in Test 40 with Specimen T063-08 and 0.500-Inch Probe

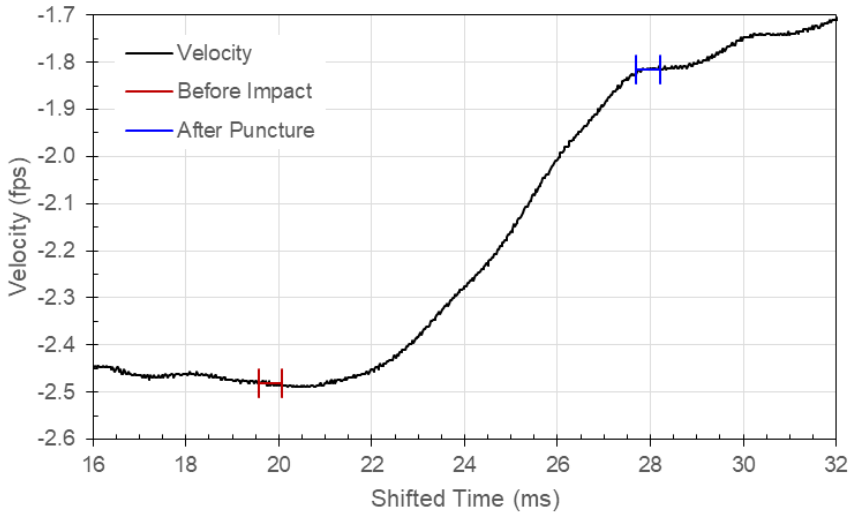

Figure 156: Carriage Velocity in Test 41 with Specimen T063-09 and 0.500-Inch Probe

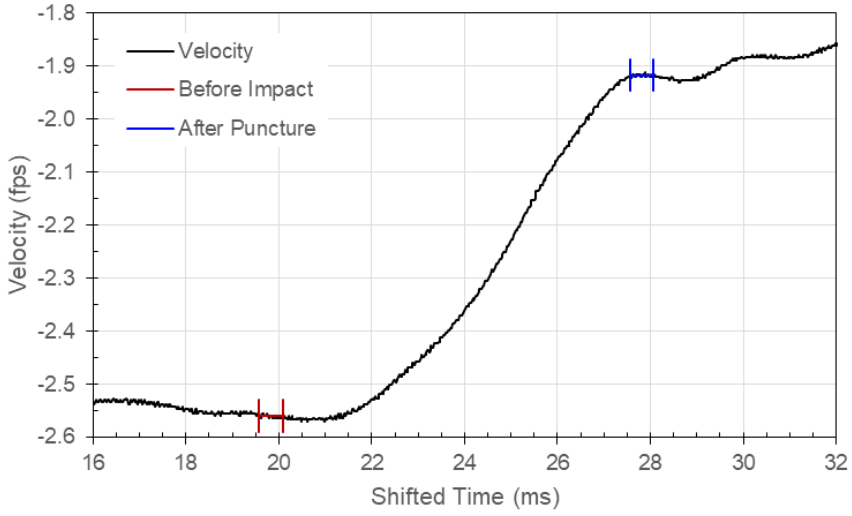

Figure 157: Carriage Velocity in Test 42 with Specimen T063-10 and 0.500-Inch Probe

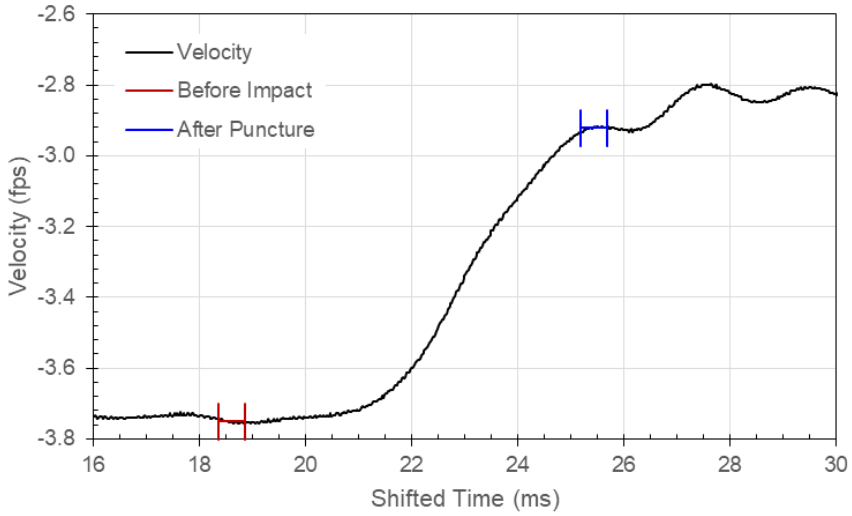

Figure 158: Carriage Velocity in Test 43 with Specimen T063-11 and 1.000-Inch Probe

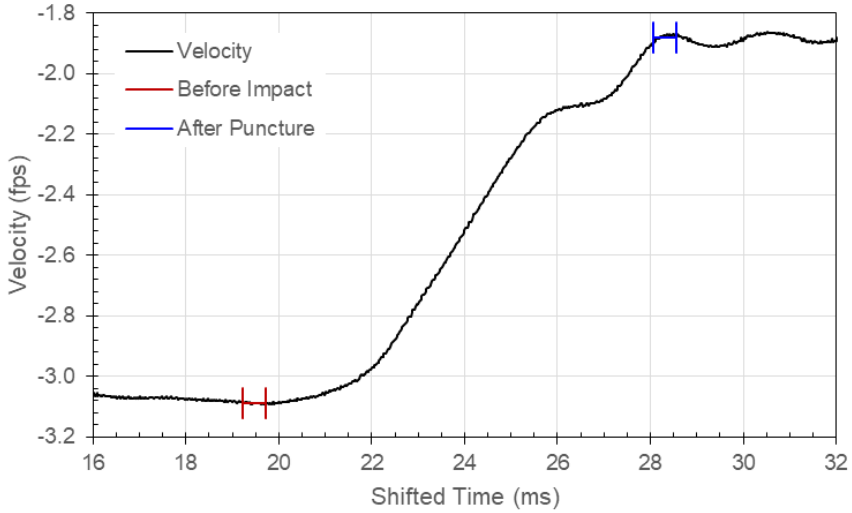

Figure 159: Carriage Velocity in Test 44 with Specimen T063-12 and 1.000-Inch Probe

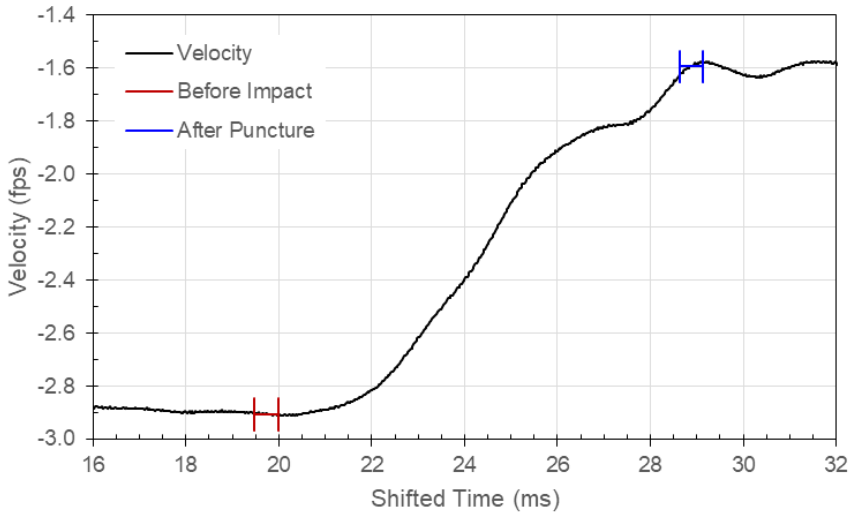

Figure 160: Carriage Velocity in Test 45 with Specimen T063-13 and 1.000-Inch Probe

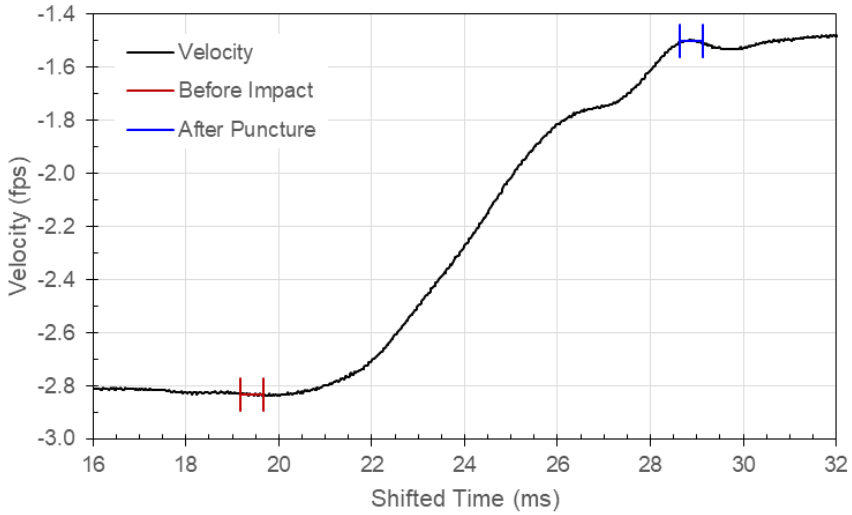

Figure 161: Carriage Velocity in Test 46 with Specimen T063-14 and 1.000-Inch Probe

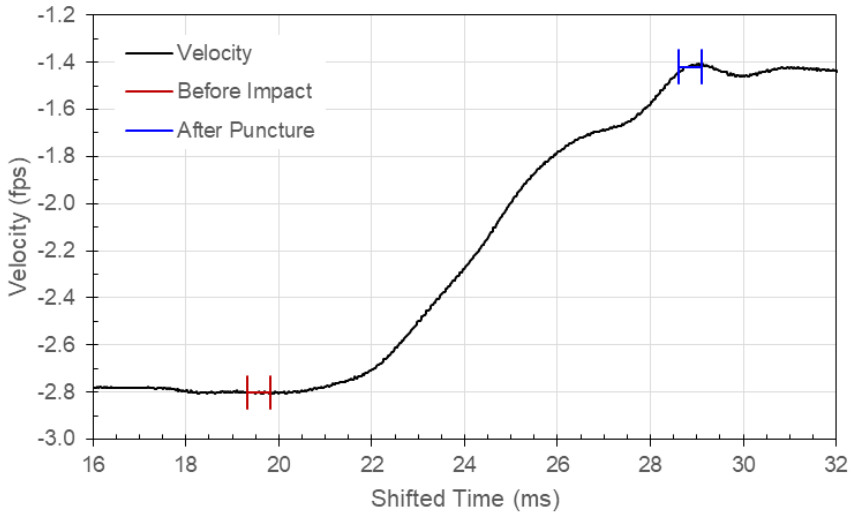

Figure 162: Carriage Velocity in Test 47 with Specimen T063-15 and 1.000-Inch Probe

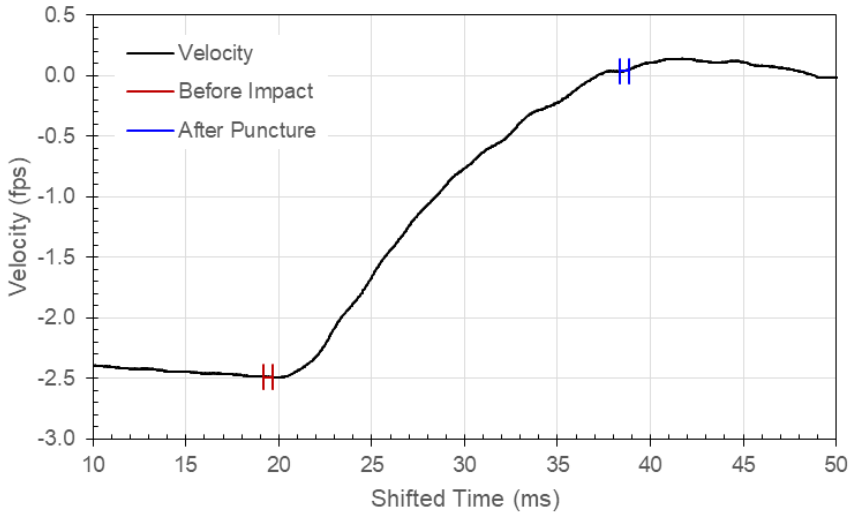

Figure 163: Carriage Velocity in Test 49 with Specimen T125-02 and 0.250-Inch Probe

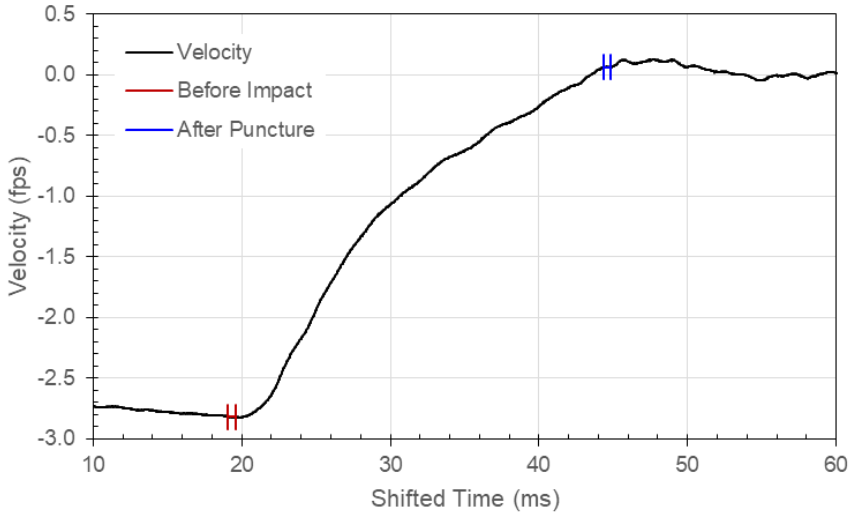

Figure 164: Carriage Velocity in Test 50 with Specimen T125-03 and 0.250-Inch Probe

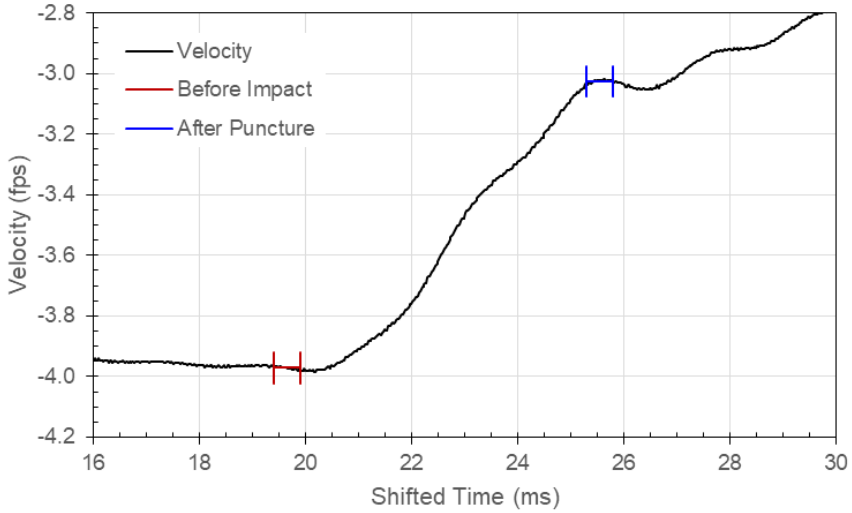

Figure 165: Carriage Velocity in Test 51 with Specimen T125-04 and 0.250-Inch Probe

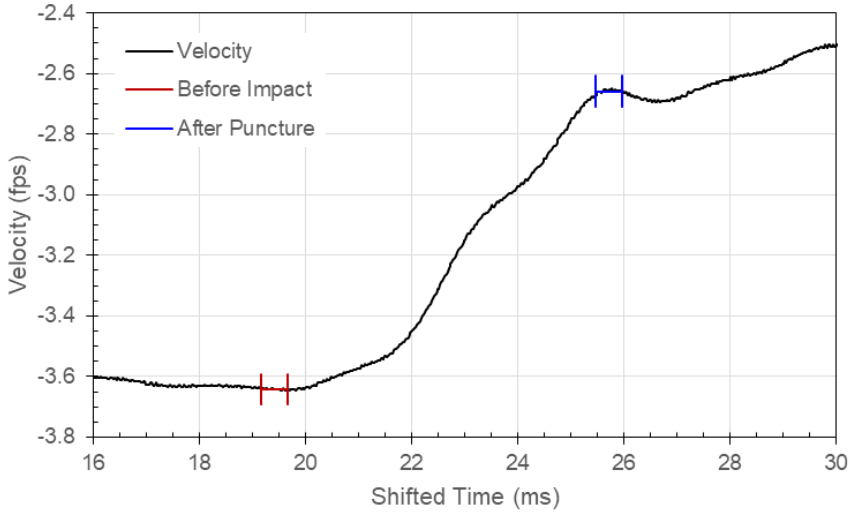

Figure 166: Carriage Velocity in Test 52 with Specimen T125-05 and 0.250-Inch Probe

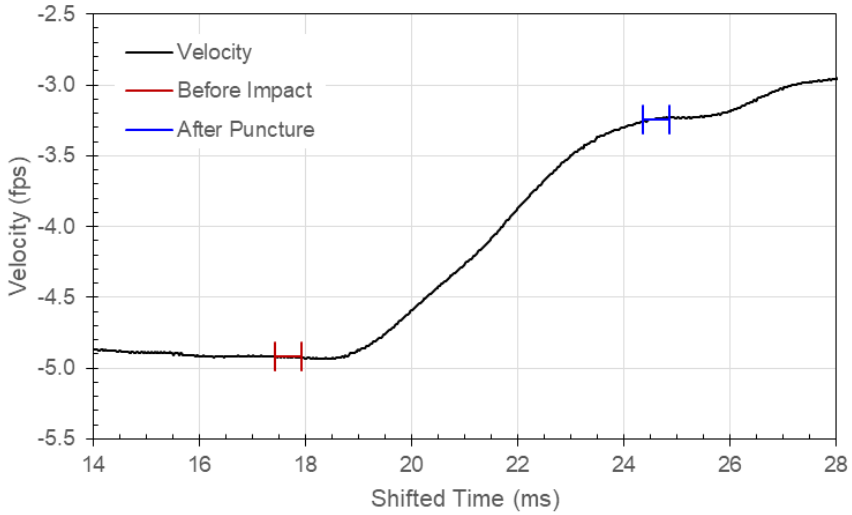

Figure 167: Carriage Velocity in Test 59 with Specimen T125-07 and 0.500-Inch Probe

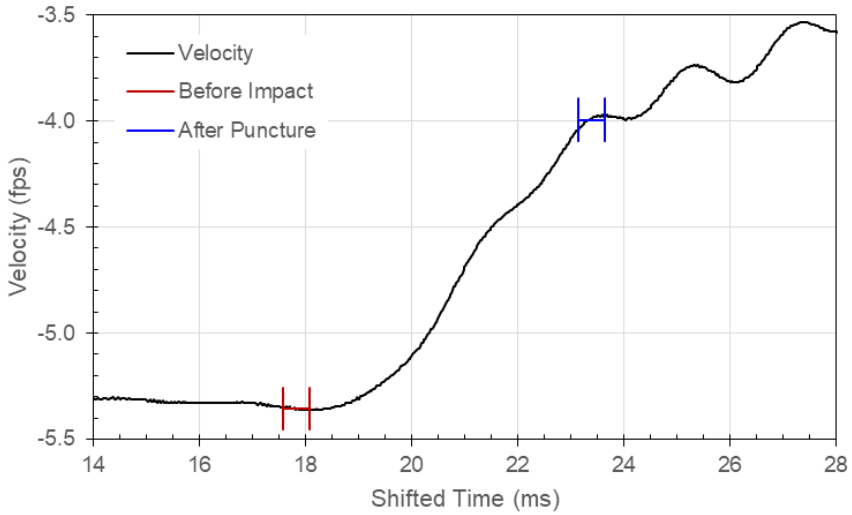

Figure 168: Carriage Velocity in Test 60 with Specimen T125-08 and 0.500-Inch Probe

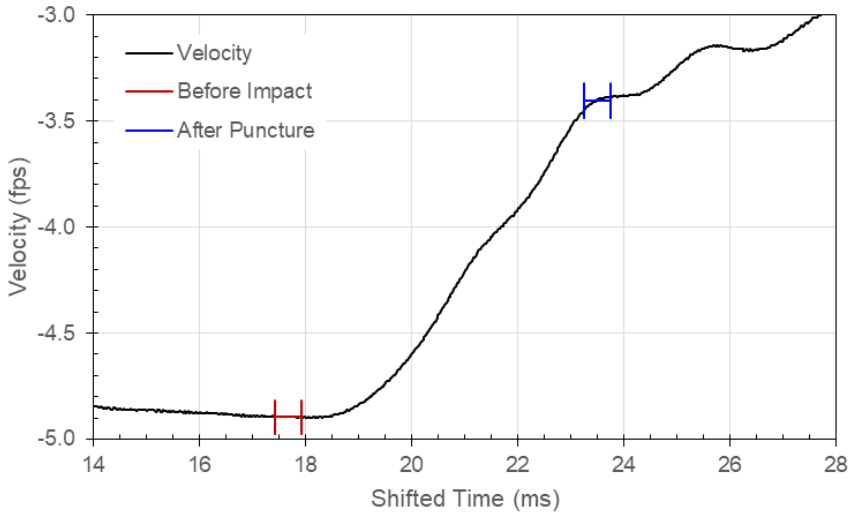

Figure 169: Carriage Velocity in Test 61 with Specimen T125-09 and 0.500-Inch Probe

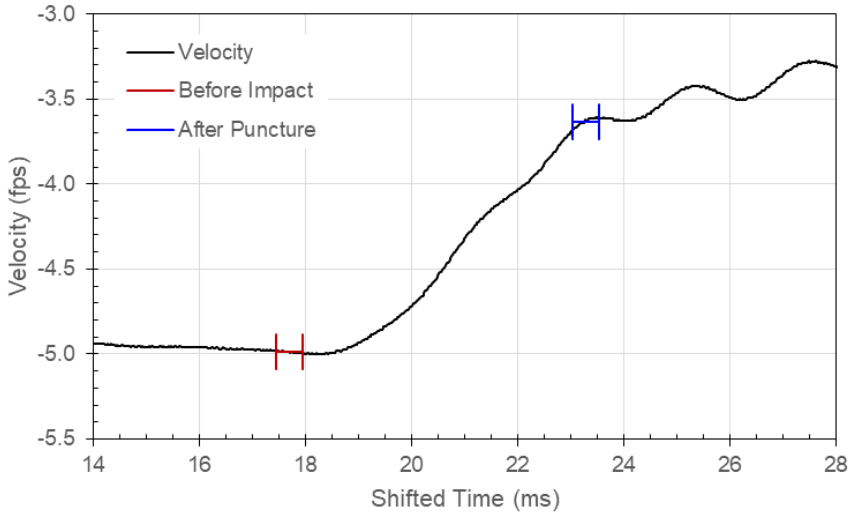

Figure 170: Carriage Velocity in Test 62 with Specimen T125-10 and 0.500-Inch Probe

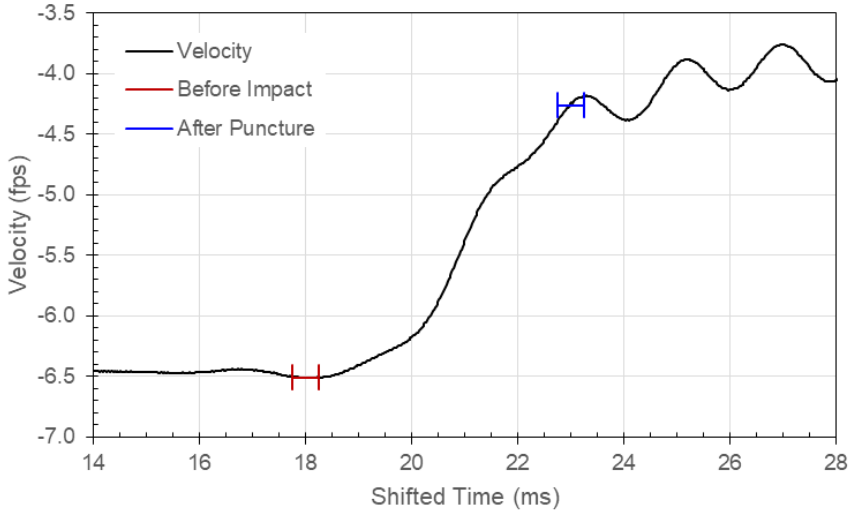

Figure 171: Carriage Velocity in Test 64 with Specimen T125-11 and 1.000-Inch Probe

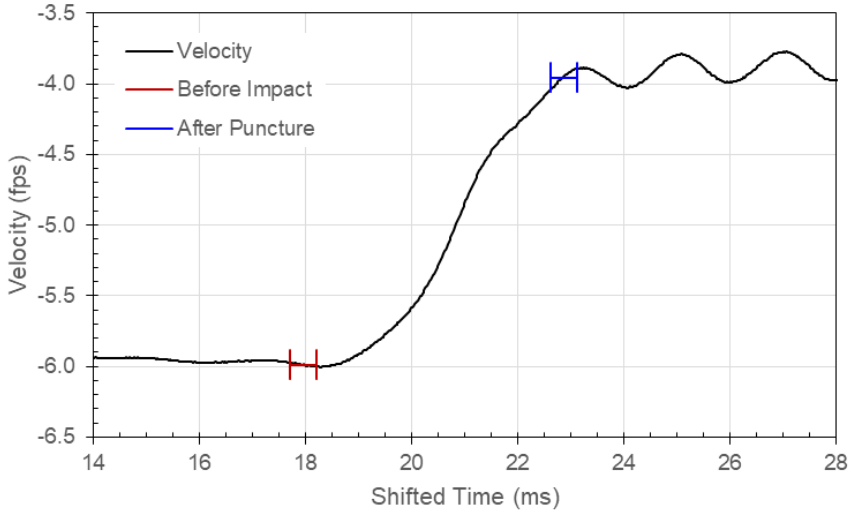

Figure 172: Carriage Velocity in Test 65 with Specimen T125-12 and 1.000-Inch Probe

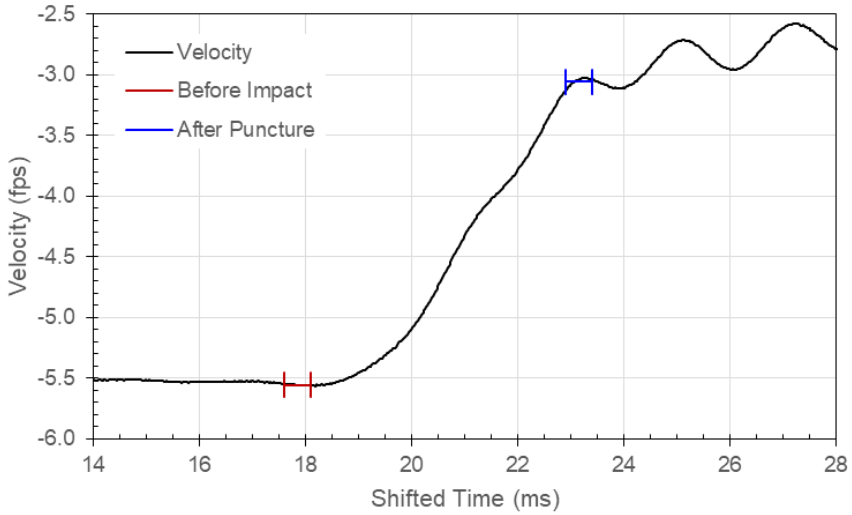

Figure 173: Carriage Velocity in Test 66 with Specimen T125-13 and 1.000-Inch Probe

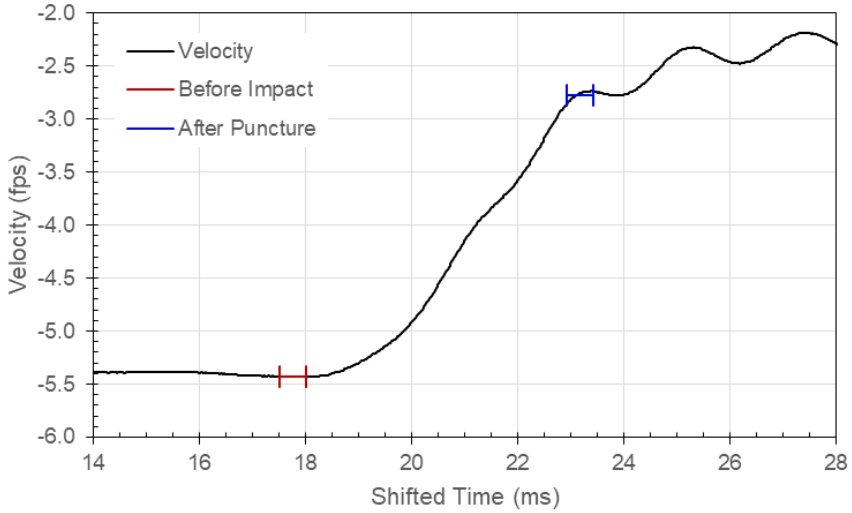

Figure 174: Carriage Velocity in Test 67 with Specimen T125-14 and 1.000-Inch Probe

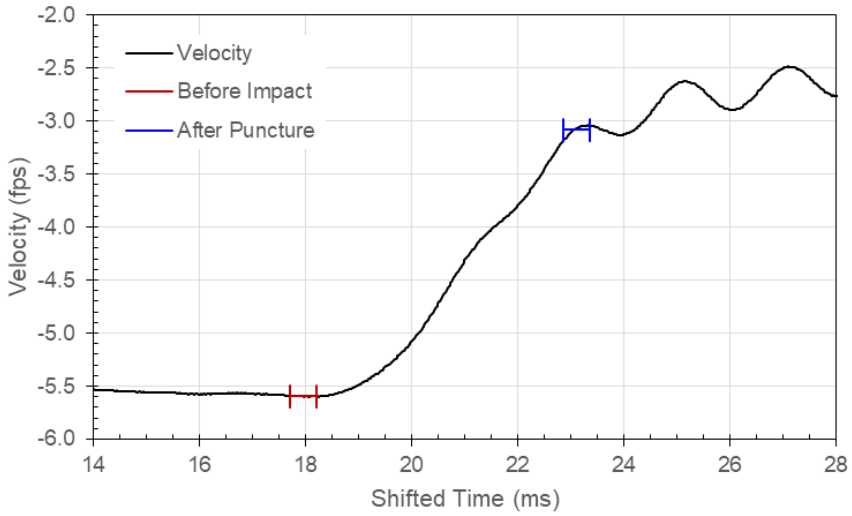

Figure 175: Carriage Velocity in Test 68 with Specimen T125-15 and 1.000-Inch Probe

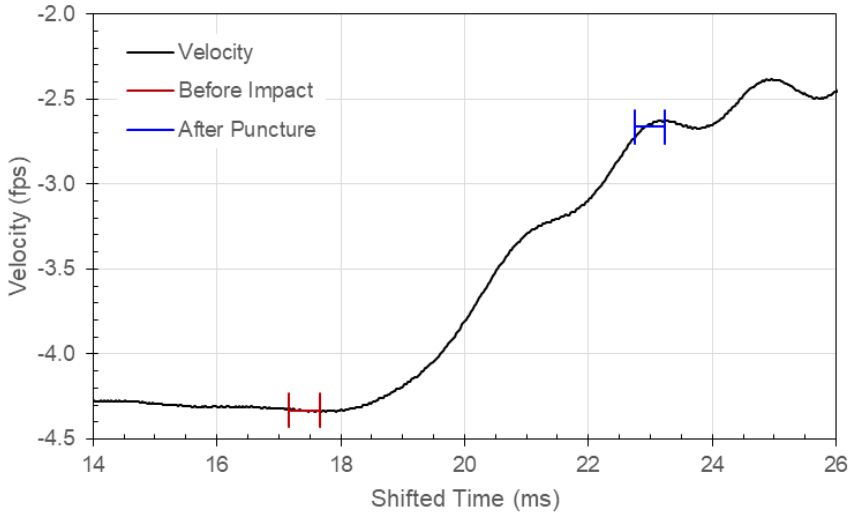

Figure 176: Carriage Velocity in Test 73 with Specimen T188-01 and 0.250-Inch Probe

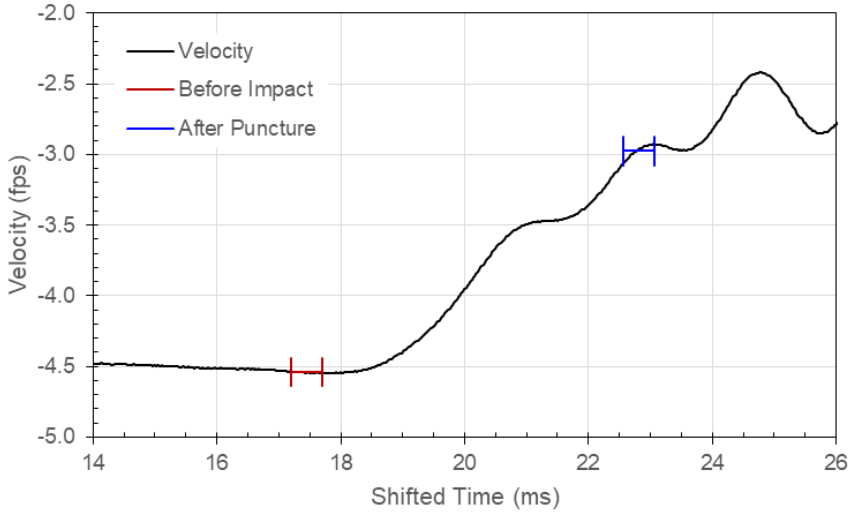

Figure 177: Carriage Velocity in Test 74 with Specimen T188-02 and 0.250-Inch Probe

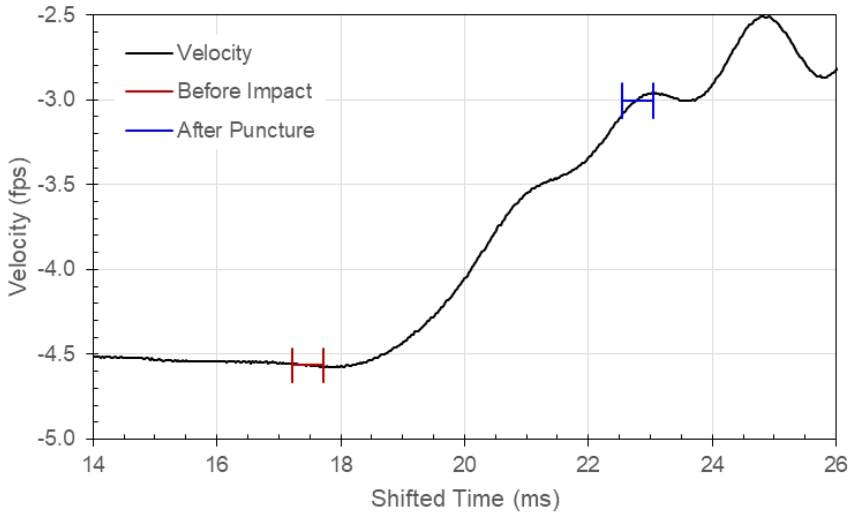

Figure 178: Carriage Velocity in Test 75 with Specimen T188-03 and 0.250-Inch Probe

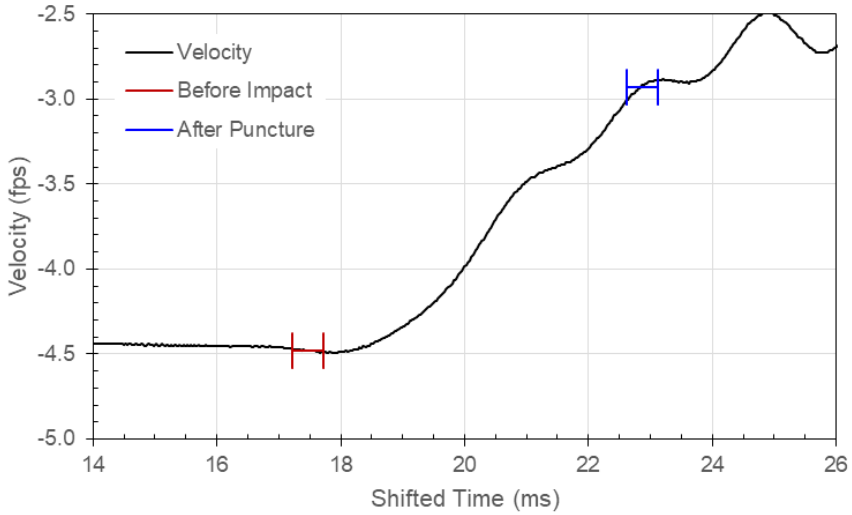

Figure 179: Carriage Velocity in Test 76 with Specimen T188-04 and 0.250-Inch Probe

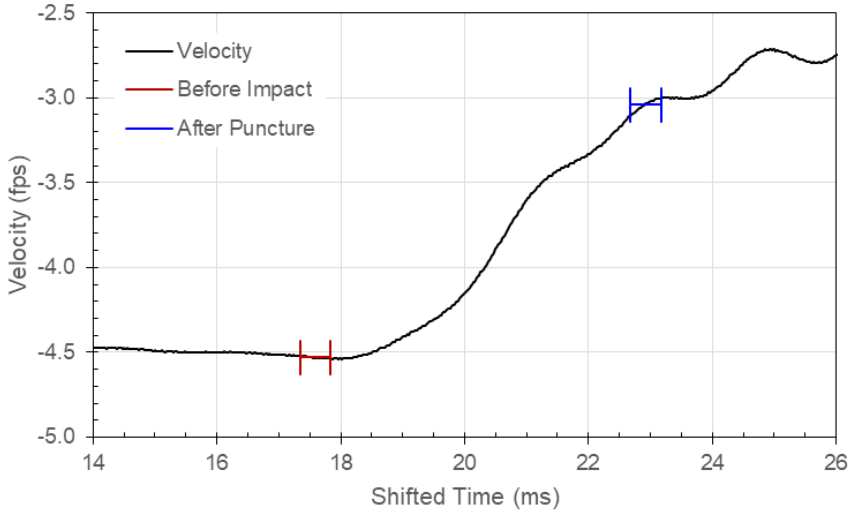

Figure 180: Carriage Velocity in Test 77 with Specimen T188-05 and 0.250-Inch Probe

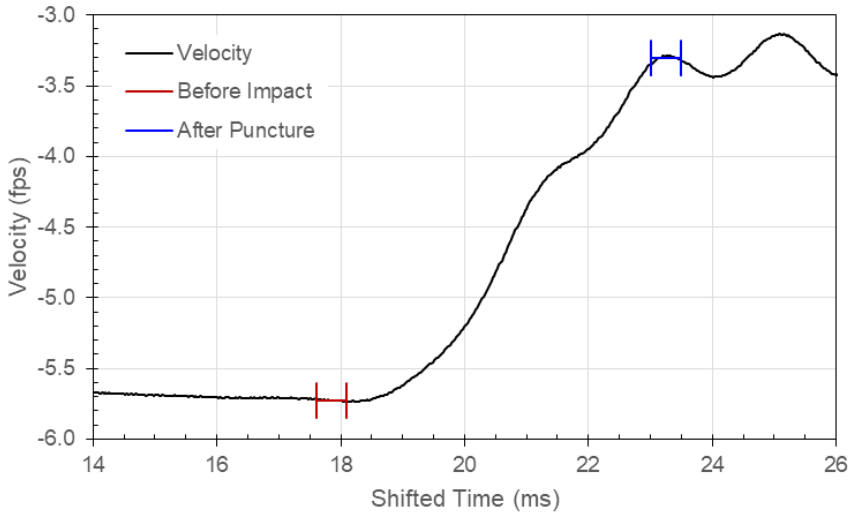

Figure 181: Carriage Velocity in Test 78 with Specimen T188-06 and 0.500-Inch Probe

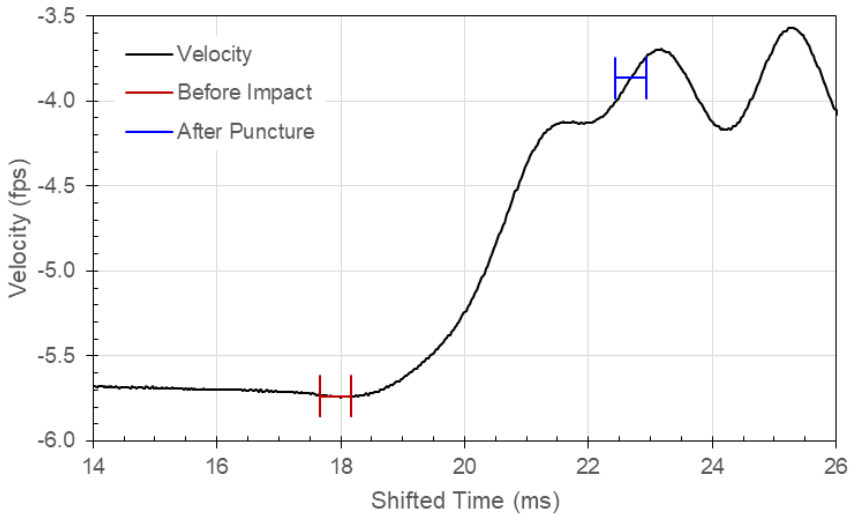

Figure 182: Carriage Velocity in Test 79 with Specimen T188-07 and 0.500-Inch Probe

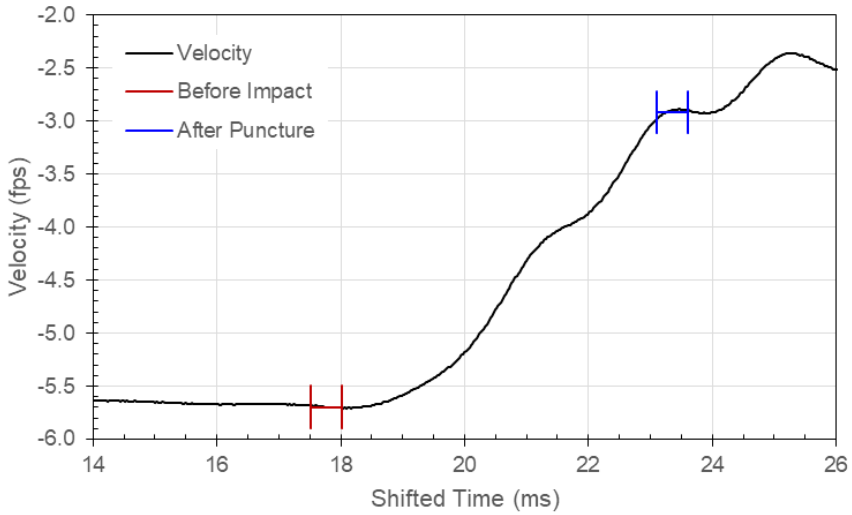

Figure 183: Carriage Velocity in Test 80 with Specimen T188-08 and 0.500-Inch Probe

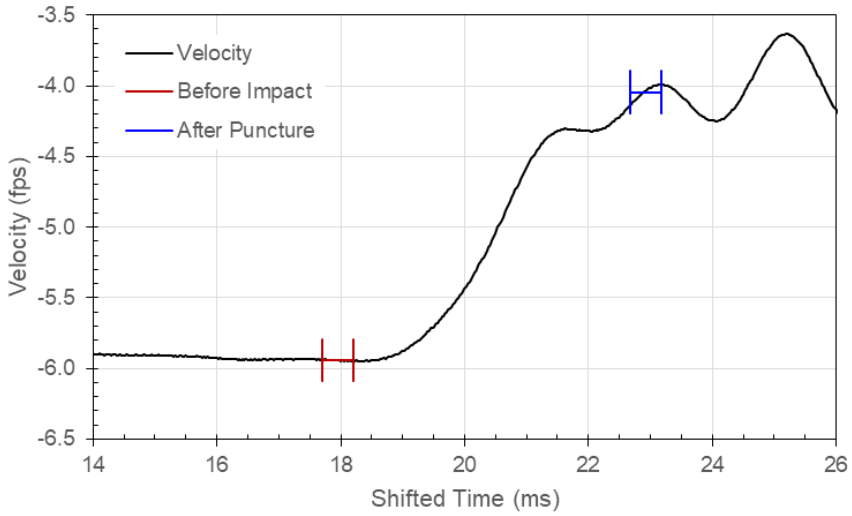

Figure 184: Carriage Velocity in Test 81 with Specimen T188-09 and 0.500-Inch Probe

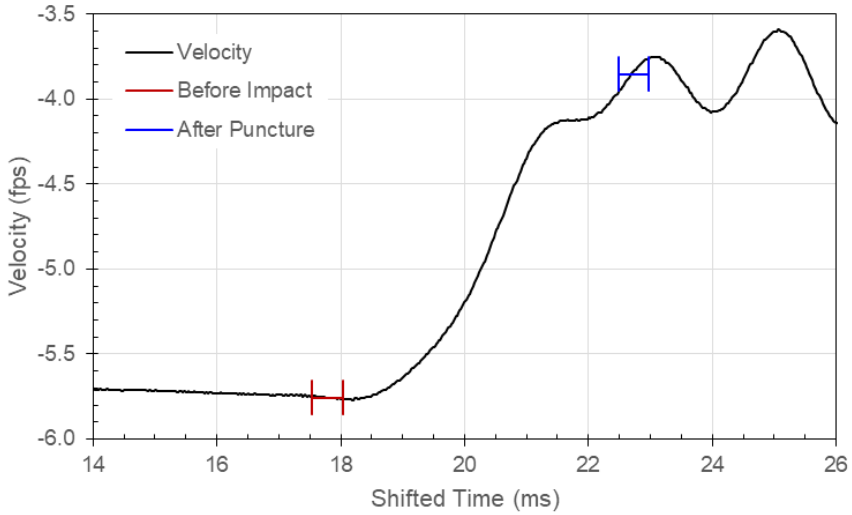

Figure 185: Carriage Velocity in Test 82 with Specimen T188-10 and 0.500-Inch Probe

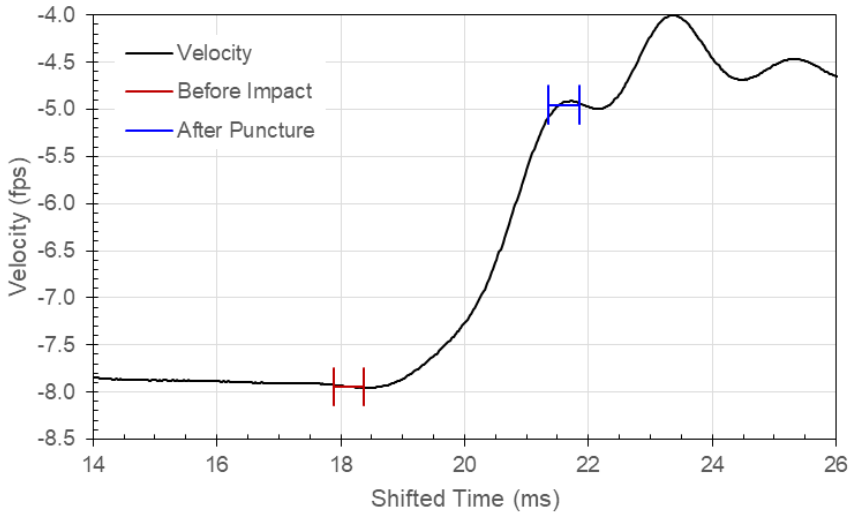

Figure 186: Carriage Velocity in Test 83 with Specimen T188-11 and 1.000-Inch Probe

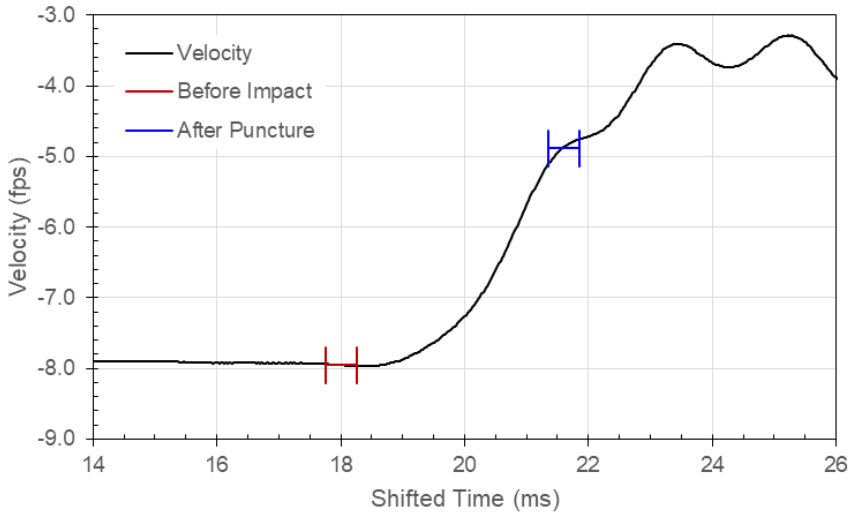

Figure 187: Carriage Velocity in Test 84 with Specimen T188-12 and 1.000-Inch Probe

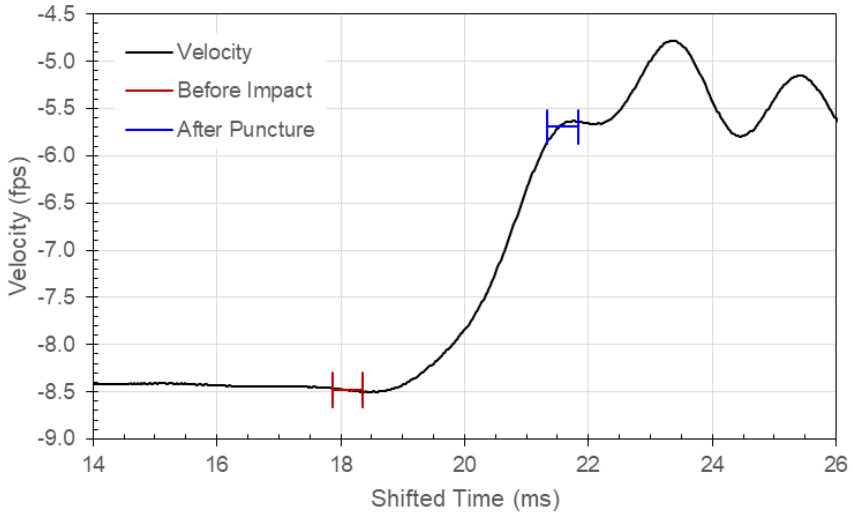

Figure 188: Carriage Velocity in Test 85 with Specimen T188-13 and 1.000-Inch Probe

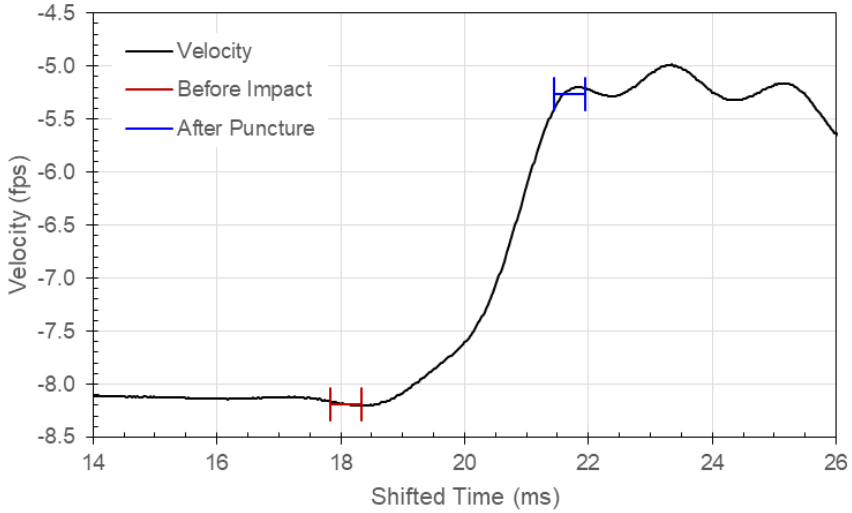

Figure 189: Carriage Velocity in Test 86 with Specimen T188-14 and 1.000-Inch Probe

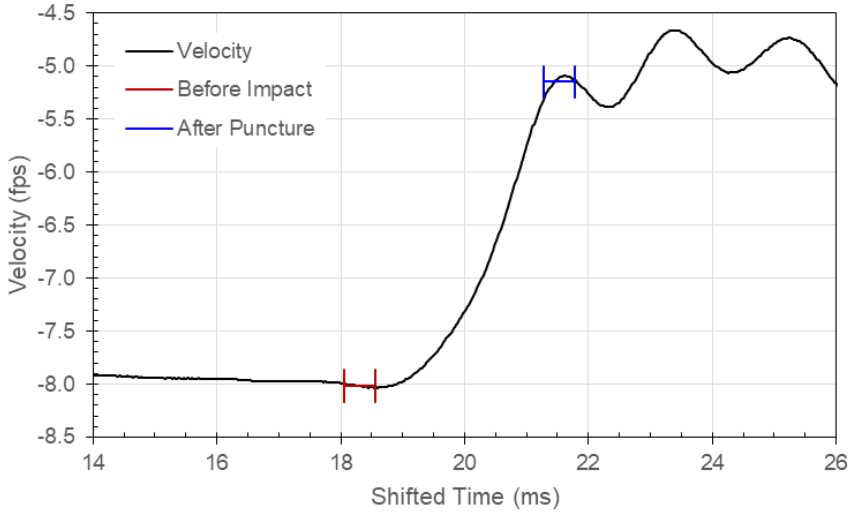

Figure 190: Carriage Velocity in Test 87 with Specimen T188-15 and 1.000-Inch Probe

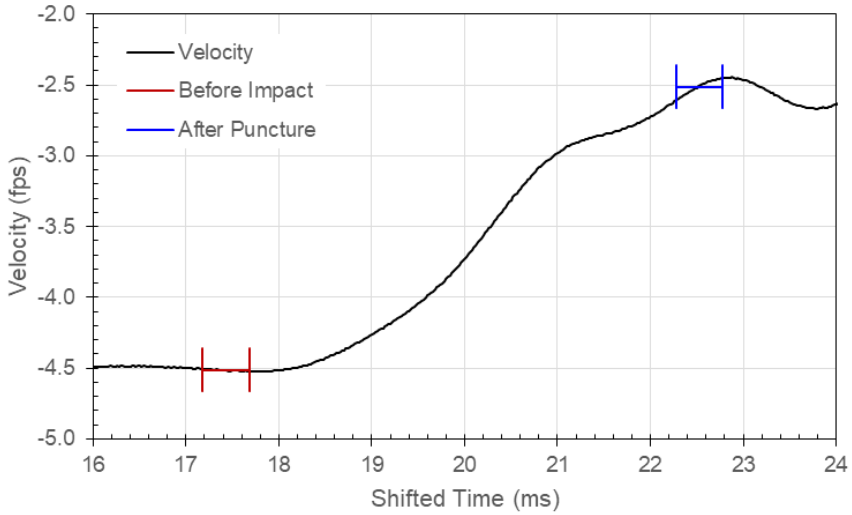

Figure 191: Carriage Velocity in Test 88 with Specimen T250-01 and 0.250-Inch Probe

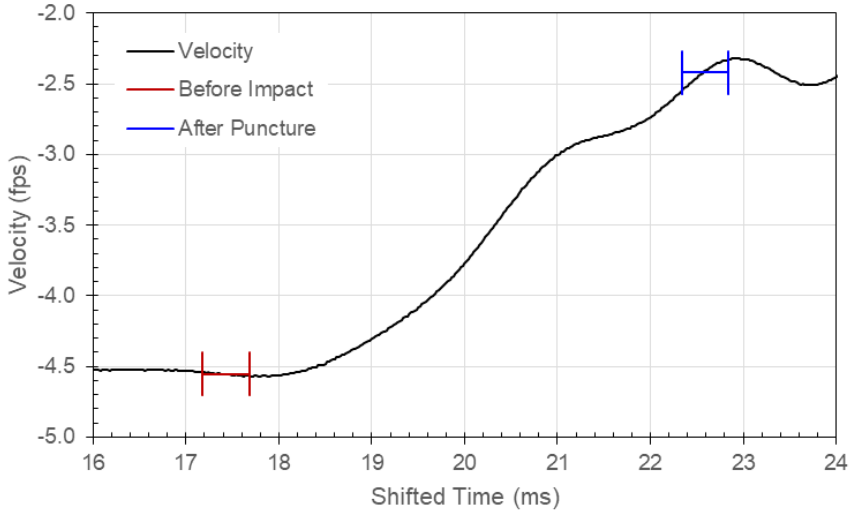

Figure 192: Carriage Velocity in Test 89 with Specimen T250-02 and 0.250-Inch Probe

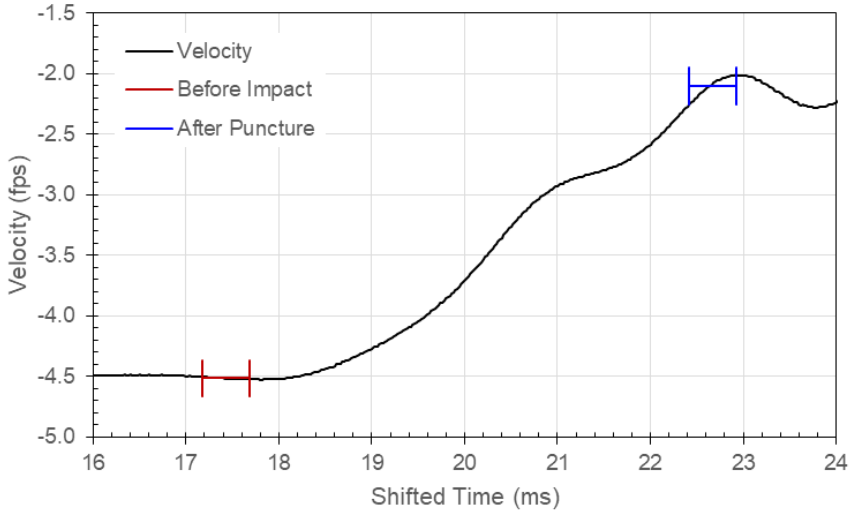

Figure 193: Carriage Velocity in Test 90 with Specimen T250-03 and 0.250-Inch Probe

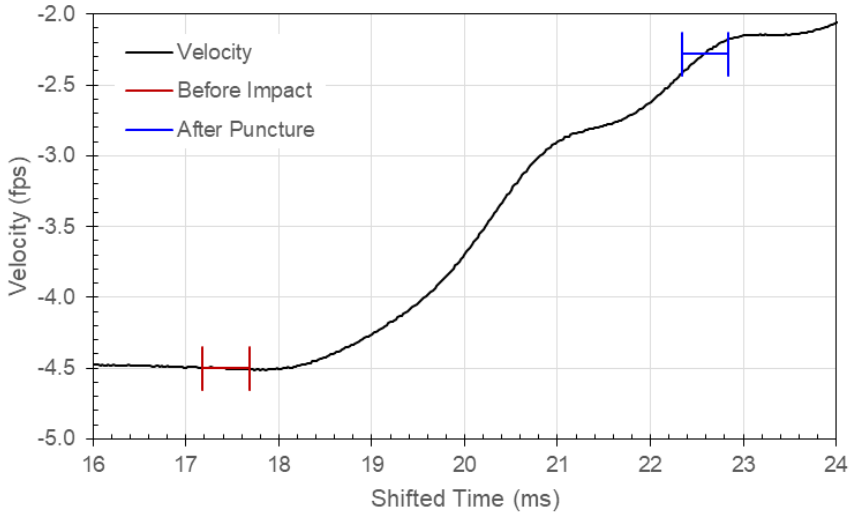

Figure 194: Carriage Velocity in Test 91 with Specimen T250-04 and 0.250-Inch Probe

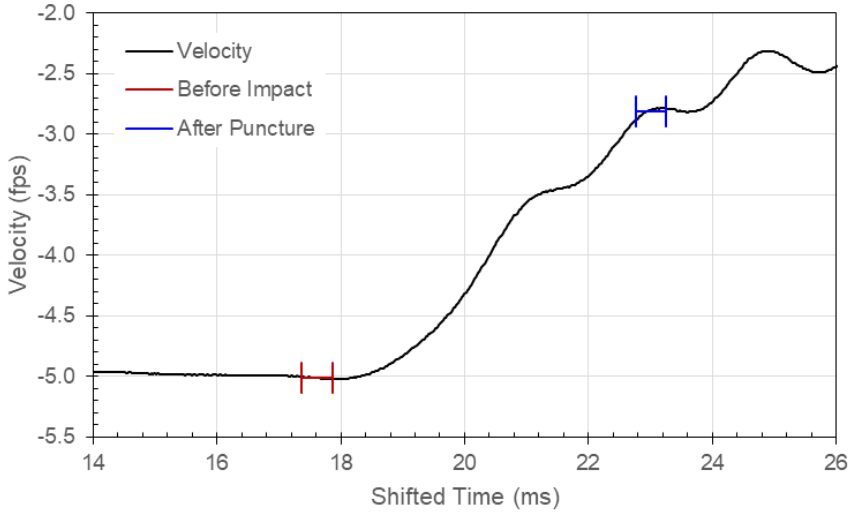

Figure 195: Carriage Velocity in Test 92 with Specimen T250-05 and 0.250-Inch Probe

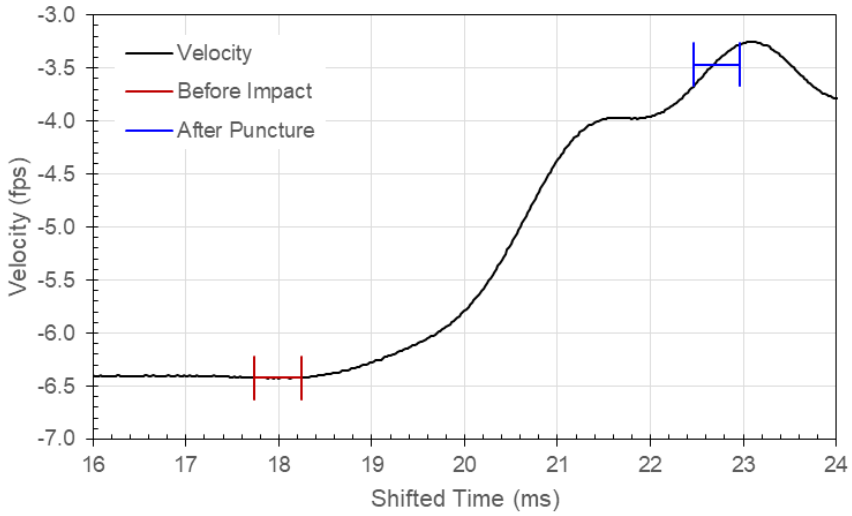

Figure 196: Carriage Velocity in Test 94 with Specimen T250-07 and 0.500-Inch Probe

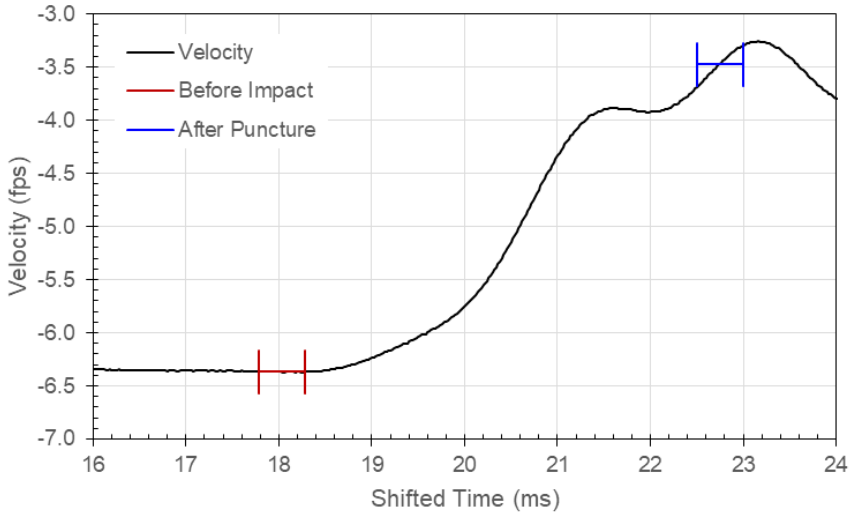

Figure 197: Carriage Velocity in Test 95 with Specimen T250-08 and 0.500-Inch Probe

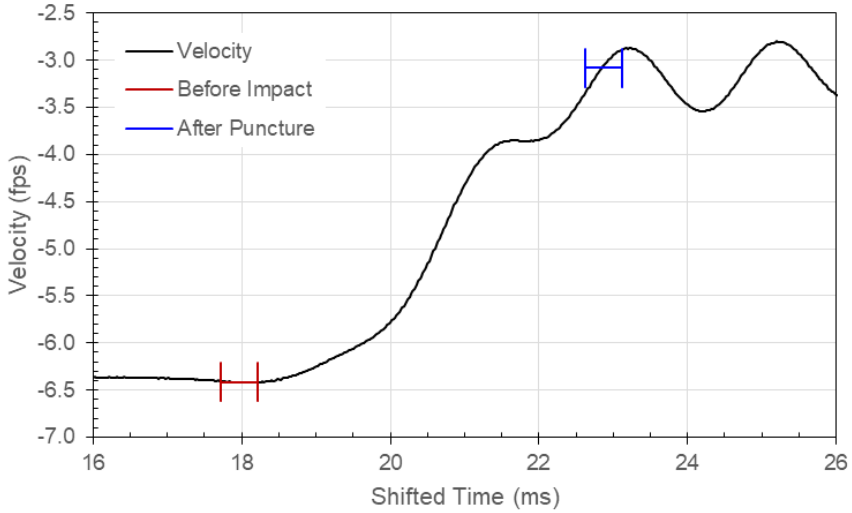

Figure 198: Carriage Velocity in Test 96 with Specimen T250-09 and 0.500-Inch Probe

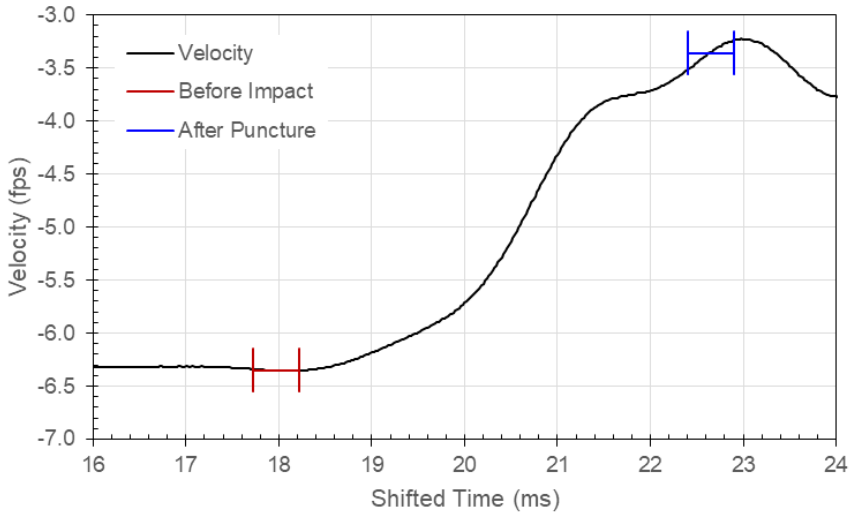

Figure 199: Carriage Velocity in Test 97 with Specimen T250-10 and 0.500-Inch Probe

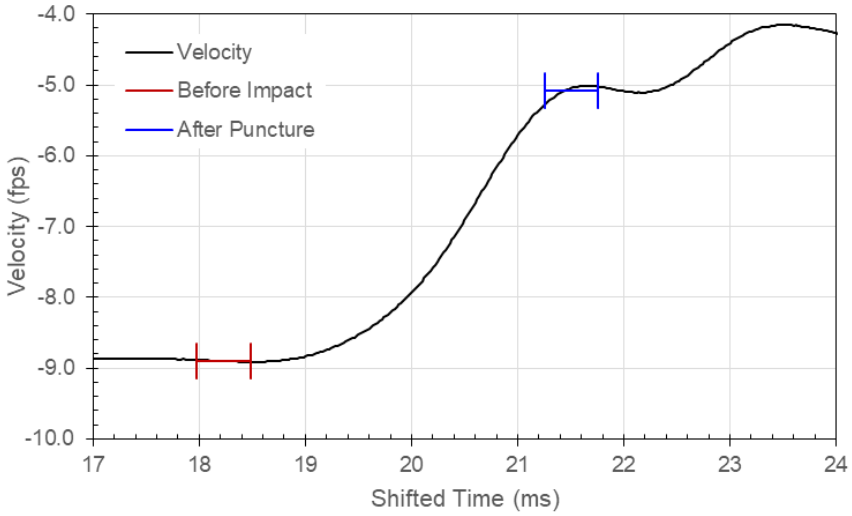

Figure 200: Carriage Velocity in Test 98 with Specimen T250-11 and 1.000-Inch Probe

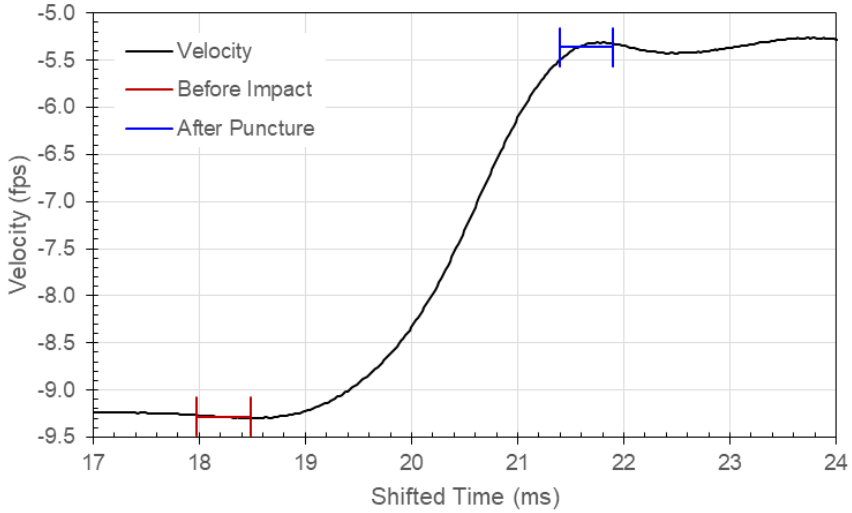

Figure 201: Carriage Velocity in Test 99 with Specimen T250-12 and 1.000-Inch Probe

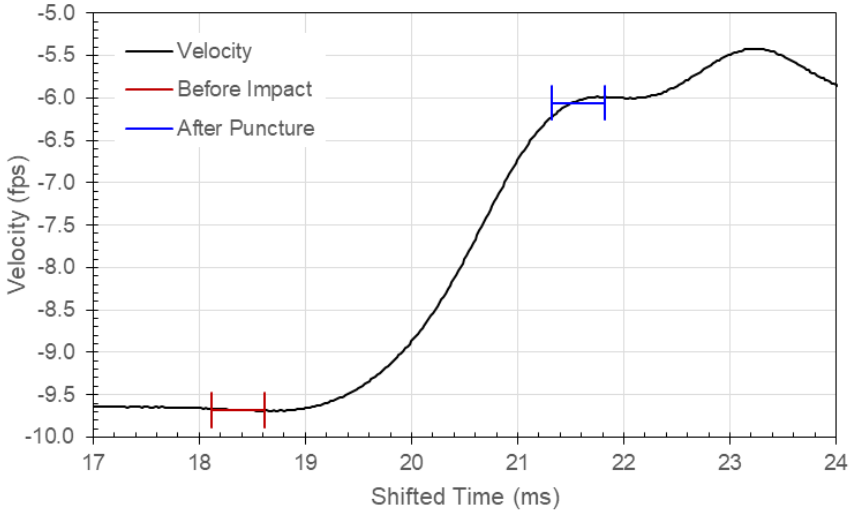

Figure 202: Carriage Velocity in Test 100 with Specimen T250-13 and 1.000-Inch Probe

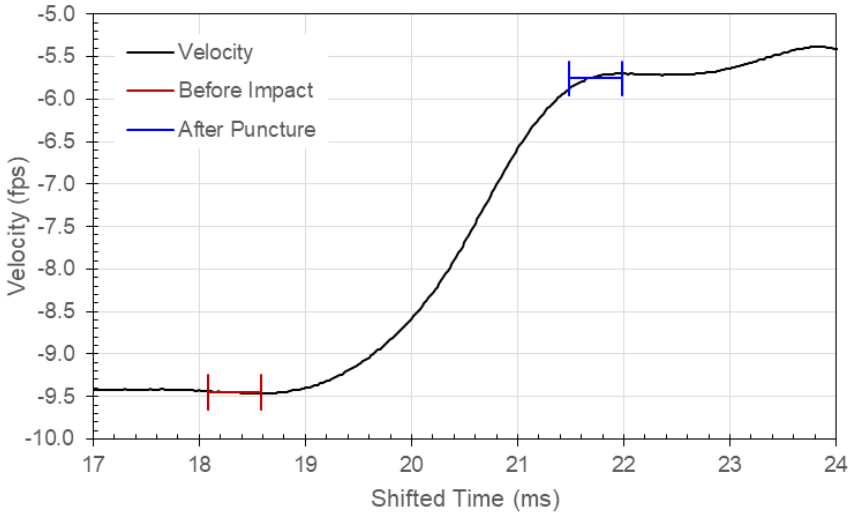

Figure 203: Carriage Velocity in Test 101 with Specimen T250-14 and 1.000-Inch Probe

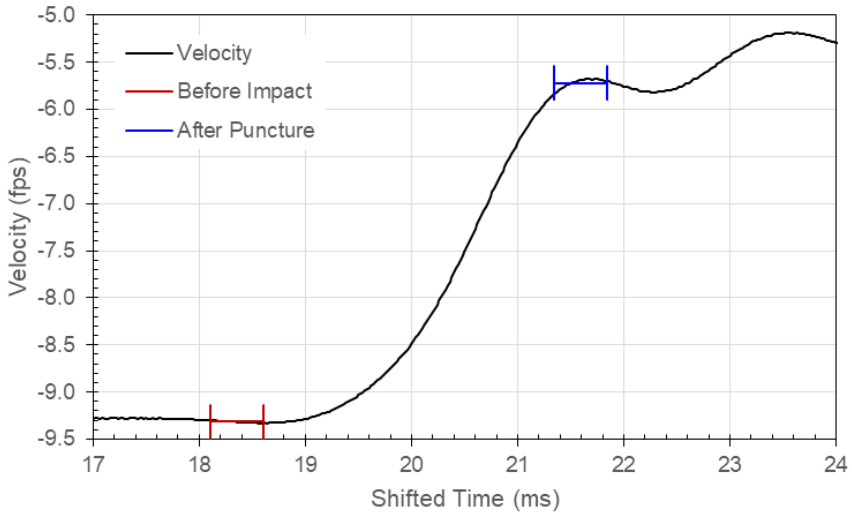

Figure 204: Carriage Velocity in Test 102 with Specimen T250-15 and 1.000-Inch Probe

Sandia National Laboratories is a multimission laboratory managed and operated by National Technology and Engineering Solutions of Sandia, LLC, a wholly owned subsidiary of Honeywell International, Inc., for the U.S. Department of Energy's National Nuclear Security Administration under contract DE-NA0003525.